High Statistics Search for $\nu_\mu(\overline{\nu}_\mu) \to \nu_e(\overline{\nu}_e)$ Oscillations in the Small Mixing Angle Regime

Alexandru Romosan

R-1536
CU-402
Nevis-296

Columbia University
Department of Physics
New York, New York 10027

HIGH STATISTICS SEARCH FOR $\nu_\mu(\overline{\nu}_\mu) \to \nu_e(\overline{\nu}_e)$ OSCILLATIONS IN THE SMALL MIXING ANGLE REGIME

Alexandru Romosan

Submitted in partial fulfillment of the
requirements for the degree
of Doctor of Philosophy
in the Graduate School of Arts and Sciences,
Columbia University

National Science Foundation
NSF PHY 92-15987
NSF PHY 95-12810

1996

HIGH STATISTICS SEARCH FOR $\nu_\mu(\overline{\nu}_\mu) \to \nu_e(\overline{\nu}_e)$ OSCILLATIONS IN THE SMALL MIXING ANGLE REGIME*†

Alexandru Romosan
Columbia University, New York, NY 10027

*Research supported by the National Science Foundation.
†Submitted in partial fulfillment of the requirements for the degree of Doctor of Philosophy in the Graduate School of Arts and Sciences, Columbia University.

Abstract

Limits on $\nu_\mu(\overline{\nu}_\mu) \to \nu_e(\overline{\nu}_e)$ oscillations based on a statistical separation of $\nu_e N$ charged current interactions in the CCFR detector at Fermilab are presented. ν_e interactions are identified by the difference in the longitudinal shower energy deposition pattern of $\nu_e N \to eX$ versus $\nu_\mu N \to \nu_\mu X$ interactions. Neutrino energies range from 30 to 600 GeV with a mean of 140 GeV, and ν_μ flight lengths vary from 0.9 km to 1.4 km. The lowest 90% confidence upper limit in $\sin^2 2\alpha$ of 1.1×10^{-3} is obtained at $\Delta m^2 \sim 300$ eV^2. For $\sin^2 2\alpha = 1$, $\Delta m^2 > 1.6$ eV^2 is excluded, and for $\Delta m^2 \gg 1000$ eV^2, $\sin^2 2\alpha > 1.8 \times 10^{-3}$ is excluded. This result is the most stringent limit to date for $\Delta m^2 > 25$ eV^2 and it excludes the high Δm^2 oscillation region favoured by the LSND experiment. The ν_μ-to-ν_e cross-section ratio was measured as a test of $\nu_\mu(\overline{\nu}_\mu) \leftrightarrow \nu_e(\overline{\nu}_e)$ universality to be $1.026 \pm 0.025(\text{stat}) \pm 0.049(\text{syst})$.

Acknowledgements

"[they] threw their watches off the roof to cast their ballot for Eternity outside of Time, & alarm clocks fell on their heads every day for the next decade"

Allen Ginsberg

It is my pleasure to acknowledge the people who made the completion of this dissertation possible, not only because they deserve it, but also because doing so brings back many pleasant memories.

Foremost I thank Michael Shaevitz, my adviser, for his guidance and support along the way. Without him, graduate school would have not been "the best years of my life" (his quote). I went to Columbia because I wanted to live in New York City, but I spent three and a half years away from the city, at Fermilab, because I really enjoyed working with him. The other professor at Columbia who really inspired me (read force) to continue working on this neutrino experiment even if it meant going to Fermilab was Tim Bolton. I owe a lot of my understanding of particle physics to his incredibly clear explanations. It was also Tim who provided the initial impetus for this thesis by attempting (unsuccessfully) to extract the number of electron neutrinos. I simply continued where he left of and the rest is, as they say, history. I will never forgive him though for abandoning us to go to (of all places) Kansas.

Life in the middle of a corn field can be pretty miserable, but the people I worked with there (and the frequent trips to New York) made it a lot more bearable. The two Columbia postdocs I had the pleasure to work with were Janet Conrad, and Eric Stern.

Janet (now professor Janet) helped not only with the physics questions I had, but also with more mundane things like buying a car. The Thursday night talks she organized for so long at her house were enjoyable from a physics point of view and brought everybody working on the experiment closer together. Eric is an absolute wizard when it comes to electronics and computers. I have a lot more to learn before I can even come close to his caliber. Without his understanding of how the TDC's work, and his help I would have never finished that job.

Panagiotis Spentzouris was the third Columbia postdoc who joined the experiment during my stay at Fermilab. His friendship was one of the best things that happened to me while at Fermilab and I can only hope that our paths will cross again in the future. Enjoying "the good things of life" (TM) without him is just not the same.

I am happy to have worked with Dr. Robert Bernstein. His unique perspective on life, as well as his broad interests outside physics (like playing Doom) made for many interesting discussions. I also want to thank him for reading drafts of this thesis and providing helpful comments on how to improve it.

I have learned a great deal from most of the people I worked with on the experiment. In particular, I want to thank Prof. Arie Bodek whose suggestions helped with crucial parts of this analysis. It was his idea to *add* a muon track to the neutral current events instead of subtracting one from the charged current events, which I consider to be the turning point of the analysis.

Nevis Laboratories was a wonderful place to work. From the lunchtime volleyball games to varied discussions on physics and other topics I enjoyed every minute of being there. The staff of Nevis Labs: Donald Bunch, Dave Leon, Fred de Martino, Dorothy Palmer, Bob Peters, Gail Smith and Ann Therrien keep the place going. I don't know what I would have done without their help.

I learned most of what I know about electronics from Herb Cunitz. He succeeded

where many University of Toronto professors had failed before him. His patience and understanding of electronics have finally made me enjoy playing with that stuff. Joe Capone and Nancy Bishop in the Nevis electronics shop fixed many of my botched attempts to replace a chip. It was the ease with which they did it in the first place that made me believe I could do it by myself. Sadly, that wasn't quite true.

My dearest friend Jennifer helped make my life in New York City a much more pleasant experience than it would have been without her. I can only hope I returned the favour by making her understand physics just a little bit better.

I was fortunate enough to have shared the last two and a half years of my life with Donna Naples. She has put up with a lot, and I can only be grateful for that. Her beauty, humour, and love were the principal source of my happiness. She is a much better physicist than I can ever hope to be, and has read this thesis many times trying to help me make it better. I love her dearly and I will miss her.

My debt and gratitude to my parents of course extends beyond the years I spent in graduate school. Throughout my life, they have been a source of inspiration and support for me. Unfortunately, my mother never got the chance to see me finish this thesis. Of all people, I think she would have been the happiest to see me finally graduate. I dedicate this thesis to her memory.

Contents

List of Tables

List of Figures

Chapter 1

Introduction

The existence of neutrino mass and mixing would have important implications for fundamental problems in both particle physics and cosmology. These include violation of lepton family number conservation, the mass of the universe, and the observed neutrino deficits from the sun and from atmospheric sources. Neutrino oscillations are a necessary consequence of non-zero neutrino mass and mixing since neutrinos are produced and detected in the form of weak-interaction eigenstates whereas their motion, as they propagate from the point of production to their detection, is dictated by the mass eigenstates [1]. To date, there is no conclusive evidence for neutrino oscillations from laboratory-based experiments, although there are hints from the low energy LSND experiment at Los Alamos. On the other hand, there are indications of possible neutrino masses from non-laboratory experiments: in particular, the solar neutrino deficit and the possibility of a hot component of dark matter. The atmospheric neutrino anomaly, which is plagued by many uncertainties, is also in favour of neutrino oscillations and predicts that neutrinos have mass. In this thesis we present new limits on $\nu_\mu \to \nu_e$ oscillations based on the isolation of $\nu_e N$ charged current interactions in the CCFR detector with data taken during the 1987-88 fixed target run at Fermilab.

1.1 Brief Neutrino History

The existence of the neutrino (ν) was first proposed by Pauli [2] in the 1930's to explain an apparent non conservation of energy observed in nuclear β decays. Soon after Pauli's neutrino postulate, Fermi [3] proposed his theory for the β-decay in which he assumed that neutrinos have a mass much smaller than the electron, obey the Dirac equation, and have a distinct antiparticle. Using Fermi's theory, Bethe and Peirles [4] showed later the same year that an inverse β-decay process, $\nu n \rightarrow e^- p$, should also be possible with a cross-section on the order of 10^{-44} cm^2 which, they thought, made the neutrino impossible to detect.

Direct experimental observation of the neutrino was achieved in 1956 when Cowan, Reines and coworkers [5] detected antineutrinos from a nuclear reactor through the reaction $\overline{\nu}_e p \rightarrow n e^+$. Soon after, Davis and coworkers showed that the neutrino and the antineutrino are not identical particles by searching unsuccessfully for the reaction $\overline{\nu} + {}^{37}\mathrm{Cl} \rightarrow {}^{37}\mathrm{Ar} + e^-$ [6]. The existence of a second lepton generation was proven experimentally in 1962 by Lederman, Schwartz, and Steinberger [7], when neutrinos produced in the decay of charged pions interacted to produce only muons and no electrons. In 1975 at SLAC Perl *et al.* discover a third generation of charged leptons, τ^+ and τ^- [8]. Direct observation of $\nu_\tau(\overline{\nu}_\tau)$ hasn't been achieved yet, but experiment E531 at Fermilab [9] has demonstrated that ν_τ is different from ν_e and ν_μ. The precise measurement of the width of the Z at LEP and SLC has shown that there are only three species of light neutrinos [10].

In the standard model, neutrinos are generally assumed to be massless, although with minimal extensions it is possible to give neutrinos mass. Direct mass measurements in the laboratory have confirmed that neutrinos have a very small mass. The best ν_τ mass measurements were done by the ALEPH collaboration [13] which used the decay of a τ particle into five charged pions plus a π^0 and, based on 24 events, set an upper limit of 24 MeV. The measurements by the PSI group [12] of the pion decay into a muon and

neutrino give an upper limit for the ν_μ mass of 170 KeV. The best method to measure the ν_e mass is to study the end-point of the electron energy spectrum of tritium decay, which is about 18570 eV. If the ν_e's have a mass, m_ν then the end-point would be at a lower value by m_ν. What is interesting about the ν_e mass measurements is that all the best experiments obtain negative values for the square the measured electron neutrino mass. The current values of the best upper limits for the mass of each neutrino species are summarized in Table 1.1.

Flavour	Mass Limit	Confidence Level	Experiment
ν_e	4.35 eV	95%	Troitsk [11]
ν_μ	170 KeV	90%	PSI [12]
ν_τ	24 MeV	95%	ALEPH [13]

Table 1.1: Current neutrino mass limits.

To probe neutrino masses significantly lower than these direct measurements one needs to use other techniques such as neutrino oscillations. Neutrino oscillation experiments are a particularly sensitive way to test for non-zero neutrino mass and mixing over a broad range of values. The existence of neutrino oscillations would imply that neutrinos have mass and that there is mixing among the different flavours of neutrinos. No evidence for such oscillations has been observed so far at accelerator based experiments, with the exception of LSND. There is also some indications of possible neutrino oscillations coming from experiments observing non-terrestrial neutrinos. The various types of neutrino experiments, as well as the current limits on neutrino oscillations are presented in the following sections of this chapter.

1.2 Neutrino Oscillation Experiments

Neutrino oscillation experiments can be separated into two categories depending on the type of search performed. In exclusive (or appearance) searches, an experiment looks for the

anomalous appearance of ν_β type neutrinos in a beam of predominantly ν_α type neutrinos. Finding such neutrinos would constitute evidence in favour of $\nu_\alpha \leftrightarrow \nu_\beta$ oscillations. On the other hand, an inclusive (or disappearance) measurement is made by examining the change in flux of a given neutrino type, ν_α with distance. If the measured flux of neutrinos should turn out to be less than the flux expected in the absence of oscillations, it would constitute evidence in favour of the $\nu_\alpha \leftrightarrow \nu_x$ oscillations.

Since neutrino oscillations have not been observed, in most of the literature the experimental data is analyzed under the simplest assumption, that of oscillation between two states. We show in the following chapter that in such case the oscillation probability depends on two independent parameters: a mixing angle θ and a mass square difference Δm^2, as

$$P(\nu_\alpha \rightarrow \nu_\beta) = \sin^2 2\theta \sin^2 \left(\frac{1.27 \Delta m^2 L}{E_\nu} \right) \tag{1.1}$$

where $\Delta m^2 = |m_1^2 - m_2^2|$, with m_1 and m_2 being the neutrino masses, is in units of eV^2, L is the distance between the point of creation and detection in km, and $E_\nu \simeq p$ is the neutrino energy in GeV.

It is evident from Eq. 1.1 that neutrino oscillations would not be observed in a given experiment if the difference of the square of the neutrino masses, Δm^2 were so small that for all L and E characteristic of the experiment the argument of the second sine function were much smaller than unity. Neutrino oscillations may be observed in general if the values of L and E typical of a given experiment satisfy the inequality:

$$\Delta m^2 \geq \frac{E}{L} \tag{1.2}$$

This inequality implies the parameter

$$(\Delta m^2)_0 = \frac{E}{L} \tag{1.3}$$

which quantitatively characterizes the sensitivity of an experiment searching for neutrino oscillations.

To date, four major methods to search for neutrino oscillations have been employed:

- **Accelerators:** A neutrino beam is generated by decaying pions and kaons produced when a hadron beam strikes a production target. The neutrino flux for such experiments is in general very well understood. Typical experiments involve searching for either appearance (exclusive channel) or disappearance (inclusive channel) of a particular flavour neutrino from the beam.

- **Reactors:** $\overline{\nu}_e$ are created by the β^- decays of fission products in the core of a nuclear reactor. These type of experiments search for a $\overline{\nu}_e$ deficit some distance away from the source.

- **Atmospheric neutrinos:** Cosmic rays, mostly protons or α particles, interact in the atmosphere producing pions and kaons, some of which decay before reaching the earth. These experiments measure the $(\nu_\mu + \overline{\nu}_\mu)/(\nu_e + \overline{\nu}_e)$ flux ratio and compare it to the expected ratio of two.

- **Solar neutrinos:** ν_e are produced by nuclear reactions inside the sun. The measured flux is compared against solar model calculations.

Typical values of the parameter $(\Delta m^2)_0$ are given in Table 1.2. As it can be seen from the table, the most sensitive (with respect to Δm^2) experiments with neutrinos from terrestrial sources are the reactor experiments.

1.2.1 Exclusive (or appearance) experiments $\nu_\alpha \to \nu_\beta$

This type of search is limited by the number of background ν_β from standard sources and the total number of ν_α interactions, N_α detected during the measurement. If the background fraction is very small and the measurement yields no detected ν_β interactions, then the sensitivity of the measurement depends only on N_α, E_ν, and the distance L from the source to the detector. To see this consider the oscillation probability given in Eq. 1.1. $P(\nu_\alpha \to \nu_\beta)$

Neutrino source	E (MeV)	L (m)	$(\Delta m^2)_0$ (eV^2)
Reactor	1	10^2	10^{-2}
Meson factory	10	10^2	10^{-1}
High-energy accelerator	10^4	10^3	10
Atmospheric neutrinos	10^3	10^7	10^{-4}
Sun	1	10^{11}	10^{-11}

Table 1.2: Values of the parameter $(\Delta m^2)_0$ qualitatively characterizing the sensitivity of a given experiment searching for neutrino oscillations. E and L are the neutrino energy and the source-detector distance typical of the experiment.

can also be defined as:

$$P(\nu_\alpha \to \nu_\beta) = \frac{N_\beta^{obs} - N_\beta^{back}}{N_\alpha} \tag{1.4}$$

where N_β^{obs}, N_β^{back} are the number of ν_β observed and background respectively. If we assume a Poisson distribution for the number of ν_β observed, then if $N_\beta^{obs} = 2.3$ there is a 10% probability that $N_\beta = 0$. Conversely, if $N_\beta^{obs} > 2.3$ one says that at 90% confidence level $N_\beta \neq 0$. With $N_\beta^{back} = 0$, Eqs. (1.1) and (1.4) at 90% confidence level become:

$$\sin^2 2\theta \sin^2 \left(\frac{1.27 \Delta m^2 L}{E_\nu} \right) > \frac{2.3}{N_\alpha} \tag{1.5}$$

The second term averages to 1/2 for large values of Δm^2. For small values of Δm^2 it can be replaced by the argument of the sine function. The expected sensitivity range for 90% confidence level with no background subtraction is then given by:

$$\text{Small } \Delta m^2 \text{ region} \qquad \Delta m^2 \sin 2\theta > \frac{1}{1.27} \left(\frac{E_\nu}{L} \right) \left(\frac{2.3}{N_\alpha} \right)^{1/2} \propto \text{ const.} \tag{1.6}$$

$$\text{Large } \Delta m^2 \text{ region} \qquad \sin^2 2\theta > \frac{4.6}{N_\alpha} \propto L^2 \tag{1.7}$$

On the other hand, if there exists a significant ν_β background fraction, $f = N_\beta^{back}/N_\alpha$ in the beam or from misidentification in the detector, then the expected background must be subtracted to obtain the best sensitivity. The subtraction introduces additional statistical and systematic errors to the above formula. For this case the error in the oscillation probability at 90% confidence level becomes $1.62\sqrt{N_\beta^{back}}$. This leads to the following sensitive

regions:

$$\text{Small } \Delta m^2 \text{ region} \qquad \Delta m^2 \sin 2\theta > \left(\frac{E_\nu}{L}\right)\left(\frac{f}{N_\alpha}\right)^{1/4} \propto \frac{1}{\sqrt{L}} \tag{1.8}$$

$$\text{Large } \Delta m^2 \text{ region} \qquad \sin^2 2\theta > 3.2\left(\frac{f}{N_\alpha}\right)^{1/2} \propto L \tag{1.9}$$

For all these formulae, the dependence on distance assumes that the number of detected events, N_α, decreases as $1/L^2$. For small Δm^2, sensitivity can be improved slightly by moving to larger distances at the expense of a much poorer $\sin^2 2\theta$ limit at large masses.

1.2.2 Inclusive (or disappearance) experiments ($\nu_\alpha \to \nu_x$)

For an inclusive search, the neutrino flux seen by two detectors located at different distances from the source is compared. This comparison can be made as a function of energy and is interpreted in terms of the expected oscillation behaviour. The comparison is bounded by the statistical and systematic errors of a given measurement and the data is used to restrict the probability that $\nu_\alpha \to \nu_x$ is less than some limit δ at 90% confidence level. This limit on the disappearance probability at a given energy E_ν can then be used to exclude a certain region in the $\Delta m^2 - \sin^2 2\theta$ plane bounded by:

$$\text{Lower } \Delta m^2 \text{ limit} \qquad \Delta m^2 \sin 2\theta > \frac{\sqrt{\delta}}{1.27}\frac{E}{L} \tag{1.10}$$

$$\text{Upper } \Delta m^2 \text{ limit} \qquad \Delta m^2 < 3 \text{ to } 5\ \frac{E}{L} \tag{1.11}$$

$$\text{Minimum } \sin^2 2\theta \text{ limit} \qquad \sin^2 2\theta > \delta \tag{1.12}$$

where the large Δm^2 bound results from finite experimental resolution on energy and position that smears the oscillation phase difference in the two detectors. This type of experiments is particularly sensitive to oscillations to any type of neutrino including non-standard sterile (non interacting) neutrinos.

1.3 Current Status of Neutrino Oscillations

A large number of experiments have been performed to search for neutrino oscillations using both terrestrial and extra-terrestrial sources of neutrinos. Experiments using laboratory neutrinos have the advantage of using a beam that is well understood in contrast to experiments using extra-terrestrial neutrinos which rely on complex models to predict the neutrino flux expected at the detectors. To date there is no conclusive evidence for neutrino oscillations despite hints from the so-called atmospheric and solar neutrino deficits. Below is a list with a brief description of the various experiments which set our current knowledge of neutrino oscillations.

1.3.1 Accelerator Experiments

- **BNL-E734** The Brookhaven E734 experiment ran during three different periods in 1981, 1983, and 1986. The main purpose of the experiment was to study neutral and charged current elastic neutrino interactions using a total absorption calorimeter-target with a total mass of 170 tons. At the 90% confidence level, $\sin^2 2\theta < 3.4 \times 10^{-3}$ was excluded for large Δm^2 values. At full mixing, *i.e.* $\sin^2 2\theta = 1$, $\Delta m^2 > .4$ eV^2 was excluded [14].

- **BNL-E776** The Brookhaven E776 experiment, performed in 1985, searched for ν_e appearance in a narrow band ν_μ beam with a mean energy $\langle E_\nu \rangle = 1.4$ GeV. A second run was taken in 1986 for a search for $\nu_e(\overline{\nu}_e)$ above expected background in a $\nu_\mu(\overline{\nu}_\mu)$ wide band beam. The detector was a 230 metric ton finely segmented electromagnetic calorimeter target. At the 90% confidence level, $\sin^2 2\theta < 3.0 \times 10^{-3}$ was excluded for large Δm^2 values. At full mixing, *i.e.* $\sin^2 2\theta = 1$, $\Delta m^2 > .075$ eV^2 was excluded [15].

- **KARMEN** The KARMEN (KArlsruhe Rutherford interMediate Energy Neutrino) collaboration searches for the appearance of $\overline{\nu}_e$ detected via the charged current re-

action on the protons (hydrogen) of the scintillator in the detector. The signature of such an interaction is the emission of a positron and up to three γ rays within 100 μs after the positron corresponding to the binding energy of the neutron. The data sample consists of 147 events. At the 90% confidence level $\sin^2 2\theta < 5.9 \times 10^{-3}$ was excluded for large Δm^2 values. At full mixing, *i.e.* $\sin^2 2\theta = 1$, $\Delta m^2 > .1$ eV^2 was excluded [16]. KARMEN hopes to improve their Δm^2 sensitivity by reducing backgrounds.

- **LSND** The LSND collaboration, using a liquid scintillator neutrino target has reported a signal consistent with $\overline{\nu}_\mu \rightarrow \overline{\nu}_e$ oscillations at $\sin^2 2\theta \approx 10^{-2}$ at large Δm^2 with values down to 1 eV^2 [17]. Most of the allowed region has been ruled out by the above mentioned experiments and so a possible signal is only consistent if $\sin^2 2\theta \lesssim 3 \times 10^{-3}$ or Δm^2 is below 1 eV^2. There are proposals to upgrade existing detectors which will allow for a final decision in the next 2-3 years, whether neutrino oscillations exist in the parameter area proposed by the LSND experiment.

- **CCFR** The CCFR collaboration has previously reported a limit on $\nu_\mu \rightarrow \nu_e$ oscillations using the ratio of neutral to charged current neutrino events in the massive and relatively coarse grained CCFR detector comparable in sensitivity to the above mentioned limits [18]. The lowest 90% confidence upper limit in $\sin^2 2\theta$ of 1.9×10^{-3} is obtained at $\Delta m^2 \approx 350$ eV^2. This result is the most stringent limit to date for $250 < \Delta m^2 < 450$ eV^2, and also excludes at 90% confidence much of the high Δm^2 region favoured by the recent LSND observations.

These limits, together with the 90% and 99% confidence allowed regions from LSND are shown in Figure 1.1.

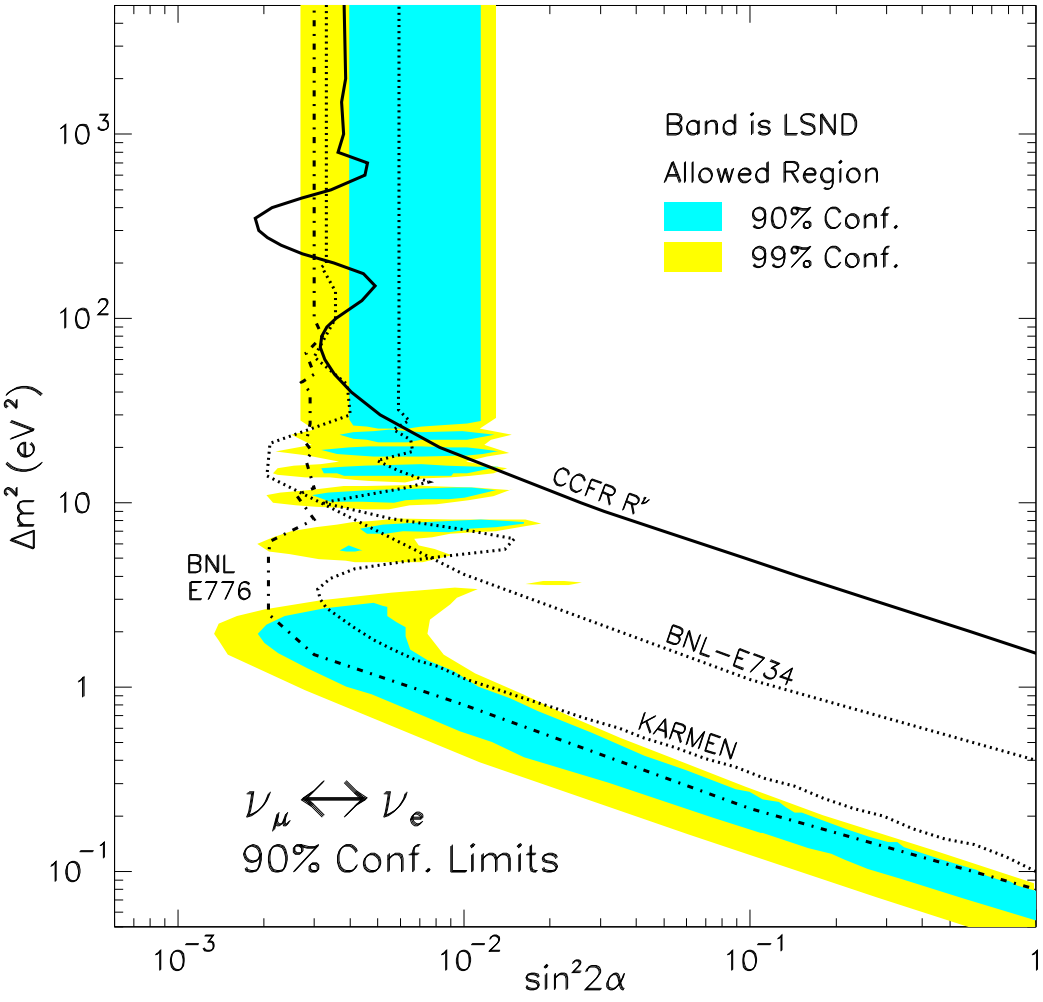

Figure 1.1: Current status of the excluded region of $\sin^2 2\alpha$ and Δm^2 for $\nu_\mu \to \nu_e$ oscillations from accelerator experiments. The shaded bands are the LSND 90% (darker) and 99% (lighter) confidence allowed regions.

1.3.2 Atmospheric Neutrino Experiments

- **Kamiokande** The Kamiokande collaboration employs a 4.5 kton water Čerenkov detector located at about 2700 m water equivalent underground. The detector consists of two layers, each instrumented with two dimensional arrays of photomultiplier tubes (PMT). The inner volume detects Čerenkov photons radiated by relativistic charged particles. The outer layer is a 4π solid angle anti-counter used to reduce background. The ratio of muons to electron neutrinos observed in the data to that predicted by the Monte Carlo is $(\nu_\mu^{\rm DATA}/\nu_e^{\rm DATA})/(\nu_\mu^{\rm MC}/\nu_e^{\rm MC} = 0.57^{+0.08}_{-0.07} \pm 0.07$ [19], which is smaller than expected. This result can be construed as evidence for neutrino oscillations.

- **IMB-3** A water Čerenkov detector with a 3.3 kton fiducial mass instrumented with 2048 8 inch PMT's. The ratio of muon to electron neutrinos in the data to that predicted by the Monte Carlo is $0.54 \pm 0.05 \pm 0.12$ [20] which agrees with the Kamiokande result.

- **Frejus** Unlike the water-based Čerenkov experiments, the Frejus collaboration uses a 6m $\times$ 6m $\times$ 12.3m 912 ton iron calorimeter with a mean density $\rho_{avg} = 1.95$ g/cm^3. The detector is located 1780m underground to reduce background. The detector is instrumented with 912 flash chamber planes and 113 Geiger tube planes. The Frejus collaboration reports no discrepancy between data and the Monte Carlo measuring a ratio of muon to electron neutrino events of $1.00 \pm 0.15 \pm 0.08$ [21].

- **SOUDAN-2** The Soudan-2 collaboration also uses a tracking drift calorimeter consisting of 224 modules each weighing 4.3 tons. The detector was calibrated with π's and μ's between 140 and 400 MeV/c and protons at 700 and 830 MeV/c. The e/μ separation was determined to be greater than 95%. The ratio of muons in the data to the predicted by the Monte Carlo is $0.64 \pm 0.17 \pm 0.09$ consistent with the water Čerenkov results [22].

1.3.3 Solar Neutrino Experiments

- **Kamiokande**

  The Kamiokande detector is unique among other solar neutrino experiments because it is a real time experiment able to measure the direction of the incident neutrinos and can provide recoil energy information. Solar neutrinos are detected through $\nu + e \rightarrow \nu + e$ elastic scattering in the detector where the incident direction of neutrinos is well kept in that of the recoil electrons within $E\theta^2 < 2m_e$. The Kamiokande detector is mainly sensitive to the high energy solar neutrinos from the ^{8}B cycle since the minimum energy threshold of their analysis is 7.0 MeV. Data were taken during two runs, the first from January 1987 to April 1990 and the second from December 28, 1990 to February 6, 1995, and the combined solar flux was measured to be $2.80 \pm 0.19((\text{stat.}) \pm 0.33(\text{syst.}) \times 10^6$ /cm^2/sec [23]. The number of solar neutrino events observed is 597^{+41}_{-40} events whereas the expected number of events the standard solar model (SSM) of Bahcall and Pinsonneault (BP) is 1213 [24]. The flux ratio to the SSM of BP for the combined data is $0.492^{+0.034}_{-0.033}(\text{stat.}) \pm 0.058(\text{syst.})$.

- **Homestake**

  The oldest of the solar neutrino experiments, this experiment has been running since 1965 in the Homestake mine, South Dakota 5000 feet underground. The detector, a tank filled with C_2Cl_4, responds to neutrinos via the reaction

$$\nu_e + {}^{37}\text{Cl} \rightarrow {}^{37}\text{Ar} + e^- \tag{1.13}$$

  Since the threshold for this reaction is 814 KeV, the detector is sensitive to several of the neutrinos from the neutrino-generating reactions in the Sun except for p-p fusion, namely: ^{7}Be electron capture, the decay of ^{13}C, ^{15}N, and ^{8}B and $p + e^- + p$. The main advantages of this type of experiment are: (i) the availability of an inexpensive,

non hydrogen chlorine compound, C_2Cl_4 which is liquid at room temperature, (ii) the ease with which the produced argon can be removed from the liquid and measured, and (iii) the high efficiency with which ^{37}Ar can be identified. The solar neutrino rate in Solar Neutrino Units (SNU) as measured from 1970 to 1993 is [25]

$$\Sigma_{\rm expt} = 2.55 \pm 0.25\,{\rm SNU} \tag{1.14}$$

which is smaller than the prediction of the standard solar model of Bahcall and Pinsonneault [24]

$$\Sigma_{\rm theor} = 8.1 \pm 1.0\,{\rm SNU} \tag{1.15}$$

- **Gallium Experiments: SAGE, GALLEX**

The Gallium experiments are the only detectors currently in operation able to detect neutrinos produced in dominant solar processes. The neutrinos are detected through the reaction:

$$^{71}{\rm Ga} + \nu_e \rightarrow {}^{71}{\rm Ge} + e^- \tag{1.16}$$

which has a 233 KeV threshold. ^{71}Ge decays with a lifetime of 16.49 days

$$^{71}{\rm Ge} + e^- \rightarrow {}^{71}{\rm Ga} + \nu_e + {\rm X-rays} \tag{1.17}$$

and the X-rays are detected at nominal energies of 10.4 KeV (K) and 1.2 KeV (L). The GALLEX experiment operates in the Gran Sasso Underground Laboratory using 30.3 tons of gallium contained in 100 tons of concentrated $GaCl_3$ solution, and it observes $69.7 \pm 6.7 \pm^{3.9}_{4.5}$ SNU [26] over a period of 1326 days from May 1991 to October 1995, compared to a theoretical prediction based on the Bahcall model of 132 ± 7 SNU. The SAGE experiment, situated at the Baksan Neutrino Observatory in the Northern Caucasus Mountains, measures a solar flux of $72 \pm 12 \pm 7$ [27], which is consistent with the GALLEX measurement. Furthermore, the detector response of the GALLEX experiment was checked with a radioactive neutrino source. Two calibration runs were

performed using neutrinos emitted in the electron capture decay of ^{51}Cr. The ratio between the activity deduced from ^{71}Ge counting and the directly measured activity is $R = 0.92 \pm 0.08$ [26], which is a strong indication that the observed neutrino deficit is real.

The solar neutrino experimental observations relative to the prediction of Bahcall and Pinsonneault standard solar model are shown in Figure 1.2.

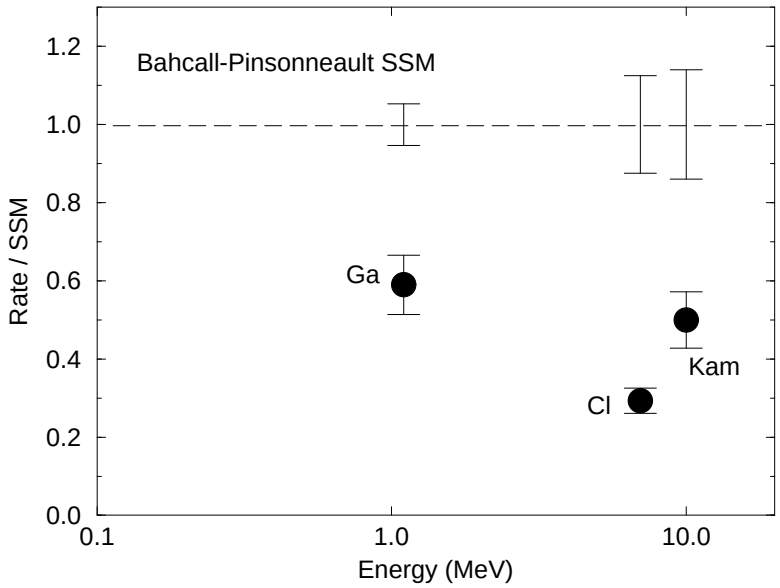

Figure 1.2: Solar neutrino experimental observations relative to the prediction of Bahcall and Pinsonneault standard solar model. Each experiment is sensitive to a range of neutrino energies. The values shown represent typical energies for each experiment.

1.3.4 Reactor Experiments

- Gösgen

  The Caltech-SIN-TUM collaboration measured the energy spectrum of antineutrinos at 37.9, 45.9, and 64.7 m from a 2800-MW nuclear power reactor in Gösgen (Switzerland). The detection of neutrinos was based on the reaction $\overline{\nu}_e \rightarrow e^+ + n$ with approximately 10^4 antineutrinos registered at each of the three measuring positions.

The detector consisted of 30 cells, containing a total of 377 l of liquid scintillator with a proton density of $(6.39 \pm 0.007) \times 10^{22}$ cm^{-3}, arranged in five planes which served both as target for the incident antineutrinos and as detector for the generated positrons. Multiwire proportional chambers filled with 95% (volume) ^{3}He and 5% (volume) CO_2 were positioned in between the scintillation planes and were used to detect the thermal neutrons produced by the neutrino interaction. The same detector was used for all three measurements. The measured spectra were analyzed in terms of a two-neutrino oscillation model, with the data being consistent with the absence of neutrino oscillations. At 90% confidence $\Delta m^2 < 0.019$ eV^2 is ruled out for maximum mixing, and for $\Delta m^2 > 5$ eV^2 $\sin^2 2\theta < 0.21$ is excluded [29].

- Bugey

This experiment searched for neutrino oscillations at 15, 40, and 95 metres from a nuclear power reactor at the Bugey nuclear power plant in France. Three identical modules, each filled with ≈ 600 litres of liquid scintillator doped with ^{6}Li, were used: one (module 1) located under the reactor building, at 15 m from the core, and two (modules 2 and 3) outside the reactor building, inside a concrete bunker 40 m away from the core. Module 1 was also used to measure the neutrino signal from another reactor located 95 m away when the nearest reactor was stopped. A total a 150000 events were observed, which is the highest number of $\overline{\nu}_e$'s ever detected. For approximately 40% of the data taking period the measurement was done *simultaneously* at the two locations which greatly reduces the systematics due to uncertainties in the neutrino flux from nuclear burnup in the reactor. The neutrino spectra at the three distances were found to be consistent with each other, with no evidence for neutrino oscillations. The minimum excluded values for Δm^2 and $\sin^2 2\theta$ parameters at 90% confidence level are 1×10^{-2} eV^2 and 2×10^{-2} respectively [29].

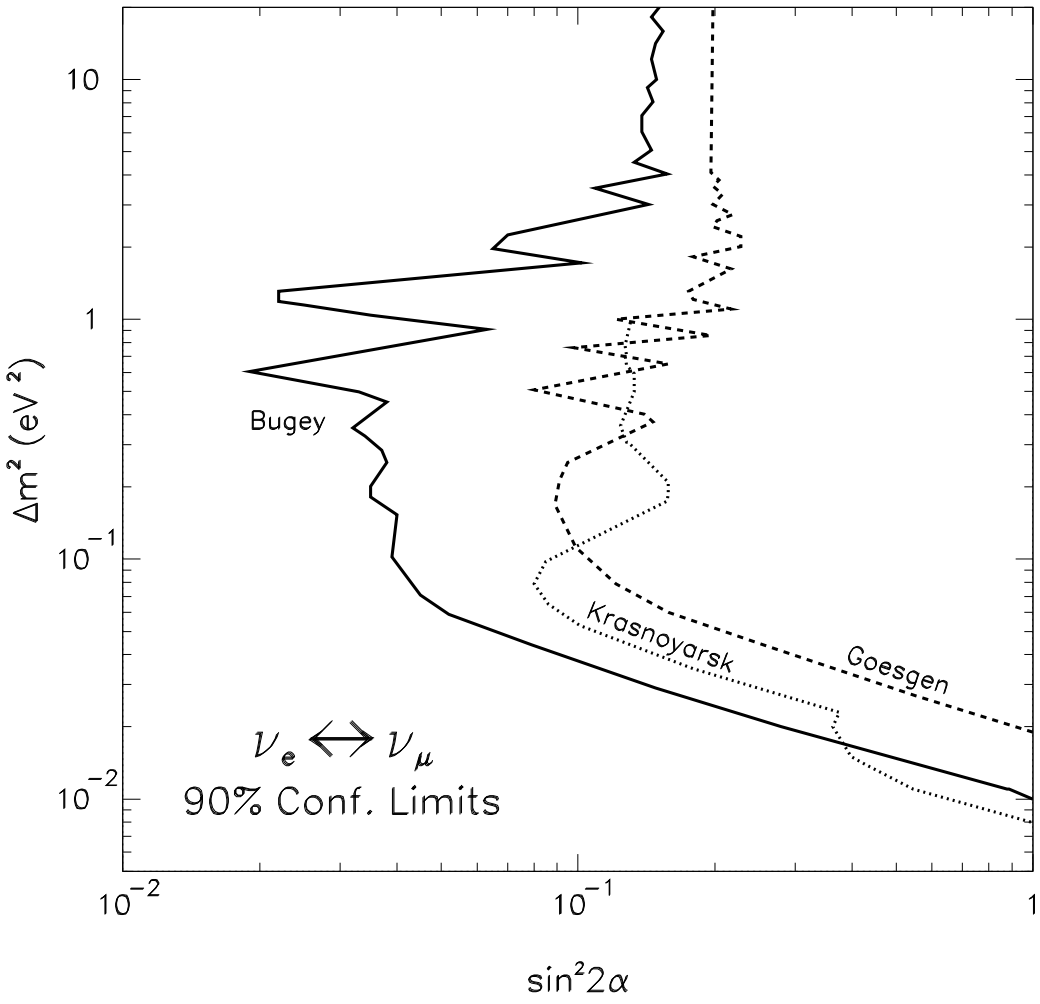

Figure 1.3: Excluded region of $\sin^2 2\alpha$ and Δm^2 for $\nu_e \rightarrow \nu_x$ oscillations from reactor experiments.

- Krasnoyarsk

  The feature that distinguishes this experiment is the fact that it employs a single detector located at distances of 57.0, 57.6, and 231.4 m from three practically identical nuclear reactors. This allowed for a complete exclusion of the systematic errors associated with the efficiency of the detector, and to greatly decrease the errors arising from insufficient knowledge of the antineutrino flux. An additional and considerable advantage of this method is that the background for all three measurements is the same. Data were taken for approximately 490 hours and no evidence for oscillations was found. At the 90% confidence level, $\sin^2 2\theta \leq 0.15$ was excluded for $\Delta m^2 \geq 5.0 \times 10^{-2}$ eV^2. At full mixing, *i.e.* $\sin^2 2\theta = 1$, $\Delta m^2 \leq 7.5 \times 10^{-3}$ eV^2 was excluded [30].

These limits are shown together in Figure 1.3. By comparing the limits from accelerator experiments and and reactor ones, we can easily see that reactor experiments are sensitive to lower mass differences ($\approx 10^{-2}$ eV^2 for distances of a few tens of metres) than experiments at accelerators primarily due to the low energy of reactor neutrinos (a few MeV). On the other hand, accelerator experiments, which compare the oscillation probability, P, directly to the data (appearance method) are more sensitive to small values of the mixing parameter than the reactor experiments, where $1 - P$ is measured.

1.4 Outline of the Thesis

This thesis presents the results of a high statistics search for $\nu_\mu \rightarrow \nu_e$ oscillations in the small mixing angle regime. The neutrino data was collected during the 1987-88 fixed target run at Fermilab with the Lab E detector by the CCFR collaboration. High energy neutrinos were provided using the Fermilab Quadrupole Triplet beamline, which focused pion and kaon secondaries produced in the collision of 800 GeV protons on a BeO target, before allowing them to decay in flight. Neutrino interactions were detected with a 690 ton total absorption

target calorimeter instrumented with liquid scintillation counters and drift chambers, which was separated from the neutrino source by approximately one kilometer of earth and steel.

The chapters of the thesis are organized as follows: Chapter 2 outlines the theory of neutrino oscillations. Chapter 3 describes the experimental apparatus, including the accelerator facilities at Fermilab, the neutrino beam and the CCFR detector. Chapter 4 describes the extraction of the ν_μ flux and the Monte Carlo simulation used to predict the ν_e flux at the detector. Chapter 5 describes the analysis procedure used to measure the ν_e flux, and the study of the systematic uncertainties. Finally, Chapter 6 describes the oscillation analysis and presents the results, which are summarized below:

- We searched for ν_e appearance in a predominantly ν_μ beam, and the results are consistent with no neutrino oscillations. We find 90% confidence level excluded regions in the $\sin^2 2\alpha - \Delta m^2$ phase space. The lowest 90% confidence upper limit in $\sin^2 2\alpha$ of 1.1×10^{-3} is obtained at $\Delta m^2 \sim 300$ eV^2. For $\sin^2 2\alpha = 1$, $\Delta m^2 > 1.6$ eV^2 is excluded, and for $\Delta m^2 \gg 1000$ eV^2, $\sin^2 2\alpha > 1.8 \times 10^{-3}$ is excluded. This result is the most stringent limit to date for $\nu_\mu \to \nu_e$ oscillation for $\Delta m^2 > 25$ eV^2.

- We also tested $\nu_\mu(\overline{\nu}_\mu) \leftrightarrow \nu_e(\overline{\nu}_e)$ universality and found the ratio of the ν_μ-to-ν_e cross-section to be $1.026 \pm 0.025(\text{stat}) \pm 0.049(\text{syst})$. This is currently the most stringent test of universality at high space-like momentum transfer.

Chapter 2

Theoretical Background

Experimentally, the neutrino is observed to participate only in the weak interactions. The first description of weak interactions was formulated by Fermi to explain the nuclear β-decay, $n \to pe\overline{\nu}$:

$$\mathcal{L}_F(x) = -\frac{G_F}{\sqrt{2}} \left[\overline{p}(x)\gamma_\lambda n(x)\right] \left[\overline{e}(x)\gamma^\lambda \nu(x)\right] + \text{h.c} \tag{2.1}$$

where the fermion field operators are denoted by their particle names, and

$$G_F \approx 10^{-5}/m_p^2 \tag{2.2}$$

is the Fermi coupling constant with m_p the proton mass.

The discovery of parity non-conservation led to the eventual formulation of the V-A theory [31]. It was suggested that the effective Lagrangian:

$$\mathcal{L}_{\text{eff}} = -\frac{G_F}{\sqrt{2}} J_\lambda^\dagger(x) J^\lambda(x) + \text{h.c.} \tag{2.3}$$

describes weak interactions, with the weak current J_λ of the vector-minus-axial form:

$$J_\lambda \sim \overline{\psi}\gamma_\mu(1-\gamma_5)\psi \tag{2.4}$$

By invoking $\frac{1}{2}(1-\gamma_5)$ as the left handed spin projection operator it becomes apparent that these weak interactions *only* involve left handed fermions and right handed antifermions. This is known as the principle of maximal parity violation. Although experimentally the

neutrinos are known to be light, it is really because of observed maximal parity violation that the neutrino is believed to be massless.

Schwinger [32] was the first to advance the idea of weak and electromagnetic unification and Glashow [33], Weinberg [34], and Salam [35] (GWS) proposed such a model which has the $SU(2)\times U(1)$ gauge symmetry. This theory is based on the requirement of $SU(2)_L\times U(1)$ local gauge invariance. Weak interactions between fermion currents are mediated by a triplet of vector particles, the charged $W^{\pm}$ ($M_W = 80.410 \pm 0.180$ [36]), and the neutral Z^0 ($M_Z = 91.187 \pm 0.007$ [37]). When a massive virtual particle is exchanged, the effective strength of the interaction is determined by the relationship between the four momentum it carries (q^2) and its mass. This is because the propagator is proportional to

$$\frac{g^2}{q^2 - M_{W,Z}^2} \tag{2.5}$$

Historically, the weak interactions were recognized as being weak because in all processes studied $q^2 \ll M_{W,Z}^2$.

The fermion currents which couple to the $W^{\pm}$ are charged while those which couple to Z_0 are neutral. These currents may consist of either leptons or quarks. The leptonic currents have the form

$$J_\mu^{\text{leptons}} = \begin{cases} \sum_{i=1}^{3} \overline{L}_i \gamma_\mu \dfrac{(1-\gamma_5)}{2} N_i & \text{charged} \\ \sum_{i=1}^{3} \overline{L}(\overline{N})_i \gamma_\mu \dfrac{(c_V^f - c_A^f \gamma^5)}{2} L(N)_i & \text{neutral} \end{cases} \tag{2.6}$$

Here L_i refers to the i^{th} charged lepton, and N_i to the corresponding neutrino. The quark current is of a similar form but the fields which enter represent six different quark flavours,

$$J_\mu^{\text{quark}} = \begin{cases} \sum_{i=1}^{3} \overline{U}_i \gamma_\mu \dfrac{(1-\gamma_5)}{2} \sum_{j=1}^{3} V_{ij} D_j & \text{charged} \\ \sum_{i=1}^{3} \overline{U}(\overline{D})_i \gamma_\mu \dfrac{(c_V^f - c_A^f \gamma^5)}{2} \sum_{j=1}^{3} V_{ij} U(D)_j & \text{neutral} \end{cases} \tag{2.7}$$

The fields represented by the U_i are the "up" quarks, u (up), c (charm), and t (top). The other three fields, the "down" quarks, d (down), s (strange), and b(bottom) are mixed with

f	c_V	c_A
ν_e, ν_μ, ν_τ	$\frac{1}{2}$	$\frac{1}{2}$
e^-, μ^-, τ^-	$-\frac{1}{2} + 2\sin\theta_W$	$-\frac{1}{2}$
u, c, t	$\frac{1}{2} - \frac{4}{3}\sin^2\theta_W$	$\frac{1}{2}$
d, s, b	$-\frac{1}{2} + \frac{3}{4}\sin^2\theta_W$	$-\frac{1}{2}$

Table 2.1: Neutral vector and axial vector couplings in the GWS model.

respect to the "up" quarks. The mixing is parametrized in terms of the unitary Cabbibo, Kobayashi and Maskawa (CKM) matrix V_{ij}. The elements of the CKM matrix are not predicted by theory and have to be measured experimentally. The coefficients c_V^f and c_A^f depend on the particular quark or lepton (f) involved (see Table 2.1). In the GWS model, *all* these numbers are determined by a single parameter θ_W, called the "weak mixing angle". The standard model provides no way to calculate θ_W; like the CKM matrix, its value is taken from the experiment. Using the on-shell renormalization scheme, $\sin^2\theta_W$, the CCFR collaboration measured the weak mixing angle to be [38]:

$$\sin^2\theta_W = 0.2218 \pm 0.0025(\text{stat}) \pm 0.0036(\text{exp.syst.}) \pm 0.0040(\text{model}) \tag{2.8}$$

This is consistent with the various measurements at LEP/SLC where $\sin^2\theta_W^{\text{on-shell}} = 0.2232 \pm 0.0018$.

There is no compelling theoretical reason, even with the GWS theory, for neutrinos to be massless and/or not to mix. Experimentally it has been observed that particular neutrinos (antineutrinos) appear to participate in reactions only with its corresponding charged leptons, and that a neutrino is different from its antiparticle. These selection rules are formalized in two empirical principles of lepton number conservation. The first principle reflects the differentiation between particles and antiparticles. We associate to these a total lepton "charge", or number

$$L_{\text{TOTAL}} = \Sigma + 1 \text{ for each particle } (-1 \text{ for each antiparticle}) \tag{2.9}$$

which is conserved in all interactions. The second principle differentiates among leptons of

different families (*i.e.* electron, muon, and tau) and associates a lepton charge with each family. Here the separate lepton numbers

$$\begin{aligned} L_e &= \Sigma +1 \text{ for } \nu_e, e^- \ (-1 \text{ for } \overline{\nu}_e, e^+) \\ L_\mu &= \Sigma +1 \text{ for } \nu_\mu, \mu^- \ (-1 \text{ for } \overline{\nu}_\mu, \mu^+) \\ L_\tau &= \Sigma +1 \text{ for } \nu_\tau, e^- \ (-1 \text{ for } \overline{\nu}_\tau, \tau^+) \end{aligned} \tag{2.10}$$

are conserved additively in all interactions. This conservation law would exclude for example $\mu \to e\gamma$ or $\overline{\nu}_\mu + e^- \to \mu^- \overline{\nu}_e$.

If neutrino oscillations exist it would mean that neutrinos would spontaneously transform among each other with harmonic probability. If this were the case, it would be a clear violation of the lepton number conservation, and it would mean that neutrinos have mass.

2.1 Deep Inelastic Scattering

To understand neutrino-nucleon scattering in terms of the GWS theory, with its neutrino-quark coupling terms, one must first understand the quark content of the nucleon. Fortunately, when the momentum squared transfered in the νN interaction is a few GeV^2 or more - the so-called deep inelastic scattering (DIS) regime - the scattering becomes well described by incoherent scattering off quasi-free quarks inside the nucleon.

The tree level diagram for charged current neutrino-nucleon scattering is shown in Figure 2.1. A neutrino (antineutrino) with incoming four-momentum k_1, scatters from a quark or antiquark in the nucleon via exchange of a $W^+(W^-)$ boson, with four-momentum q. In the lab, the variables which can be measured in the CCFR experiment for this interaction are the momentum and angle of the outgoing muon, E_μ and θ_μ, and the energy of the outgoing hadrons, E_{had}. These can be used to reconstruct the energy of the incoming neutrino, $E_\nu = E_\mu + E_{had}$. In terms of these experimental quantities, the four-momenta shown in

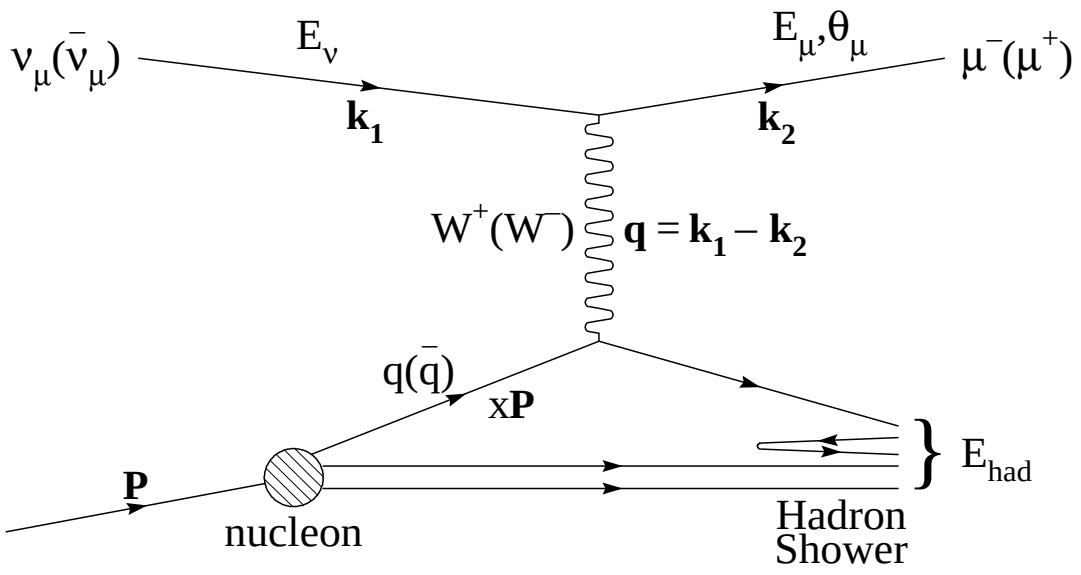

Figure 2.1: Kinematic variables of deep inelastic scattering. The struck quark carries a fraction x of the nucleon's momentum P.

Figure 2.1 are:

$$\begin{aligned} k_1 &= (E_\nu, 0, 0, E_\nu) \\ k_2 &= (E_\mu, p_\mu \sin\theta_\mu \cos\phi_\mu, p_\mu \sin\theta_\mu \sin\phi_\mu, p_\mu \cos\theta_\mu) \\ P &= (M, 0, 0, 0) \\ q &= k_1 - k_2 \end{aligned} \tag{2.11}$$

Useful Lorenz invariant variables commonly used to describe deep inelastic scattering are easily derived:

the centre-of-mass energy squared,

$$s = (P + k)^2 = M^2 + 2ME_\nu \tag{2.12}$$

the energy transfered to the hadronic system

$$\nu = \frac{P \cdot q}{M} = E_\nu - E_\mu = E_{had}, \tag{2.13}$$

the negative squared four-momentum transfer

$$Q^2 = -q^2 = -(k_1 - k_2)^2 = m_\mu^2 + 2E_\nu(E_\mu - p_\mu \cos\theta_\mu), \tag{2.14}$$

the invariant mass of the hadronic system

$$W^2 = (P + q)^2 = M^2 + 2M\nu - Q^2, \tag{2.15}$$

the Bjorken scaling variable

$$x = \frac{-q^2}{2P \cdot q} = \frac{Q^2}{2M\nu}, \tag{2.16}$$

and the inelasticity

$$y = \frac{P \cdot q}{P \cdot k_1} = \frac{E_{had}}{E_\nu}. \tag{2.17}$$

The laboratory frame expressions for the Lorenz-invariant scalars given above neglect the mass of the final state lepton. In an inclusive measurement, where the specific makeup of the final state hadrons is not considered, the kinematics of an event are specified by 3 independent variables, *e.g.* E, x, and y or E, x, and Q^2.

2.2 Models of Neutrino Masses

There are two general ways to generate neutrino masses. First, one modifies the Higgs sector in the standard model. For example, an additional singlet, doublet, or triplet with or without right-handed neutrinos can be added to the original Higgs doublet in the standard model. In this case one is forced to introduce a new mass scale in the form of the vacuum expectation value. This, however, is not an explanation of the small neutrino mass. The other possibility is to utilize extremely heavy right-handed neutrinos which appear in models such as left-right symmetry models or GUTs. In the past, there have appeared numerous papers on the theory of neutrino mass. For recent reviews one can see, for example, [39], [40], and [41]. The major models, along with the most natural scales for the neutrino masses are listed in Table 2.2 [42]. In the following, we list several ways to *describe* the neutrino mass [43].

Model	m_{ν_e}	m_{ν_μ}	m_{ν_τ}
Dirac	1 - 10 MeV	100 MeV - 1 GeV	1 - 100 GeV
pure Majorana (Higgs triplet)	arbitrary	arbitrary	arbitrary
GUT seesaw ($M \sim 10^{14}$ GeV	10^{-11} eV	10^{-6} eV	10^{-3} eV
intermediate seesaw ($M \sim 10^{9}$ GeV)	10^{-7} eV	10^{-2} eV	10 eV
TeV seesaw ($M \sim 1$ TeV)	10^{-1} eV	10 KeV	1 MeV
light seesaw ($M \ll 1$ GeV)	1 - 10 MeV	–	–
charged Higgs	< 1 eV	–	–

Table 2.2: Models for neutrino mass, along with their most natural scales for the light neutrino masses.

2.2.1 Dirac Mass

The simplest way to describe the mass is to introduce right-handed neutrinos. The mass term of the Lagrangian is:

$$\mathcal{L}_{\text{Dirac}} = -(\overline{\nu}_L \mathcal{M} \nu_R + \overline{\nu}_R \mathcal{M}^\dagger \nu_L), \tag{2.18}$$

where $\nu_{L,R}$ are given by

$$\nu_{L,R} = \begin{pmatrix} \nu_e \\ \nu_\mu \\ \nu_\tau \end{pmatrix}_{L,R} \tag{2.19}$$

In general $\mathcal{M}$ is a 3×3 complex mass matrix, and there is no guarantee that the mass eigenstates are positive. One needs to bi-diagonalize $\mathcal{M}$ using two unitary matrices U and V:

$$U^\dagger \mathcal{M} V = m_D = \begin{pmatrix} m_1 & 0 & 0 \\ 0 & m_2 & 0 \\ 0 & 0 & m_3 \end{pmatrix}, \tag{2.20}$$

where U and V relate the mass eigenstates $\nu_{L,R}^{(m)}$ to the weak eigenstates ν_L as

$$\begin{aligned} \nu_L &= U \nu_L^{(m)} \\ \nu_R &= V \nu_R^{(m)} \end{aligned} \tag{2.21}$$

The diagonalized mass Lagrangian is:

$$\mathcal{L}_{\text{Dirac}} = -\overline{\nu}_L^{(m)} m_D \nu_R^{(m)} + \text{h.c.} \tag{2.22}$$

Since only ν_L is involved in the weak interactions, U is the Cabbibo, Kobayashi and Maskawa mixing matrix. Since there is no evidence for the existence of ν_R we simply assume that it couples to matter much more weakly than ν_L and may be very massive. A charged current composed of these other components would have the space-time structure of a vector *plus* an axial vector (V+A). The implication is that the $W_R^{\pm}$ which couple to these V+A charged current interactions are much heavier than the observed $W^{\pm}$. Equation 2.5 implies that these right handed weak interactions remain weak until a much higher q^2 is exchanged. The best limits to date on the mass of the right-handed boson W_R come from Tevatron searches by the D0 and CDF collaborations. Assuming maximal mixing between the right-handed boson and the left-handed counterpart, the Standard Model W boson, the D0 collaboration sets a lower limit on M_{W_R} of 720 GeV/c^2 [44] which can be compared with the limit set by CDF of 652 GeV/c^2 [45].

2.2.2 Majorana Mass

The neutrino is in general assumed to be a Dirac particle, different from its antiparticle. It is possible for the neutrino to be its own antiparticle, or a Majorana particle [46]. In this case, the neutrino is a single particle, and its two states can just be the two helicity states of a massive fermion. The Majorana neutrino mass can be described by the use of ν_L alone:

$$\mathcal{L}_{\text{Majorana}} = -\frac{1}{2}\overline{\nu^C}_L \mathcal{M} \nu_L + \text{h.c.} \tag{2.23}$$

where ν_L^C is a right-handed neutrino. For this case $\mathcal{M}$ is symmetric and diagonalization can be done by a single unitary matrix U with

$$\nu_L = U \nu_L^{(m)} \tag{2.24}$$

Equation 2.23 becomes

$$\mathcal{L}_{\text{Majorana}} = -\frac{1}{2}\left[\overline{\nu^C}_L m_D \nu_L + \overline{\nu_L} m_D \nu_L^C\right]. \tag{2.25}$$

Defining

$$\nu_{\text{Maj}} \equiv \nu_L + \nu_L^C \tag{2.26}$$

which is clearly a Majorana neutrino, we can rewrite

$$\mathcal{L}_{\text{Majorana}} = -\frac{1}{2}\overline{\nu}_{\text{Maj}} m_D \nu_{\text{Maj}} \tag{2.27}$$

Although this expression looks similar to that of Eq. 2.18 the oscillations of the two types of neutrinos posses a somewhat different phenomenology. In the case of a Dirac neutrino, the oscillations violate the separate lepton flavour conservation rules. For a Majorana neutrino it is also possible to violate the total lepton number.

2.2.3 Dirac-Majorana Mass

In a one generation case , the Lagrangian of interest is

$$\mathcal{L}_{D-M} = -M\overline{\nu}_L \nu_R - \frac{1}{2}\left(m_L \overline{\nu}_L^C \nu_L + m_R \overline{\nu}_L^C \nu_R\right) + \text{h.c.} \tag{2.28}$$

where M is the Dirac mass and $m_L(m_R)$ are Majorana masses. If we define a left-handed neutrino state ν as

$$\nu \equiv \begin{pmatrix} \nu_L \\ \nu_R^C \end{pmatrix}, \tag{2.29}$$

the Dirac-Majorana Lagrangian looks like that for the Majorana case:

$$\mathcal{L} = -\frac{1}{2}\overline{\nu}^C \mathcal{M} \nu + \text{h.c.} \tag{2.30}$$

where the mass matrix $\mathcal{M}$ is

$$\mathcal{M} = \begin{pmatrix} m_L & M \\ M & m_R \end{pmatrix}. \tag{2.31}$$

Diagonalizing $\mathcal{M}$ yields

$$\begin{aligned} m_1 &= \frac{1}{2}\sqrt{4M^2+(m_R-m_L)^2} - \frac{m_L+m_R}{2} \\ m_2 &= \frac{1}{2}\sqrt{4M^2+(m_R-m_L)^2} + \frac{m_L+m_R}{2} \end{aligned} \tag{2.32}$$

Now, the mass eigenstate $\nu^{(m)}$ can be defined as

$$\begin{aligned} \nu^{(m)} &= \begin{pmatrix} \nu_1 \\ \nu_2 \end{pmatrix} = U\nu \\ &= \begin{pmatrix} \cos\theta\,\nu_L - \sin\theta\,\nu_R^C \\ \sin\theta\,\nu_L + \cos\theta\,\nu_R^C \end{pmatrix}, \end{aligned} \tag{2.33}$$

where the mixing angle is given by $\tan 2\theta = \frac{2M}{m_R - m_L}$. We can distinguish between two different cases:

1. Case with $M \gg m_L, m_R$. In this case m_1 and m_2 are almost degenerate in mass (Eq. 2.32 implies $m_1 \simeq m_2 \simeq M$) and ν_1 and ν_2 have opposite CP phase. This case is called special pseudo-Dirac neutrino [47] and we have a half active ν_L and a half sterile ν_R.

2. Case with $m_R \gg M, m_L$. If we assume for simplicity that $m_L = 0$, then we have

$$\begin{aligned} m_1 &\simeq \frac{M^2}{m_R} \\ m_2 &\simeq m_R \end{aligned} \tag{2.34}$$

   implying that m_1 is naturally small and m_2 is large. Since $\theta \simeq 0$, ν_L and ν_R^C are practically decoupled. This is the seesaw mechanism [48].

2.2.4 Seesaw Mechanism

We can extend the above to the three generation case by writing

$$m_1 = \frac{M^2}{m_R} \rightarrow \overline{m}_1 = \overline{M}\frac{1}{\overline{m}_R}\overline{M}^T \tag{2.35}$$

where all barred objects are 3×3 matrices and as before we assume $|(\overline{m}_R)_{ij}| \gg |\overline{M}_{ij}|$. The matrix analogous to Eq. 2.31 is a 6×6 mass matrix $\overline{\mathcal{M}}$ given by

$$\overline{\mathcal{M}} = \begin{pmatrix} 0 & \overline{M} \\ \overline{M} & \overline{m}_R \end{pmatrix}. \tag{2.36}$$

One can consider two possible cases:

1. There is no mass hierarchy among the right-handed neutrinos, *i.e.*

$$\overline{m}_R \simeq m_R \begin{pmatrix} 1 & 0 & 0 \\ 0 & 1 & 0 \\ 0 & 0 & 1 \end{pmatrix}, \tag{2.37}$$

   implying

$$m(\nu_1) : m(\nu_2) : m(\nu_3) = \frac{m_u^2}{m_R} : \frac{m_c^2}{m_R} : \frac{m_t^2}{m_R}. \tag{2.38}$$

   this is called the quadratic seesaw mechanism.

2. The right-handed neutrinos have a mass hierarchy similar to that of the quarks, *i.e.*

$$\overline{m}_R \simeq \overline{m}_R \begin{pmatrix} \frac{m_u}{m} & 0 & 0 \\ 0 & \frac{m_c}{m} & 0 \\ 0 & 0 & \frac{m_t}{m} \end{pmatrix}. \tag{2.39}$$

   In this case we have:

$$m(\nu_1) : m(\nu_2) : m(\nu_3) = \frac{m_u}{m_R} : \frac{m_c}{m_R} : \frac{m_t}{m_R} \tag{2.40}$$

   which is called the linear seesaw mechanism.

The above relations as give by Eqs. 2.38 and 2.40 are valid at the GUT scales which means that one has to bring them down to the low energy region using the Renormalization Group Equations (RGE). If, for example, we consider only the running of the mass in one-loop calculations then Eq. 2.38 is modified as [49]

$$m(\nu_1) : m(\nu_2) : m(\nu_3) = \begin{cases} 0.05\frac{m_u^2}{m_R} : 0.09\frac{m_c^2}{m_R} : 0.38\frac{m_t^2}{m_R} & SUSY\ SU(5) \\ 0.05\frac{m_u^2}{m_R} : 0.07\frac{m_c^2}{m_R} : 0.18\frac{m_t^2}{m_R} & SO(10) \end{cases} \tag{2.41}$$

As we can see from the above, the corrections due to the RGE depend on the choice of the model. In general, the actual size of the neutrino masses will be determined by the

mass scale for m_R which depends on the Yukawa coupling, the GUT vacuum expectation value, and the gauge coupling constant. m_R is in general expected to be in the range of $10^{10} - 10^{15}$ GeV which would explain the (possibly) small neutrino mass.

2.3 Theory of Neutrino Oscillations

Neutrino oscillations are an example of a common quantum phenomenon, namely that if one starts at time $t = 0$ in a state that is not an energy eigenstate then at later times the state can evolve (oscillate) into another orthogonal state. From this point of view neutrino oscillations are analogous to $K^0 \rightleftharpoons \overline{K}^0$ mixing.

If neutrinos have mass, then in general the mass eigenstates need not be the same as the weak interaction eigenstates. If the weak eigenstates are mixtures of mass eigenstates, then separate electron, muon, and tau numbers will not be conserved; however, the sum of the three, the lepton number, will be conserved just as the baryon number is conserved in the quark sector. Suppose the state vectors of the neutrinos taking part in the weak interaction are superpositions of the state vectors of neutrinos with different masses. In this case, the neutrino associated with the α^{th} charged lepton ν_α can be expressed as:

$$|\nu_\alpha\rangle = \sum_i U_{\alpha i} |\nu_i\rangle \tag{2.42}$$

where ν_i is the field of a Dirac neutrino with mass m_i, and U is a unitary "neutrino mass mixing matrix" that transforms between the weak interaction (flavour) eigenstates (ν_α) and the mass eigenstates (ν_i). For antineutrinos there is an equation analogous to Eq. 2.42 with the replacements $\nu \to \overline{\nu}$ and $U \to U^*$.

The time evolution of a state is controlled by its energy eigenvalues. We assume that all neutrinos in the beam have a common fixed momentum p; then the mass eigenstates have energy eigenvalue

$$E_i^2 = p^2 + m_i^2 \tag{2.43}$$

If at the initial moment $t = 0$ the flavour neutrinos are described by the state vector $|\nu_\alpha\rangle$, at the moment t they will be described by

$$|\nu_\alpha(t)\rangle = e^{-iH_0 t}|\nu_\alpha(0)\rangle \tag{2.44}$$

where H_0 is the free Hamiltonian, with

$$H_0|\nu_i\rangle = E_i|\nu_i\rangle \tag{2.45}$$

From Eqs. 2.42, 2.44, and 2.45 we get:

$$|\nu_\alpha(t)\rangle = \sum_{k=1}^{3} U_{\alpha k} e^{-iE_k t}|\nu_k\rangle \tag{2.46}$$

To obtain the probability amplitude of finding a neutrino in a given flavour state we have to decompose $|\nu_\alpha(t)\rangle$ over the complete set of neutrino flavour state vectors. Using the unitarity of the transformation matrix U we can expand the mass eigenstates $|\nu_k\rangle$ into flavour eigenstates

$$|\nu_k\rangle = \sum_{\beta=e,\mu,\tau} U^*_{\beta k}|\nu_\beta\rangle \tag{2.47}$$

Thus, we may write the flavour eigenstates at time t as:

$$|\nu_\alpha(t)\rangle = \sum_{\beta=e,\mu,\tau} |\nu_\beta\rangle \sum_{k=1}^{3} U_{\alpha k} e^{-iE_k t} U^*_{\beta k} \tag{2.48}$$

If a flavour state α is produced at time $t = 0$, the amplitude for finding a state of flavour β at a later time t is:

$$A(\nu_\alpha \to \nu_\beta) =< \langle \nu_\beta(t)|\nu_\alpha(0)\rangle = \sum_{k=1}^{3} U_{\beta k} e^{-iE_k t} U^*_{\alpha k} \tag{2.49}$$

The transition probability P is the absolute square of this amplitude:

$$P(\nu_\alpha \to \nu_\beta) = |< \langle nu_\beta(t)|\nu_\alpha(0)\rangle|^2 = \left| \sum_{k=1}^{3} U_{\beta k} e^{-iE_k t} U^*_{\alpha k} \right|^2 \tag{2.50}$$

If we assume that $m_k \ll p$, and keep only terms linear in m_k^2/p^2, we have

$$E_k \simeq p + \frac{m_k^2}{2p} \tag{2.51}$$

Substituting back into the probability equation, one obtains:

$$P(\nu_\alpha \to \nu_\beta) = \sum_{k=1}^{3} |U_{\alpha k}|^2 + |U_{\beta k}|^2 + Re \sum_{i \neq j} U_{\beta i} U^*_{\alpha i} U^*_{\beta j} U_{\alpha j} e^{\frac{-i(m_i^2 - m_j^2)L}{2p}} \tag{2.52}$$

where L is the pathlength of the neutrino. From Eq. (2.52) it is easy to see that neutrinos of a given type may undergo transition in vacuum into neutrinos of a different type only if (i) there exist at least two neutrinos that are nondegenerate in mass; (ii) neutrino mixing does take place (*i.e.* at least some non-diagonal elements of the lepton mixing matrix are different from zero). If we assume that $p/L \gg |m_j^2 - m_k^2|$, $j \neq k$, $j, k = 1, 2, 3$ then $P_{\nu_\alpha \to \nu_\beta} = \delta_{\alpha\beta}$. Thus the effects of neutrino oscillations are observable only if at least one difference of the square of neutrino masses is of the order of or greater than p/L.

2.3.1 Oscillations between two types of neutrinos

Let us begin with the simplest possibility of oscillations involving two types of neutrinos:

$$\nu_\alpha \leftrightarrow \nu_\beta, \qquad \alpha \neq \beta \tag{2.53}$$

If the neutrinos with definite masses ν_1 and ν_2 are Dirac particles, the mixing matrix U is a real unitary 2×2 matrix. It has the following general form:

$$U = \begin{pmatrix} \cos\theta & \sin\theta \\ -\sin\theta & \cos\theta \end{pmatrix} \tag{2.54}$$

The angle θ is the leptonic mixing angle (leptonic equivalent of the Cabibbo angle). It follows from Eqs. 2.54 and 2.42 that the flavour states ν_α and ν_β can be expressed in terms of the neutrino states with definite masses ν_1 and ν_2 by the relations:

$$\begin{array}{rcl} \nu_\alpha & = & \nu_1 \cos\theta + \nu_2 \sin\theta, \\ \nu_\beta & = & -\nu_1 \sin\theta + \nu_2 \cos\theta. \end{array} \tag{2.55}$$

From the general expression 2.52 for the transition probability we obtain for the case under consideration:

$$P(\nu_\alpha \to \nu_\beta) = \sin^2 2\theta \sin^2 \left(\frac{1.27 \Delta m^2 L}{E_\nu} \right) \tag{2.56}$$

where $\Delta m^2 = |m_1^2 - m_2^2|$, with m_1 and m_2 being the neutrino masses, is in units of eV^2, L is the distance between the point of creation and detection in km, and $E_\nu \simeq p$ is the neutrino energy. In practice, this expression must always be integrated over the energy distribution of the incoming neutrinos.

2.3.2 Oscillations involving three types of neutrinos

Since there are three generations of neutrinos, it is possible to consider effects of mixing among the three species of neutrinos in the analysis of oscillation results.

In a massive three Dirac neutrino (real?) world, with the three charged leptons equal to their mass eigenstates we have for the mass part of the Lagrangian:

$$\mathcal{L}_{\text{Mass}}^{\text{Dirac}} = \sum_{l_i=1}^{3} m_{l_i} \bar{l}_i l_i + \sum_{l_i=1}^{3} \sum_{l_j=1}^{3} m_{\nu_{l_i,l_j}} \overline{\nu}_{l_i} \nu_{l_j} \tag{2.57}$$

where l_i refer to the three charged leptons e, μ, and τ. The neutrino mass matrix has seven independent real elements. It is diagonalized by U_{ij}, the unitary 3×3 mixing matrix. The oscillation phenomenon will then be described by the three mass eigenvalues m_1, m_2, and m_3 and the four independent elements of U_{ij}, taken to be the three angles θ_1, θ_2, θ_3 and a phase δ. This is analogous to the Kobayashi-Maskawa three quark mixing scheme. The matrix U_{ij} then takes the form:

$$U = \begin{pmatrix} c_1 & s_1 c_3 & s_1 s_3 \\ -s_1 c_2 & c_1 c_2 c_3 - s_2 s_3 e^{i\delta} & c_1 c_2 s_3 + s_2 c_3 e^{i\delta} \\ -s_1 s_2 & c_1 s_1 c_3 + c_2 s_3 e^{i\delta} & c_1 s_2 s_3 - c_2 c_3 s_3 - c_2 c_3 e^{i\delta} \end{pmatrix} \tag{2.58}$$

here, $c_i = \cos\theta_i$, $s_i = \sin\theta_i$ $i = 1, 2, 3$), and δ is the phase characterizing the violation of CP invariance. The indices $i = 1, 2, 3$ can be assigned arbitrarily to the mass eigenstates ν_i, as far as $\theta_i \in [0, \pi/2]$.

The three generations case can be better understood in a less general but more manageable framework obtained in the limit [50]

$$\left| m_2^2 - m_1^2 \right| \ll \left| m_3^2 - m_{1,2}^2 \right| \equiv m^2 \tag{2.59}$$

sometimes called "one mass-scale dominance". This equation can hold both for $m_3^2 < m_1^2 \simeq m_2^2$ and for $m_1^2 \simeq m_2^2 < m_3^2$, although only the latter case (corresponding to a natural mass hierarchy) is theoretically appealing, being motivated by the seesaw mechanism and by analogy with the charged fermion masses.

The probability of oscillation P, defined as $P = P(\nu_\alpha \to \nu_\beta) \equiv P_{\alpha\beta}$ for appearance experiments, and as $P = 1 - P(\nu_\alpha \to \nu_\alpha) \equiv 1 - P_{\alpha\alpha}$ for disappearance experiments ($\alpha, \beta = e, \mu, \tau$), is then given by:

$$\begin{array}{ll} P = 4U_{\alpha 3}^2 U_{\beta 2}^2 S & \text{(appearance)} \\ P = 4U_{\alpha 3}^2 (1 - U_{\alpha 3}^2) S & \text{(disappearance)} \end{array} \tag{2.60}$$

where S is the oscillation factor $S = \sin^2(1.27 m^2 L/E)$. As far as a single experiment is concerned, the oscillation probability P reduces to the simple two-generation form of Eq. 2.56 through the replacements:

$$\begin{array}{ll} \sin^2 2\theta \Leftrightarrow 4U_{\alpha 3}^2 U_{\beta 3}^2 & \text{(appearance)} \\ \sin^2 2\theta \Leftrightarrow 4U_{\alpha 3}^2 (1 - U_{\alpha 3}^2) & \text{(disappearance)} \end{array} \tag{2.61}$$

and the obvious identification $\Delta m^2 \equiv m^2$. Thus the one mass-scale dominance can be considered as the simplest three-flavour extension of the two-flavour scenario but with oscillation allowed between all three flavours.

In general, it is not possible to place stringent limits on oscillations in the three generation formalism from the results of one experiment. A positive result for $\nu_\mu \to \nu_e$ need not imply a direct oscillation between these flavours, it might instead result from the sequence $\nu_\mu \to \nu_\tau \to \nu_e$. In the "one mass-scale dominance" scheme, the above sequence could actually proceed more rapidly than a direct oscillation. Conversely, a negative result in the three generation case, when interpreted in terms of two generations could overestimate the significance of the experiment. For example, if an experiment were just sensitive enough to detect $\nu_\mu \to \nu_e$, but this oscillation was followed rapidly by $\nu_e \to \nu_\tau$ and $\nu_\tau \to \nu_\mu$, a null experiment result would be obtained. Thus oscillation limits calculated for the two generation case are too restrictive in the more general case of three generations. For these

reasons, the interpretation of oscillation parameters in the three generation formalism is usually made from data combined from different experiments. For this analysis we restrict ourselves to the two generation formalism.

Chapter 3

The Neutrino Beam and Detector

The CCFR detector [51, 52] consists of an 18 m long, 690 ton total absorption target calorimeter with a mean density of 4.2 g/cm^3, followed by a 10 m long iron toroidal spectrometer (see Figure 3.1).

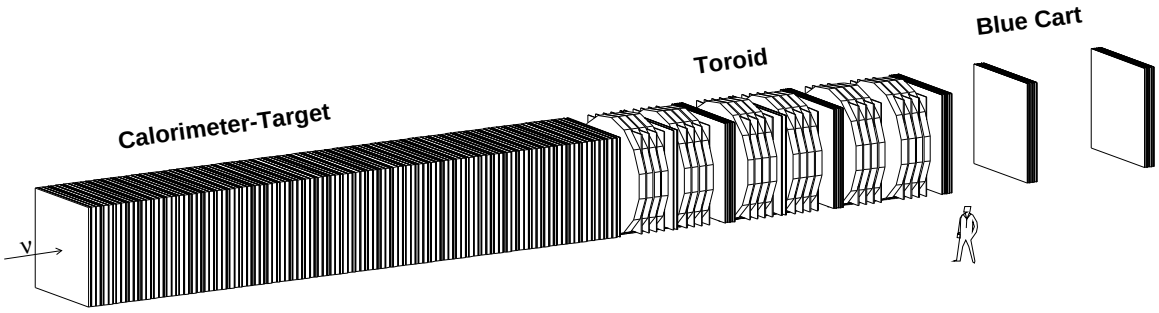

Figure 3.1: Schematic representation of the CCFR detector. The neutrino beam enters from the left. The target-calorimeter is on the left and the muon spectrometer (toroid) is on the right. The two rightmost banks of drift chambers are known as the blue cart.

3.1 Neutrino Beam

The experiment was carried out at the Fermilab Tevatron which, at least for now (1996), is the highest energy accelerator in the world. For the fixed target run protons were accelerated in the Tevatron in a series of discrete steps to 800 GeV. A schematic diagram of the Fermilab accelerator complex is show in Figure 3.2. Below is a description of the various stages used

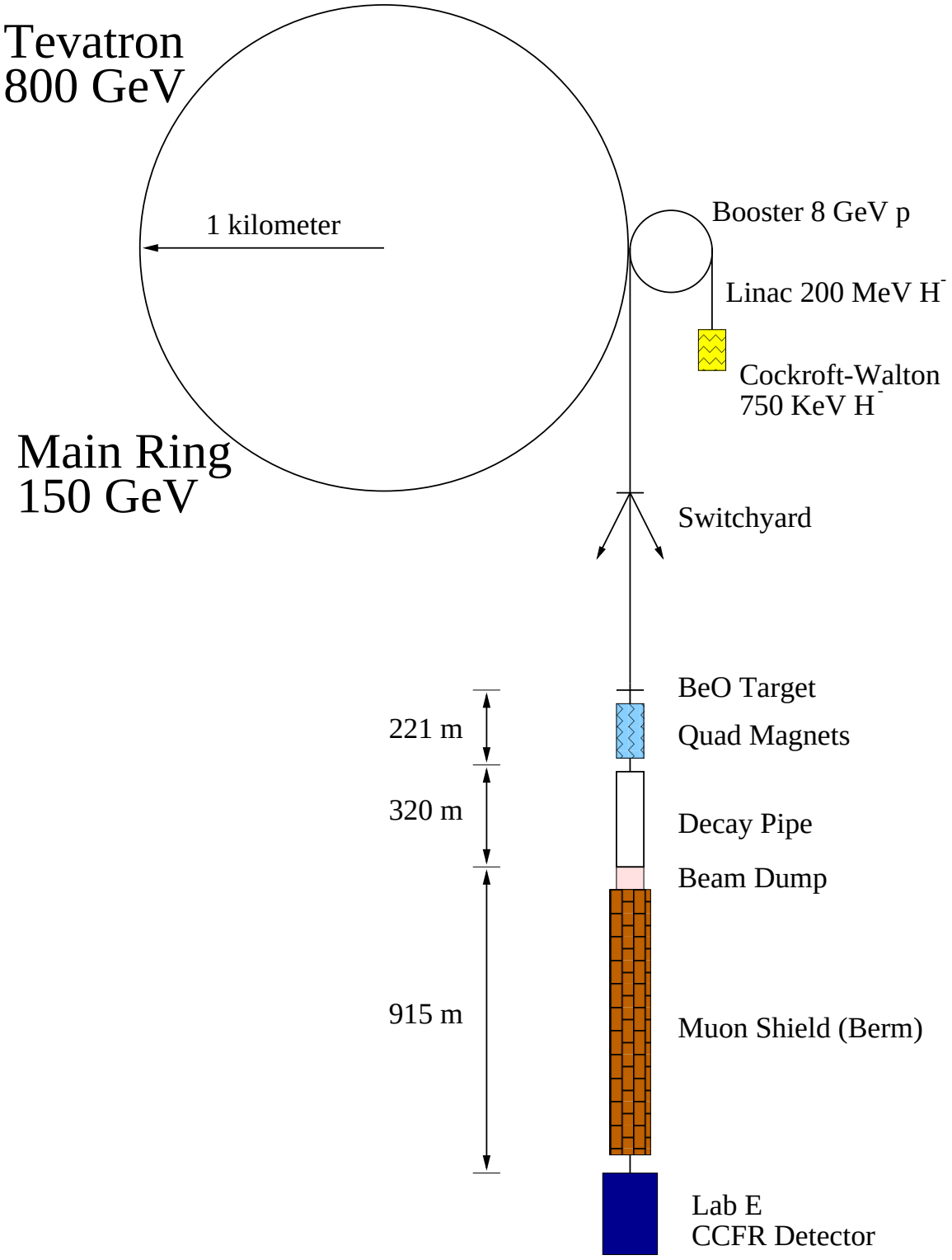

Figure 3.2: The Fermilab Tevatron and neutrino-beamline.

to accelerate the proton beam:

- ION SOURCE: H^- ions are produced by a cesium cathode immersed in a hydrogen gas.
- COCKROFT-WALTON ACCELERATOR: Collects H^- ions from the source through multiple electrostatically induced potential drops and accelerates them to 750 KeV.
- LINAC: A linear accelerator which increases the energy of the H^- ions to 200 MeV. As the ions exit the LINAC, they pass through a carbon foil which strips them of their two electrons.
- BOOSTER: The Booster ring is a 140 m diameter synchrotron which accelerates the protons to 8 GeV. A synchrotron is a cyclic machine in which the particle beam is confined to a closed orbit by a series of bending magnets. On each pass around the ring the particles' momenta are increased by acceleration in a synchronized rf cavity. As the momentum increases, the magnetic field in the bending magnets has to be increased to keep the radius of curvature constant.
- MAIN RING: The main ring is a 1 km radius synchrotron which accelerates the protons to 150 GeV. Prior to the construction of the Tevatron, the main ring served as Fermilab's primary accelerator.
- TEVATRON RING The Tevatron is a superconducting proton synchrotron. It shares the tunnel with the main ring and it is situated immediately below it. The accelerator was designed to accelerate particles to 1 TeV. For this experiment, the protons were accelerated only to 800 GeV.

During each 60 second acceleration cycle, the accelerator delivered three 2 ms bursts of protons (pings) to the neutrino beamline over a 20 s interval. The acceleration and extraction cycles are shown in Figure 3.3, where the times listed are with respect to an accelerator

reference time T1; P1, P2, and P3 indicate the ping times. The experiment took neutrino data only during the pings to minimize the background from cosmic rays. Data were also taken during beam off period for a pedestal gate (PED), and a cosmic ray gate (CR) for subtraction of cosmic ray background taken during the fast spill. The cosmic ray gate was approximately one third the length of the data gate.

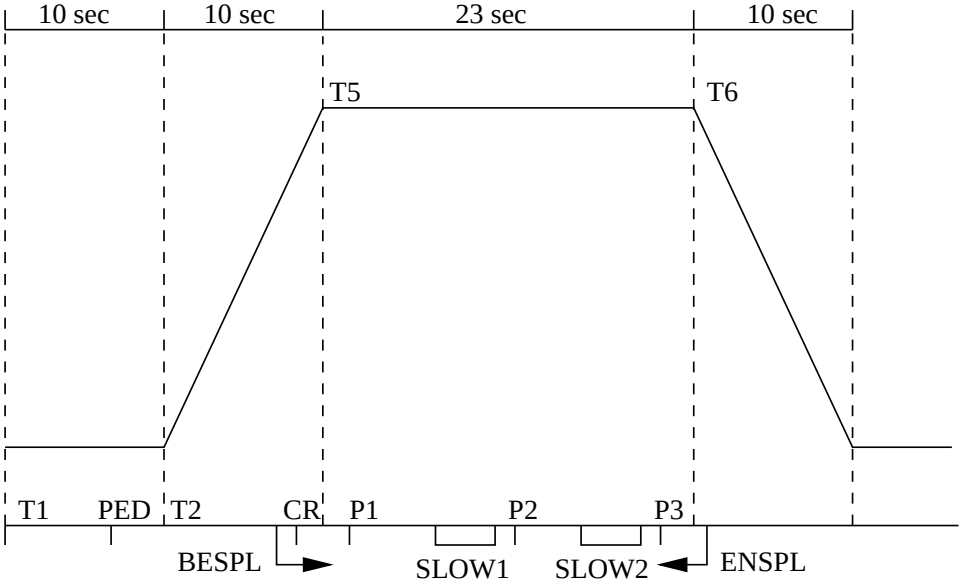

Figure 3.3: Tevatron magnet current versus time during fixed target operation. P1, P2, and P3 are the ping extraction times. BESPL and ENSPL are the beginning and the end of the spill respectively.

The Tevatron Quadrupole Triplet neutrino beam is created when 800 GeV protons hit a 30.5 cm thick beryllium oxide target producing a secondary beam of pions, kaons and other hadrons. A wide band of secondary energies is accepted by focusing magnets. The E770 beam-line consists of seven quadrupole magnets. These magnets focus in one transverse direction and defocus in the orthogonal direction. A train of quadrupoles with alternating focusing direction provides net focusing for particles of both charge signs. The beam-line was configured to optimally focus 300 GeV secondaries without sign or momentum selection such that the acceptance is maximal; this configuration gives a *wide-band beam*. A schematic of the Fermilab neutrino beamline is shown in Figure 3.4.

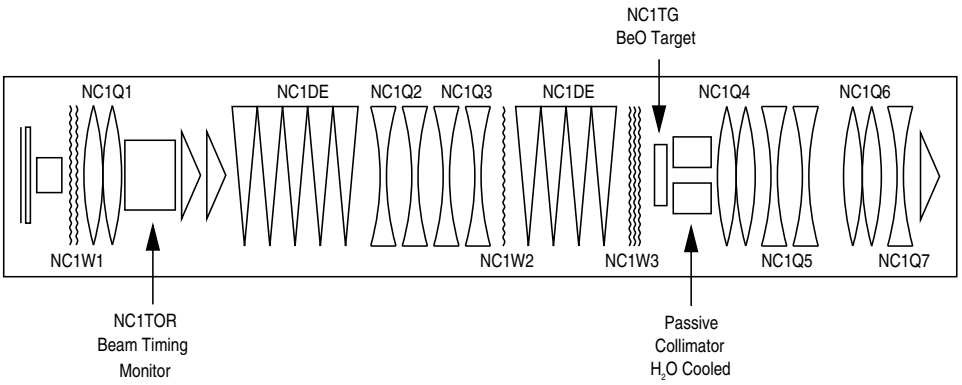

Figure 3.4: The E770 quadrupole-triplet beam-line. Dipole magnets are indicated by prisms and quadrupole magnets are indicated by concave and convex lenses.

After focusing, the pions and the kaons enter a 541 m long decay pipe, where they decay in flight with dominant decay modes:

$$\begin{array}{lcll} \pi^+ & \rightarrow & \mu^+\nu_\mu & \mathrm{BR} = 99.99\% \\ K^+ & \rightarrow & \mu^+\nu_\mu & \mathrm{BR} = 63.5\% \end{array} \tag{3.1}$$

with $\overline{\nu}_\mu$ being produced by the decays of K^- and π^-. The maximum neutrino energy is governed by the mass ratio of the muon and the decaying particle:

$$E_\nu^{max} = E_{\pi,K}\left[1 - \left(\frac{m_\mu}{m_{\pi,K}}\right)^2\right] \tag{3.2}$$

such that the neutrino beam exhibits a dichromatic spectrum, with the more energetic neutrinos coming from the kaon decays:

$$\begin{array}{lcl} (E_\nu^{max})_K & = & 0.95E_K \\ (E_\nu^{max})_\pi & = & 0.43E_\pi \end{array} \tag{3.3}$$

Approximately 3% of the mesons decay in the decay region and the remainder of the beam is dumped into a 6m block of aluminum. The muons range out in a 241m of steel shielding and 582m of earth berm. The amount of material in front of the detector is sufficient to range out all the muons produced in the decay of the mesons, allowing only the neutrinos to penetrate to the experimental area. Unfortunately neutrinos may interact in the berm, and a small number of berm muons also enter the experimental hall. Events due

to muons are identified in the veto wall, a set of scintillation counters positioned upstream of the target-calorimeter.

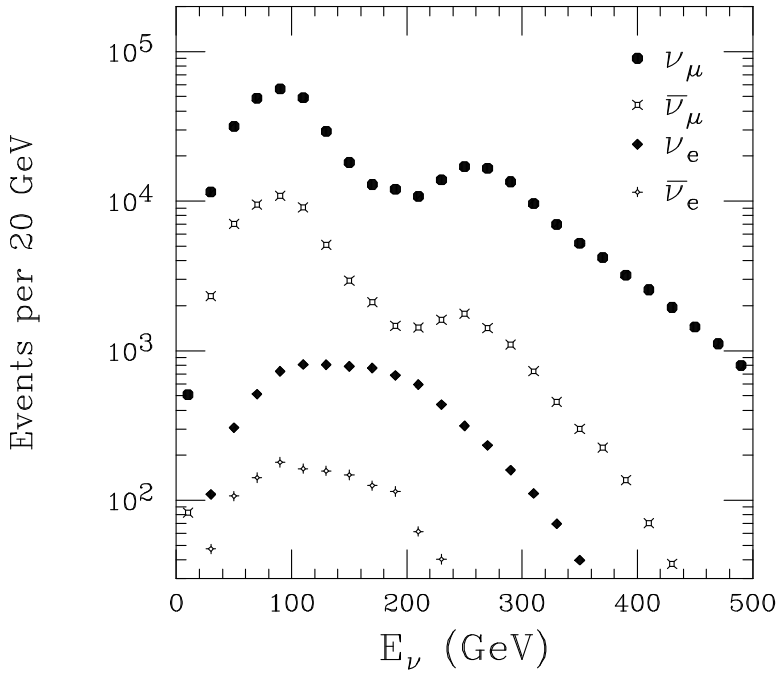

Figure 3.5: Neutrino energy spectra for ν_μ, $\overline{\nu}_\mu$, ν_e, and $\overline{\nu}_e$ at the CCFR detector for the FNAL wideband neutrino beam (Monte Carlo based on measure relative ν_μ and $\overline{\nu}_\mu$ fluxes).

The resulting neutrino energy spectra for interacting ν_μ, $\overline{\nu}_\mu$, ν_e, and $\overline{\nu}_e$ are shown in Figure 3.5. Approximately 86.4% of the E770 final event sample came from ν_μ interactions, and 11.3% from $\overline{\nu}_\mu$. Antineutrino-induced events were suppressed relative to neutrinos by lower negatively charged secondary production rates and a factor of two supression in the ν_μ to $\overline{\nu}_\mu$ total cross-section. The neutrino beam also contains a 2.3% fraction of electron neutrinos from $K^0(\overline{K}^0$, $K^\pm$ decays and a negligible fraction of tau neutrinos (less than 10^{-5}) which result primarily from D_s decay. Eighty percent of the produced ν_e's came from the three body decay mode of the charged kaons:

$$K^+ \rightarrow \pi^0 + e^+ + \nu_e \tag{3.4}$$

(with a branching ratio of 4.8%), 16% from neutral kaons:

$$K^0 \rightarrow \pi^- + e^+ + \nu_e \tag{3.5}$$

and the remaining 4% from the decays of charmed mesons, μ's, π's, Λ's, and Σ^-'s. The procedure used to determine the neutrino flux is described in more detail in chapter 4.

3.2 The Calorimeter Target

The target calorimeter is 17.7 m long, measures 3 m by 3 m transversally, has a mean density of 4.2 g/cm^3, and is centred on the neutrino beam axis. It consists of 674 tonnes of iron instrumented with 84 liquid scintillation counters and 42 drift chambers, each with an x and y plane. The iron provides the target mass required to produced a large sample of neutrino interactions; the counters and the drift chambers provide event energy and position measurements respectively. The target is segmented longitudinally into six identical modules which can be moved sideways independent of each other. Each module contains 28 iron plates, 14 liquid scintillation counters spaced every two plates and 7 drift chambers spaced every four plates. Each iron plate is 5.1 cm thick. The scintillation counters and drift chambers cover the whole transverse area of the target; along the beam axis each scintillation counter and drift chamber occupies 6.48 cm and 8.87 cm respectively. A schematic view of one target module is shown in Figure 3.6.

When a neutrino interacts with a quark in the target, the struck quark "hadronizes" on a microscopic scale of $\simeq 10^{-15}$ m producing several hadrons, predominantly charged and neutral pions. The charged pions interact to produce further pions, with a mean interaction length of approximately 20 cm of iron ($\simeq$ 2 counters). This cascade continues for several interaction lengths, until the energy of the pions is below the threshold energy to produce further pions. The pions are then stopped and their energy absorbed in the calorimeter. The neutral pions produced in the shower all decay immediately to $\gamma\gamma$ which interact producing

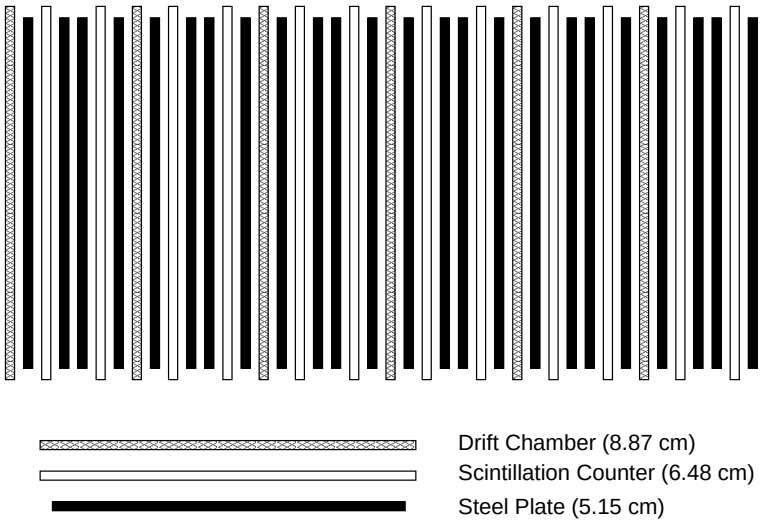

Figure 3.6: Layout of a CCFR target module. A scintillation counter is positioned after every two steel plates and a drift chamber is found after every four.

e^+e^- pairs. These electrons initiate short electromagnetic showers with a radiation length of 1.76 cm of iron ($\simeq 0.18$ counters).

The energy of the struck quark after the interaction is measured by sampling the flux of charged particles produced in the shower every 10 cm of iron in the scintillation counters. The active medium of the counters is mineral oil doped with scintillating fluors. A charged particle passing through the counter excites the primary fluors in the oil, which radiate ultraviolet light. The ultraviolet light is absorbed by secondary fluors, which in turn emit visible blue light. This light propagates through internal reflection to the edges of the counter where it is absorbed by half inch thick BBQ doped plastic bars. The bars re-emit green light and guide it to the end where phototubes are positioned. The total light output is approximately proportional to the total energy of the hadron shower and the fraction of the energy sampled in the calorimeter is approximately 3%. Figure 3.7 is a diagram of a scintillation counter.

The calibration of the calorimeter is described in detail in reference [51]. It involves a relative calibration using the energy deposition of muons, and an absolute calibration

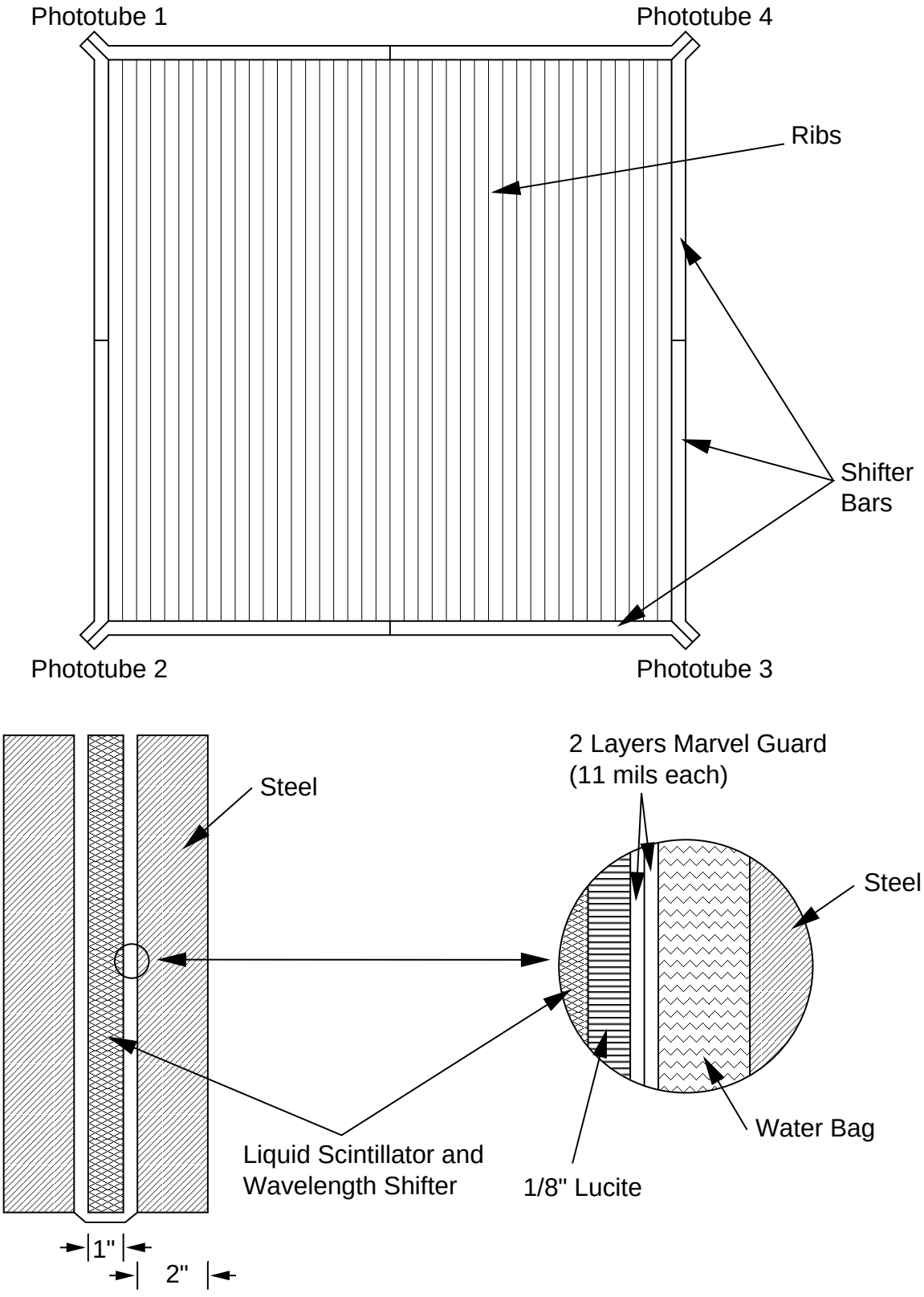

Figure 3.7: CCFR liquid scintillation counter.

determined from the measured energy depositions of momentum analyzed electrons and pions.

The ionization energy deposited in any material by a high energy charged particle is largely independent of particle type and energy, and is referred to as the minimum ionizing energy. We measure this energy using a muon's energy deposition profile. The muon energy loss is well understood: it consists of a pronounced peak due to ionization loss and a long tail due to less frequent catastrophic energy loss. The muon energy loss distribution as measured for one of the counters is plotted in Figure 3.8.

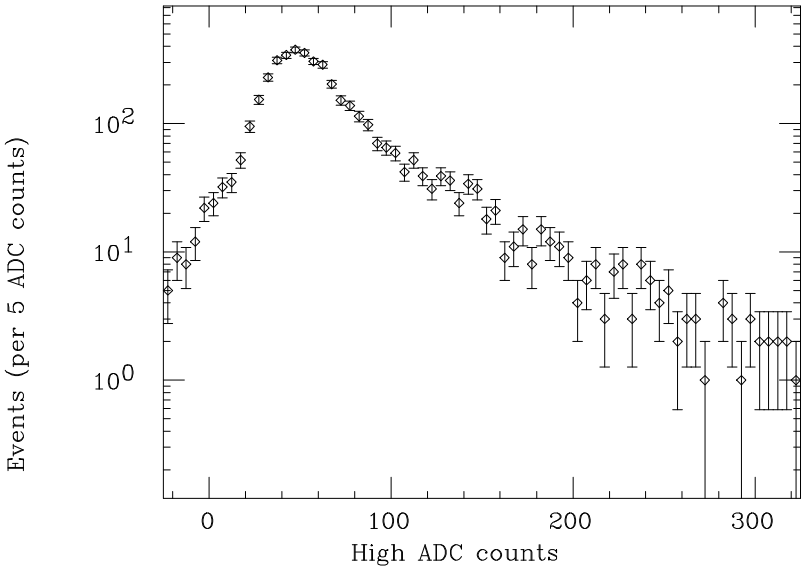

Figure 3.8: Muon energy loss distribution in a scintillation counter.

For this measurement, "straight-through" muons were used. These are muons produced by neutrino interactions in the berm upstream of the detector and are identified by the veto wall situated upstream of the calorimeter. The most probable energy loss per counter for these muons was calculated using a "truncated mean" of the distribution. The truncated mean was calculated in an iterative procedure of repeatedly calculating the mean of the distribution lying between 20% and 200% of the previous mean until the calculation converged. This truncation procedure minimizes the effect of the muon energy on the determination of

the mean. The truncated mean of the high channel distribution is taken to be one MIP in that counter and is denoted by the variable $\Delta E_i(x, y, t)$, indicating the position and time dependence of this quantity.

The distributions of the truncated mean for each counter were then binned according to either: (i) transverse coordinate or (ii) time period during the E770 run. The counter response differs over the active area of the counter due to attenuation of light within a counter and differences in its phototubes gains. Counter response is time dependent primarily because phototube gains tend to drift, and because there is slight degradation in the scintillator oil caused by ageing. The response with respect to position was typically about 20% higher at the edge of the fiducial volume (50 inches from the centre) and for the time dependence the average response fell by about 10% during the course of the E770 run [51]. All counter measurements were corrected to correspond to $t = 0$ and $(x, y) = (0, 0)$. A counter map, which shows the muon response relative to the centre of the counter is shown in Figure 3.9.

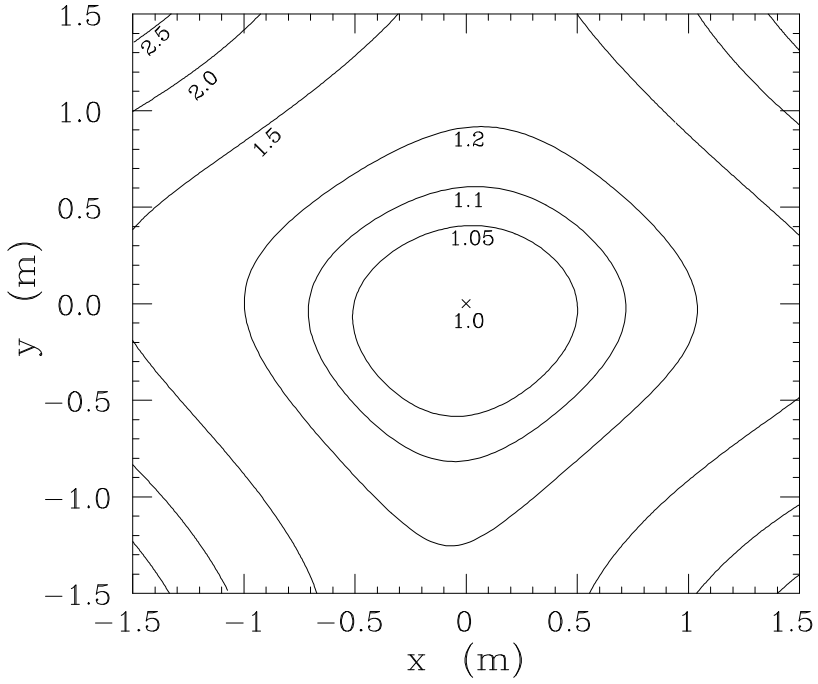

Figure 3.9: Relative muon response for counter number 37.

The calculation of the truncated mean establishes a relative calibration for the counters, *i.e.* an energy deposition anywhere in the counter can be converted to a measurement independent of the counter response by dividing the pulse height measured in ADC counts by the truncated mean:

$$\frac{\text{ADC pulse height}}{\text{truncated mean (x,y,t)}} = \text{energy deposit (in MIPs)} \tag{3.6}$$

where the truncated mean is for the appropriate time and position on the counter.

The absolute calibration of the detector involves establishing the relationship between the number of MIPs and the absolute energy of the incoming particles for each of the particles analyzed in the calorimeter. The target-calorimeter was absolutely calibrated twice with a test-beam of momentum-analyzed hadrons, muons and electrons with energies ranging from 15 to 450 GeV. These calibration runs took place before and after the experiment run. The total energy response of the calorimeter is obtained from runs where the test beam is centred on target. The calibration constants for the different types of particles are summarized in Table 3.1 [51]. Furthermore it was shown that the response of the calorimeter is linear to better than 1%, and that there is no difference in the response of identical target carts at the 1% level.

Type of signal	calibration
π	4.73 ± 0.02 MIPs/GeV
e	5.25 ± 0.10 MIPs/GeV
μ	6.33 ± 0.17 MIPs/GeV

Table 3.1: CCFR calorimeter calibration constants.

The test beam also provided measurements of the calorimeter resolution. For hadronic showers the resolution function is Poisson-like and is parameterized by the function:

$$f(x, \overline{x}) = \frac{\overline{x}^x e^{-\overline{x}}}{\Gamma(x+1)} \tag{3.7}$$

where $x = E/s$, s is a scaling parameter and $\overline{x}$ is the mean. Figure 3.10 shows the 25 and 200 GeV total energy distributions from the 1987 centred-beam calibration. By fitting

for s and $\overline{x}$ we obtain the standard deviation, $\sigma = s(\overline{x})^{1/2}$ and the energy of the incoming particles, $E = s\overline{x}$ which are used to determine the fractional sampling resolution σ/E. The resolution is characterized by the statistical fluctuations of the N particles sampled in the shower, therefore the resolution is dominated by the sampling fluctuations. The resolution is found to be:

$$\frac{\sigma}{E} = \frac{0.847 \pm 0.015}{\sqrt{E}} + \frac{(0.297 \pm 0.115)}{E} \tag{3.8}$$

where E is in GeV, and is plotted in Figure 3.11. The $1/E$ term is a noise term and is consistent with independently measured beam-related noise in the scintillation counters.

The calorimeter response to electromagnetic showers was calibrated using the electron component of the 25 and 50 GeV test beams. The electrons were identified by requiring R3, the ratio of the energy deposited in the three most upstream counters to the total observed energy to be greater than 0.96. With this requirement, it was estimated that the electron sample had about a 10% hadron contamination. The electromagnetic resolution was determined to be $\sigma_e/E = 0.60/\sqrt{E}$.

Further calibration studies were done in 1991 using cart 5 of the calorimeter during its temporary use as a "backing" calorimeter for FNAL E790, the Zeus calorimeter test beam program. The total useful event sample consisted of 36200 electrons and 85100 pions ranging with energies ranging from 7.8 to 91.1 GEV for electrons, and 19.8 to 108.8 for pions. The average response for the pion beam is $(E/p) = 4.7407 \pm 0.0021\ MIPs/GeV$, which is consistent with the value measured during the CCFR test beam calibrations. Of special interest to this analysis is the electromagnetic calibration of the detector. Unlike the CCFR calibration runs, the e^- identification using a transition radiation detector in the 1991 run produced an unbiased electron sample. Further cuts using R3 were made to enhance the purity of the sample. The resolution was fitted to the form $\Delta E/E = A/\sqrt{p} + B$. The fit yields $A = (46.1 \pm 1.0)\%$ and $B = (3.5 \pm 0.2)\%$, with a χ^2 of 3.6 per degree of freedom [53]. The stochastic term is considerably better than the $60\%/\sqrt{E}$ obtained during the

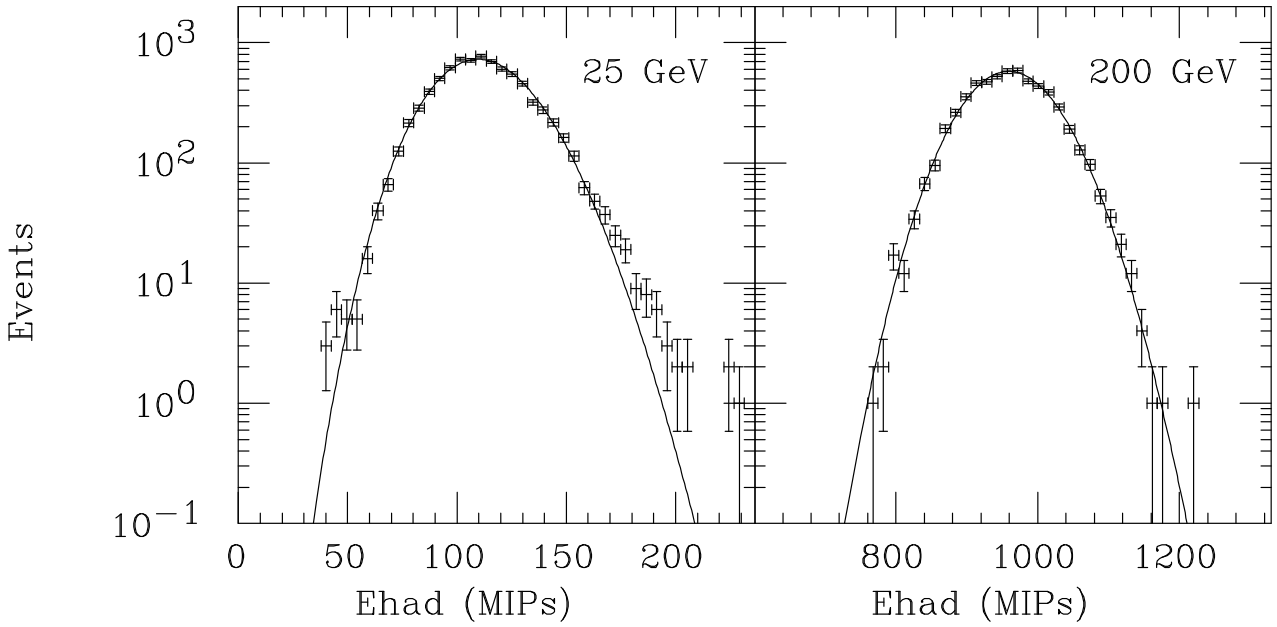

Figure 3.10: The total energy distributions of 25 and 200 GeV hadrons from the centred-beam calibration. The solid curves are the Poisson-like parameterizations of the distributions.

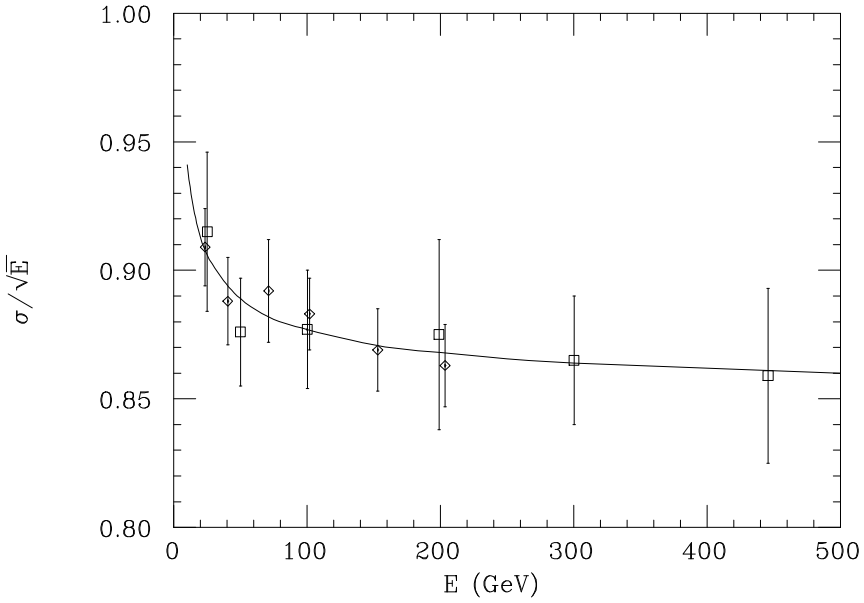

Figure 3.11: The hadron shower energy resolution of the CCFR calorimeter from 25 to 450 GeV centred-beam calibration. The curve is the parametrization given in Eq. 3.8.

CCFR calibrations runs. This can at least be partially attributed to the higher purity of the electron beam.

More important for this analysis is the electron-to-pion response, e/π, of the detector. Using data taken at 30, 70, and 90 GeV where both electron and pion data exists, one obtains $e/\pi = 1.062 \pm 0.003$, 1.041 ± 0.002, and 1.038 ± 0.003 respectively. An average of these results gives an e/π ratio of 1.05 which is considerably lower than the value of 1.11 obtained during the earlier calibration run. Since the purity of the electron test beam taken during the CCFR calibration run was poor, we decided to use $e/\pi = 1.05$ for this analysis.

The drift chambers, shown in figure 3.12, record the passage of charged particles through the detector. Each drift chamber station has an active area of 10×10 square feet and consists of an x and y plane. Each plane is divided into 24 cells, with each cell being 5 inches across and containing three wires used to shape the electric field within the cell. The central field wire is held at +350 volts, while the two sense wires spaced 2 mm from the field wire are held at +1750 volts. The cells are defined by parallel aluminum I-beams which are maintained at -4500 volts. Inside the front and back side of each cell there are 19 copper cathode strips, each of which is held at a particular voltage such that an uniform electric field of 690 volts/cm is created.

The chambers are filled with an equal mix of argon and ethane. A charged particle passing through a cell produces ionization electrons which drift towards the sense wires and are registered as an electrical pulse. The drift velocity of electrons in the drift chamber is 50 μm/ns, so that the total drift time to cross 2.5 in inside a cell is 1.3 μs. The time delay between the passage of the particle and the arrival of the pulse may be interpreted as the drift distance to the wire and allows for the determination of either the x or y coordinate of the charged particle, up to the ambiguity of determining which side of the wire the particle passed. Having two sense wires per cell resolves the ambiguity, as the sense wire closest to the particle receives the ionization. The intrinsic position resolution of the target drift

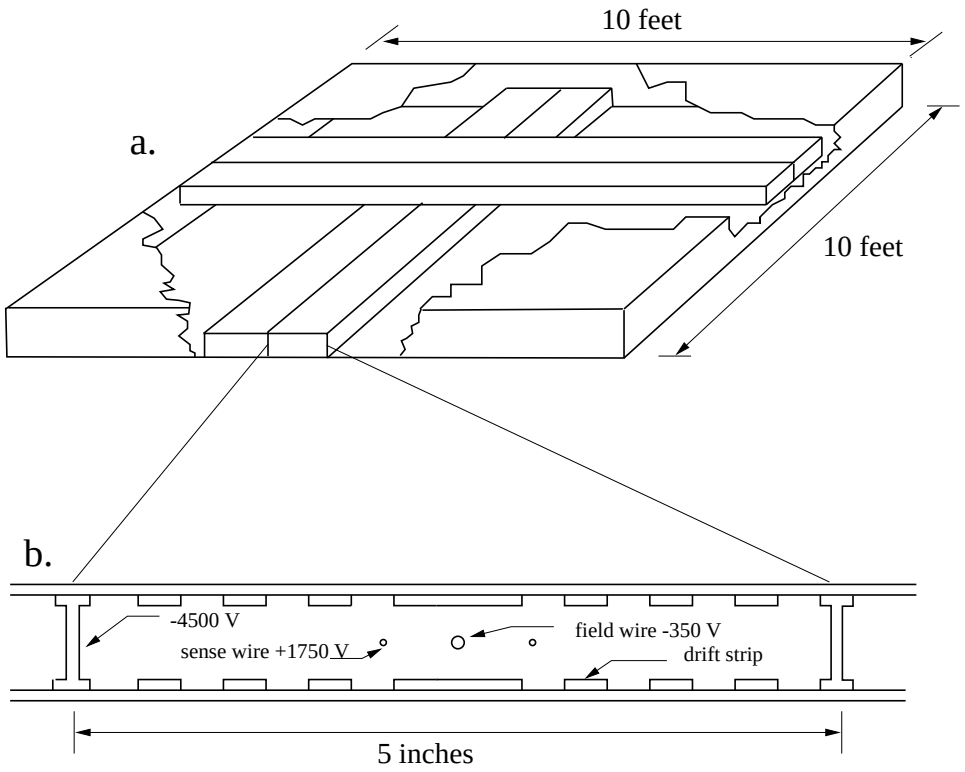

Figure 3.12: **(a)** CCFR target drift chamber station. There are two orthogonally oriented planes per station consisting of three-wire cells. **(b)** A three wire drift chamber cell.

chambers is 225 μm.

The drift chambers were used in this analysis only for the determination of the transverse coordinates of the interaction vertex.

3.3 The Muon Spectrometer

Although the main analysis of this thesis doesn't *directly* use muon momentum determination from the muon spectrometer, the muon momentum is used to determine the structure functions and incident flux.

The muon spectrometer consists of three large toroidal iron magnets instrumented with acrylic counters and 10 ft by 10 ft drift chambers. Each toroid cart is segmented into eight 8 inch thick cylinders, called washers, each 3.6 m in diameter with a 25 cm diameter hole for the magnetic coil. The magnetic field is generated by four copper coils of 12 turns each, which encircle the magnets at 90 deg intervals and returning through the hole at the centre of the cylinders. The coils carry a DC current of 1250 A which produces a magnetic field in the iron ranging from 1.9 T near the centre of the toroid to 1.55 T near the outer edge. The field was found to be azimuthal throughout the magnets except for a small radial component at the iron legs supporting the magnets. A muon traveling the length of the spectrometer receives an additional 2.4 GeV/c transverse momentum.

The momentum of each muon is determined using an iterative fitting procedure starting from an initial trial momentum estimated from a crude circular arc fit to the observed trajectory. For each trial momentum the predicted muon track is extrapolated through the magnets in 4 inch steps taking into account the energy loss due to ionization in each step. The predicted muon track is compared against the observed hits by forming the χ^2 function:

$$\chi^2(P_\mu) = \sum_{x,y} \sum_{i,j=1}^{N_{chambers}} (x_i^{measured} - x_i^{predicted}(P_\mu)) M_{ij}^{-1}(p_\mu)(x_j^{measured} - x_j^{predicted}(P_\mu)) \quad (3.9)$$

where x_i, x_j are the transverse measured or predicted track positions in the i^{th} and j^{th}

chambers respectively and $N_{chamber}$ is the number of chambers with hits from the muon. The matrix M_{ij} is the error matrix determined from the average multiple Coulomb scattering in the steel combined with the position measurement errors from the diagonal elements. Equation 3.9 is minimized by varying the momentum. This procedure continues until the momentum differs by less than 0.5% of the previous iteration.

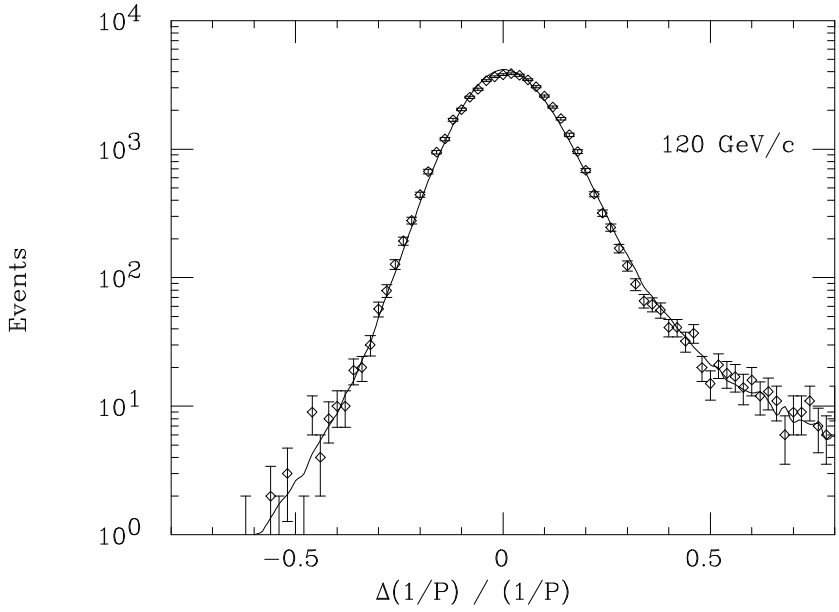

Figure 3.13: Experimental resolution function of the muon spectrometer for 120 GeV/c muons. The points are measurements of test beam muons, the solid line is an independent Monte Carlo prediction. The tail on the negative side is due to hard single scatters, and the tail on the positive side is due to catastrophic energy losses.

The calibration and resolution of the muon spectrometer was determined using test-beams of momentum analyzed muons. Figure 3.13 shows the experimental resolution function obtained from the test beam muons as compared to the Monte Carlo prediction. The central region is approximately Gaussian with a 10.1% r.m.s.; the small tails due to muons with large single scatters or catastrophic energy losses is also well modeled by the Monte Carlo. The muon absolute energy scale was calibrated using the test beam muons to a 1% accuracy.

3.4 Data Acquisition

Every charged particle passing through the detector will cause some form of response from each of the sub-systems affected: from the collected charge pulse on the drift chamber wires to the output pulse of the photomultiplier tubes on the scintillation counter. These "raw" signals need to be digitized in order to be able to store them to tape. The overall detector response is analyzed in an attempt to identify only the events of interest, while discarding events due to background or noise. Later, these signals – the pulse heights from scintillation counters, the drift chamber hits – will be converted to physical quantities like hadron and muon energy, vertex position and so on, and will enable us to do a physics analysis.

3.4.1 Event Triggers

The purpose of the trigger system is to identify in a very short period of time after a given event only events of interest and initiate storage to tape. As such, scintillator signals which can be processed quickly were used to generate the triggers. Each trigger rigorously defines an event signature which can be used to discriminate among different types of events. In order to minimize the cosmic ray contamination, the event triggers were gated to be active only during the three few ms bursts of neutrinos occurring during each cycle of the Tevatron. Gates were also set for the collection of pedestal, cosmic ray, and test beam events used for detector calibration and background subtraction.

In addition to the detector scintillators, two 17.5×4.5 feet acrylic scintillation counters are positioned immediately upstream of the first calorimeter cart to form a veto wall. The main purpose of the veto wall is to identify beam related backgrounds caused by charged particles produced by neutrino interactions in the berm. A one metre thick concrete wall is used to shield the veto wall from a flux of low energy hadrons and photons, and lead sheets are mounted between the two planes of the veto wall which are required to be in coincidence with each other in order to generate a veto.

Neutrino events were identified and classified using six separate triggers, with each recorded event firing one or more of the following triggers:

- **Trigger 1** (Charged Current): selects events in which a muon originates in the target and penetrates into the toroid. It requires at least two of the last four counters (counters 1 through 4) fire their s-bits, and both T2 (toroid gap 1) and T3 (gap 2) to measure at least a minimum ionizing signal. An alternate definition of the trigger does not require the muon to penetrate as far as T3, but instead demands two out of four s-bits in counters 9 thorough 12 together with a signal in T2 and two out of four s-bits in counters 1 through 4. Additionally we require no signal in the veto.

- **Trigger 2** (Neutral Current): selects events which deposit more than 8 GeV of energy shared between any eight adjacent scintillation counters coincident with twice minimum-ionizing energy deposited in two out of the four most downstream counters in the group of eight and no veto signal.

- **Trigger 3** (Penetrating Muon): requires 16 counters in the target (not necessarily consecutive) to fire their s-bits with no veto signal plus at least 4 GeV of energy deposited in any 8 consecutive counters (not necessarily the same ones that fired their s-bits).

- **Trigger 4** (Redundant Charged Current): used to study trigger 1 efficiency. It is similar to trigger 1 in as much that it selects events with a muon originating in the target and penetrating into the toroid but with somewhat stricter requirements. It requires at least 2 out of 4 s-bits in counters 5 through 8 and counters 13 through 16 in coincidence with no veto signal and it demands that at least two out of the four acrylic counters in the same quadrant for each of the eight half-toroid carts fire their s-bits (*i.e.* muon stays in the same quadrant throughout the toroid).

- **Trigger 5** (Test Beam): used for test beam running when muon and hadron beams are incident directly onto the detector.

- **Trigger 6** (Straight Through Muon): selects muons produced upstream of Lab E which traverse the whole detector. It requires at least one s-bit in each of the target carts and at at least 2 out of each set of 4 toroid counters within the same quadrant of each half-toroid plus veto (s-bits 81 and 82).

3.4.2 Data Readout

The receipt of a trigger initiates the collection and read-out of the detector response through the TDC (time-to-digital convertor) and FERA systems. The TDC system is composed of an s-bit branch and a drift chamber branch. The readout was coordinated by the data acquisition system which kept the 2 TDC and 1 FERA branches synchronized and wrote the data to tape. Each of the three systems is described in more detail below.

The pulse heights from the counters were integrated and digitized by a LeCroy 4300 FERA, a fast, buffered readout system with analog-to-digital converters with 11 bits of dynamic range and sensitivity of about 1/4 picocoulomb per count. The gate width of the ADC's is 240 ns, beginning 25 ns before the leading edge of the phototube signal, for an integration time of 215 ns. During this time the phototube signals charge the capacitors in the FERA's. The digitization is accomplished by measuring the time required to discharge the capacitor through a resistor. Digitizing the signals requires 8.5 μs and another 3.2 μs is needed to buffer the data because each pair of FERA modules generates 2×16 words which are transfered to the FERA memories at a rate of 100 ns/word. This leads to a total dead time of 11.7 μs for the FERA electronics.

The analog phototube outputs from each counter are fanned out and digitized by seven ADC channels of different sensitivity:

1. There are four low channels, one for each of the phototubes in the counter. A muon

passing through the centre of a counter will produce typically 2 ADC counts in each low channel.

2. The combination-low channel is the sum of the four low channels for each counter. A muon yields 8 ADC counts in this channel.

3. The high channel is the combination-low channel amplified by a factor of 10. The signal of a typical muon in this channel is 80 counts.

4. The super-low channel is the low channel attenuated by a factor of 10. The typical muon signal in this channel is 0.2 ADC counts.

In addition to the analog outputs there was also a logical output (NIM pulse). This output was created from the combination-low signal after it was amplified by a factor of a hundred and then passed through a discriminator. The discriminator threshold was set at 150 mV which is equivalent to 0.25 MIPs. The NIM output signals from the discriminators were converted to ECL and then input into TDCs which record the s-bit time relative to the trigger. The TDC system is described in more detail below. One counter's readout is shown in Figure 3.14.

Even in the absence of any particles the FERAs record a small signal of about 50 ADC counts called pedestal. This signal is due to random electronic noise originating from various electronic components (phototubes, fan-in/outs, cables, etc.) and during data taking it is superimposed with the real data pulses. This pedestal is measured by taking twenty fake events each cycle before the first ping when there was no input signal to the FERAs. This data is later subtracted in the software from the scintillator pulse heights in order to determine the real energy deposited by the particle in the scintillators.

The FERA system was read out using CAMAC connected to a PDP-11 computer. There were five CAMAC crates with ten 4300 FERAs, one 4301 FERA driver and five 4302

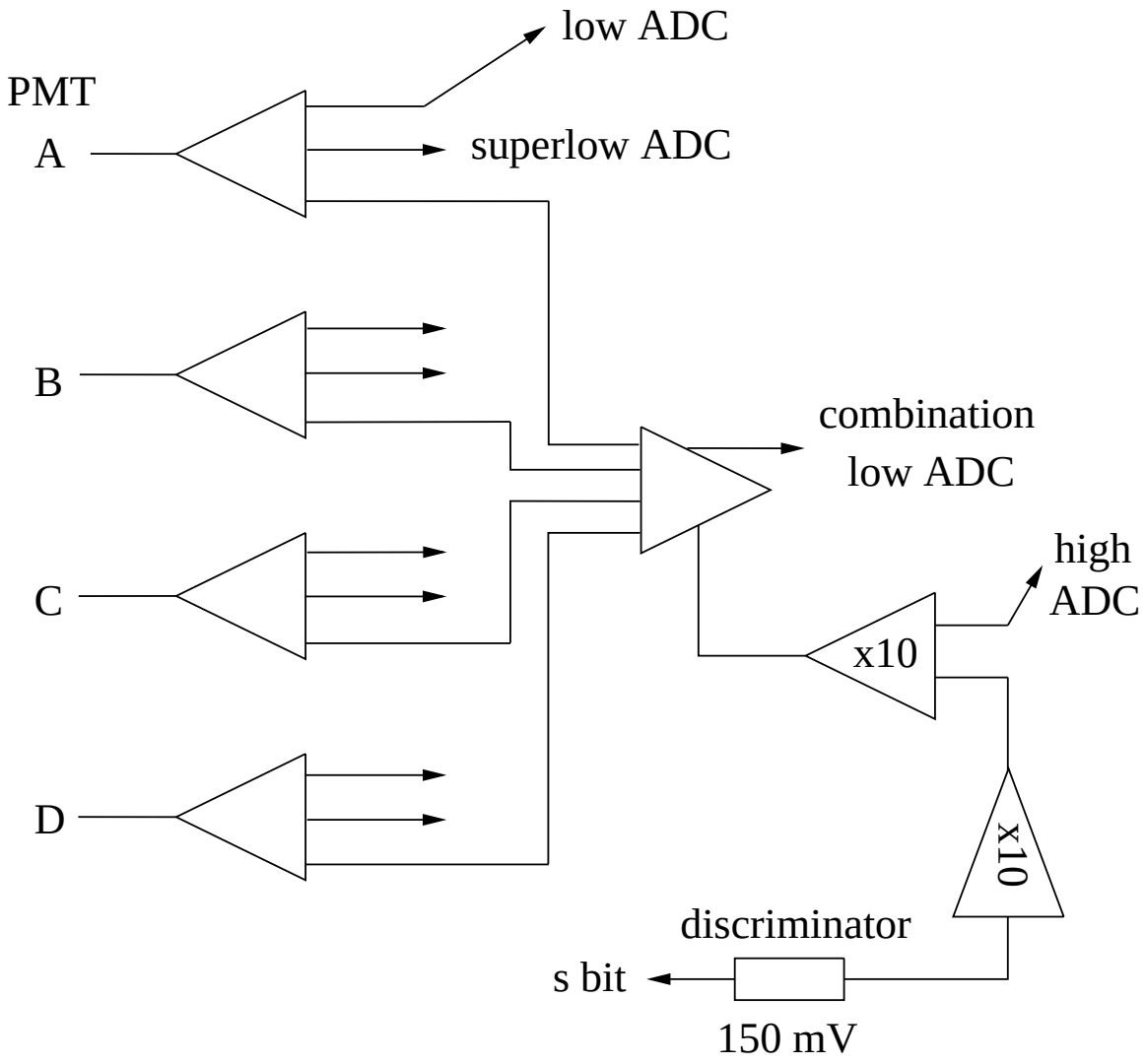

Figure 3.14: Readout electronics for a scintillation counter. Each counter is digitized by seven ADC channels. The threshold of the s-bit discriminator is set at one quarter minimum ionizing level.

memory units each. Fifteen microseconds after the ADC gate a clear pulse resets all the FERA bits to zero and the system was ready to write another event.

The signal from each sense wire in the drift chambers was digitized using the TDC's. A TDC board takes inputs from 16 channels on two 8-pair ribbon cable headers at the front of the board. The data is received as ECL differential signals, so the usual method is to transport the signals over twisted-pair wire. The input impedance is 100 Ω to match the characteristic impedance of the twisted pair lines. Each channel records the time history of the input signal (high/low) into two 16 bit circular buffers. The buffers are clocked 180 degrees out of phase with each other at 125 MHz providing a sampling resolution of the input signal of 4 ns for a total buffer length of 512 words. The total time window is thus $4\,\frac{ns}{\text{word}} \times 512\,\text{words} = 2\,\mu s$. The write clock is provided externally by a clock generator module and it is fanned out in equal time to all modules thus ensuring that all modules will record the event synchronously.

The clock module responds to a system trigger by stopping the clock at a high level. The stopping of the clock signals the TDC to transfer the data from the circular buffer into a global buffer memory which is shared by all 16 channels on one TDC card. Since the TDC stores only the last $2\,\mu s$ of data, one can change the position of this window with respect to the system trigger by adjusting the post-trigger delay in the clock generator/trigger module. The transfer into buffer memories takes place at 50 MHz, so the total transfer time is 512 words/50 MHz = 10.2 μs, during which time the TDC will not accept another trigger. During the transfer the leading and trailing edges of each pulse are identified by comparing consecutive time bins. The transition times from the 16 independent circular buffers, each corresponding to one input channel, are then formed into one word for each time interval. Each word in this buffer contains the transition time stamp (1-511) and one bit for each channel that was on.

The last word transferred into the buffer contains a special "complete" marker indicating

the last word of the event. Multiple event histories are allowed in the buffer memory and can be read out separately. The maximum word count per event can be set by switches to prevent overflowing of the buffer memories. There are two versions of the TDC board: "regular" and "deep-memory". A regular TDC has a buffer size of 256 words, while a deep-memory TDC has a buffer size of 1024 words.

The data readout of the TDC is initiated by a READ command sent by the data acquisition (DAQ). The readout continues until the number of words read out is equal to the number of words written in the main buffer. If at any time during the read out another trigger occurs, the readout is suspended and more data is transferred into the main buffer. The data being read out is transfered onto the backplane bus to the data link which then sends out the data to the DAQ. Typically, it will take several clock cycles for the data link to push out one cycle worth of data. To keep the TDC in sync, the data link will assert the hold line on the back plane while it processes one word. This will disable the read counter from incrementing.

Chapter 4

Neutrino Flux

The ν_μ and $\overline{\nu}_\mu$ were produced predominantly from two-body decays in the secondary beam of pions and kaons upstream of the detector. The integrated ν_μ and $\overline{\nu}_\mu$ fluxes reaching the detector were measured using the low hadron energy CC event samples, normalized to the total neutrino cross section [54, 55]. Approximately 86.4% of the event sample came from ν_μ interactions, 11.3% from $\overline{\nu}_\mu$, and 2.3% from ν_e or $\overline{\nu}_e$ interactions. The integrated ν_e flux measured directly in this thesis was also modeled using a Monte Carlo simulation of the neutrino beam-line for comparison.

4.1 Flux Model

We can understand the important features of the neutrino energy spectrum by looking at a simple idealized model of the secondary beam. We start by assuming that the all particles in the secondary beam propagate along the z-axis with a common momentum **p**. For the two body decays

$$K, \pi \rightarrow \mu + \nu, \tag{4.1}$$

the neutrino energy and angle with respect to the direction of the parent particle are constrained by the kinematic relation:

$$P = P_\nu + P_\mu \tag{4.2}$$

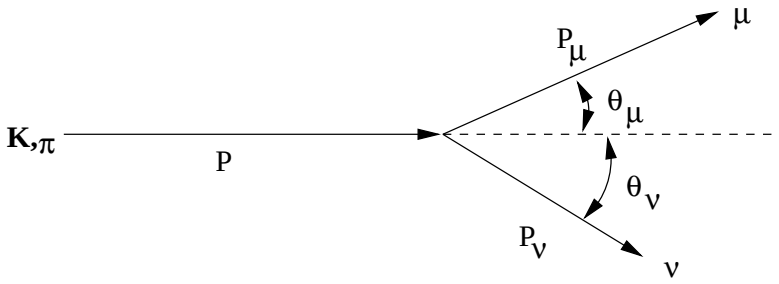

Figure 4.1: Definition of kinematical variables for a two body decay.

where $P = (m_{\pi,K}, \mathbf{p})$, $P_\nu(0, \mathbf{p}_\nu)$, and $P_\mu(m_\mu, \mathbf{p}_\mu)$ are the 4-momenta for the parent particle, the neutrino, and the muon defined as shown in Fig. 4.1. The energy of the outgoing neutrino in the LAB frame is:

$$E_\nu^{\mathrm{LAB}} = \frac{m_{K,\pi}^2 - m_\mu^2}{2E_{K,\pi}\left(1 - \beta\cos\theta_\nu\right)} \tag{4.3}$$

where $\gamma = \frac{E_{K,\pi}}{m_{K,\pi}}$ and $\beta = \sqrt{1 - \frac{1}{\gamma}}$. Let

$$E_\nu^{max} = E_{K,\pi}\left[1 - \left(\frac{m_\mu}{m_{K,\pi}}\right)^2\right]. \tag{4.4}$$

be the maximum energy the outgoing neutrino can have; then Eq. 4.3 can be written as:

$$E_\nu = \frac{E_\nu^{max}}{2\gamma^2(1 - \beta\cos\theta_\nu)} \tag{4.5}$$

For parent kaons, $E_\nu^{max} = 0.95E_K$, and for parent pions $E_\nu^{max} = 0.43E_\pi$ such that the neutrino flux would exhibit a dichromatic spectrum which corresponds to decays from either pions or kaons.

In the centre-of-mass reference system the parent mesons decay isotropically, so the number of neutrinos produced in a solid angle $d\Omega$ is:

$$dN_\nu = \frac{N_d B d\Omega_{cm}}{4\pi} \tag{4.6}$$

where N_d is the number of secondaries which decay and B is the two body branching ratio. The centre-of-mass and lab solid angles are related by:

$$d\Omega_{cm} = \frac{d(\cos\theta')}{d(\cos\theta)} d\Omega_{lab} \tag{4.7}$$

where θ' and θ are the centre of mass and lab decay angles respectively. The two angles are related by the Lorenz boost:

$$\cos\theta' = \frac{\cos\theta - \beta}{1 - \beta\cos\theta} \tag{4.8}$$

such that

$$\frac{d(\cos\theta')}{d(\cos\theta)} = \frac{1-\beta^2}{(1-\beta\cos\theta)^2} \tag{4.9}$$

If $m_{K,\pi} \ll E_{k,\pi}$ and $\sin\theta_\nu \simeq \theta_\nu$ then

$$1 - \beta\cos\theta \simeq 1 - \left(1 - \frac{1}{2\gamma^2}\right)\left(1 - \frac{\theta^2}{2}\right) \simeq \frac{1}{2}\left(\theta^2 + \frac{1}{\gamma^2}\right) \tag{4.10}$$

Substituting back in Eq. 4.3 we get

$$E_\nu = \frac{E_\nu^{max}}{1 + \gamma^2\theta_\nu^2} \tag{4.11}$$

If z is the distance from the decay point to the detector and R is the radius of impact at the detector, then

$$E_\nu = \frac{E_\nu^{max}}{1 + \frac{\gamma^2 R^2}{z^2}} \tag{4.12}$$

The number of neutrinos into some annular ring $(R, R + \Delta R)$ at the detector is then given by:

$$N_\nu(R, R+\Delta R) = \frac{2N_d B\gamma^2}{z^2}\int_R^{R+\Delta R} \frac{R\,dR}{\left(1 + \frac{\gamma^2 R^2}{z^2}\right)^2} \tag{4.13}$$

The number of neutrino interactions N_ν^{int} in a detector of density N_{TGT} nucleons per cm^2 due to the incident flux N_ν is:

$$N_\nu^{int} = N_\nu \sigma N_{TGT} \tag{4.14}$$

where σ is the neutrino interaction cross section which increases linearly with energy. If σ_ν/E_ν, the cross section slope, is constant then the number of interactions in the detector region between R and $R + \Delta R$ is:

$$N_\nu^{int}(R, R+\Delta R) = \frac{2N_d B\gamma^2 E_\nu^{max} N_{TGT}\frac{\sigma}{E_\nu}}{z^2}\int_R^{R+\Delta R} \frac{R\,dR}{\left(1 + \frac{\gamma^2 R^2}{z^2}\right)^3}. \tag{4.15}$$

The secondary particles decay over a distance of 320 m (see Figure 3.2) with a distribution falling exponentially with the lifetime:

$$\frac{dN_\nu}{dz} = \frac{e^{-\frac{z}{L_0}}}{L_0} \tag{4.16}$$

where $L_0 = \beta\gamma c\tau$, and τ is the meson's lifetime. If L_1 and L_2 are the distances from the beginning, end of the decay region to the detector respectively, then Eq. 4.15 becomes

$$N_\nu^{int}(R, R+\Delta R) = \frac{2N_s B\gamma^2 E_\nu^{max} N_{TGT}\left(\frac{\sigma}{E_\nu}\right)}{L_0} \int_{L_1}^{L_2} \frac{e^{-\frac{z-L_1}{L_0}}\, dz}{z^2} \int_R^{R+\Delta R} \frac{R\, dR}{\left(1+\frac{\gamma^2 R^2}{z^2}\right)^3} \tag{4.17}$$

where N_s is the number of secondaries.

In principle, to obtain the neutrino flux at the detector we would integrate Eq. 4.17 over the parent energy, angle, flight length, species of the secondary particle, branching ratio, etc. In practice we used a beam Monte Carlo to perform the integration using the following steps:

- Randomly pick a species of a secondary particle produced by the proton beam striking the beryllium target. Choose the energy, production angle and position according to the respective distributions. The modeling of the production position assumes a proton interaction length of 31 cm of beryllium oxide and a Gaussian transverse profile with r.m.s. widths of 0.35 mm (horizontal) and 0.65 mm (vertical). The secondary species that contributed the most to the neutrino flux were generated more frequently and the secondaries were weighted by their production cross section.

- Choose the z coordinate for the decay point randomly between the point of creation and the decay pipe with a distribution falling exponentially with the secondary's lifetime. Every secondary was forced to decay before the end of the decay pipe to efficiently use CPU time; each event was then weighted by the probability of decay. The secondary was traced through the magnet train and the event was discarded if the

particle hit a magnet or a collimator before the decay point. For a detailed description of the program used to trace the secondaries see Appendix B of reference [56].

- Choose the decay mode according to the branching ratio for the given secondary. Project the neutrino to the detector and increment the flux histograms for this neutrino species at this position and energy.

4.2 Production and Decay of Secondaries

The production of pions, kaons and other secondaries from the 800 GeV protons incident on the 1 interaction length beryllium oxide target was modeled, whenever possible, using experimentally measured cross sections for protons. The laboratory differential cross section is

$$\frac{d^2N}{dp\,d\Omega} = \frac{p^2}{E\sigma} \simeq \frac{p}{\sigma} I \qquad \text{(at high energies)} \tag{4.18}$$

where I is the invariant cross section, p is the laboratory momentum of the produced particle, E is the energy of the produced particle, and σ is the total inelastic cross section. To convert data taken at energies other than 800 GeV to our energy we used a scaling law proposed by Feynman [57] which assumes that the invariant cross section, I, can be represented as the product of a function of the transverse momentum of the secondary, p_T, and a function of the momentum fraction transferred to the secondary, $x_F = p/E_{\rm beam}$,

$$I = f(x_F)g(p_T) \tag{4.19}$$

The available production data is shown in Figure 4.2. It comes from measurements made by Atherton *et al.* [58] for π^+, π^-, K^+, and K^- from a 400 GeV proton beam incident on 4, 10, 30, and 50 cm Be targets, and by Skubic *et al.* [59] for K_S from a 300 GeV proton beam on a 15 cm Be target. Since the production angle of secondaries produced in E770 is restricted by the magnet aperture, $\theta_{apert} = 1.5$ mrad, only data below $p_T^{\rm max} = p\sin(\theta_{\rm apert}) = x_F E_{\rm beam}\sin(\theta_{\rm apert})$ was fitted to an empirical cross section parameterization from Malensek

sec.	ref.	E_0 (GeV)	L (cm)	A	B	D	M^2 (GeV^2)
π^+	[58]	400	50	3.598	177.2	27.00	0.7077
π^-	[58]	400	50	4.122	70.60	11.29	0.8932
K^+	[58]	400	10	2.7705	5.6924	20.844	1.1490
K^+	[58]	400	50	2.924	14.15	19.89	1.164
K^-	[58]	400	10	6.1068	5.6001	24.361	1.0422
K^-	[58]	400	50	6.107	12.33	17.78	1.098
K_S	[59]	300	15.3	3.6133	2.7970	10.671	0.76941

Table 4.1: Secondary production cross section fits to Malensek parametrization. The K_S fits were performed by C. Arroyo (CCFR); all other fits were by Malensek [60].

[60]:

$$\frac{d^2N}{dp\,d\Omega} = Bx_F \frac{(1-x_F)(1+5e^{-Dx_F})}{(1+p_T^2/M^2)^4} \frac{E_0}{E_{\text{beam}}} \tag{4.20}$$

where $d\Omega$ is an element of solid angle, E_0 is the energy at which the production cross section was measured, $E_{\text{beam}} = 800$ GeV is the proton energy for E770. The values for parameters A, B, D, and M^2 were obtained by fitting Equation 4.20 to the available data and are shown in Table 4.1.

Most of the production measurements were performed on targets of various lengths made of Be while the E770 target was BeO. Differences in target composition and thickness were accounted for by taking ratios of target production efficiencies. If we assume that the produced secondaries are reabsorbed in the target without producing additional particles, then the production efficiency is given by [60]

$$f(L) = \frac{e^{-L/\lambda(s)} - e^{-L/\lambda(p)}}{1 - \lambda(p)/\lambda(s)} \tag{4.21}$$

where L is the target length, $\lambda(s)$ is the absorption length for the produced secondaries, and $\lambda(p)$ is the absorption length for protons. The particle absorption lengths we assumed for Be and Be0 targets are listed in Table 4.2.

The beam Monte Carlo generates secondaries flat in Feynman x and p_T up to 3 GeV with a radial cutoff of $\theta = 10$ mrad (20 mrad for D mesons). The production weights were obtained from the Malensek parametrization given by Equation 4.20 using the transforma-

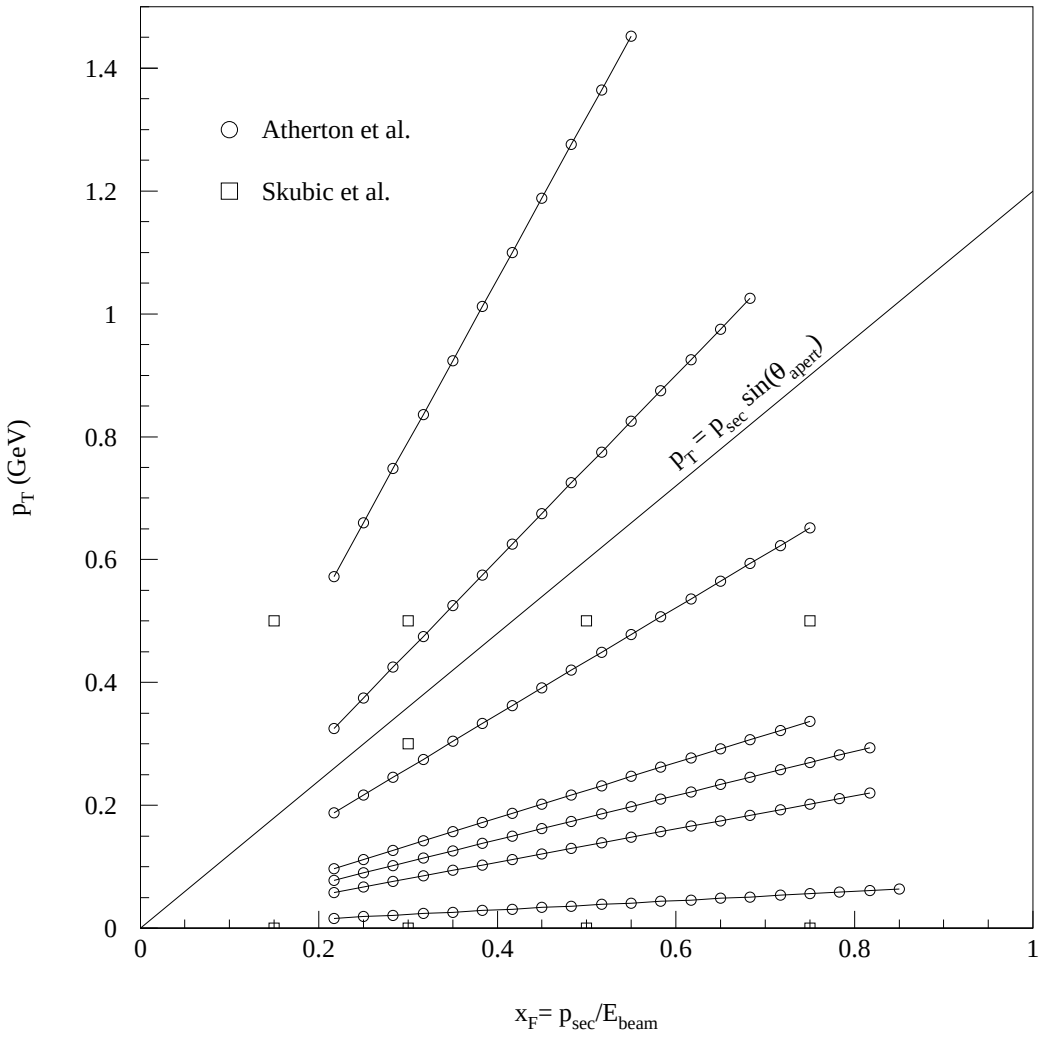

Figure 4.2: Available data for the parametrization of the secondary production cross section from Atherton *et al.* [58] for π^+, π^-, K^+, and K^- from a 400 GeV proton beam incident on 4, 10, 30, and 50 cm Be targets, and from Skubic *et al.* [59] for K_S from a 300 GeV proton beam on a 15 cm Be target. Only the points for which $p_T < x_F E_{\rm beam} \sin(\theta_{\rm aper})$ were used, where for E770, $E_{\rm beam} = 800$ GeV, and $\theta_{\rm aper} = 1.5$ mrad.

particle	λ for Be (cm)	λ for BeO (cm)
proton	43.26	30.99
π^+, π^-	57.83	41.76
K^+, K^-	65.24	46.80
K_S	65.24	46.80
Λ_0, Σ^-	43.26	30.99

Table 4.2: Assumed particle absorption lengths in Be and BeO targets.

tion

$$\frac{d^2N}{dx_F\, dp_T} = 2\pi \tan\theta \frac{E_{\rm beam}}{p_{\rm sec}} \frac{d^2N}{dp\, d\Omega} \tag{4.22}$$

The production cross section and flux modeling for each major species of secondaries produced in the target ($K^{\pm}$, K^0, π, charm mesons) are described in more detail in the following sub-sections. Small sources of neutrinos (contributing more than 0.1% of the ν_e's or ν_μ's in the final event sample) were also modeled and included in the final Monte Carlo flux.

4.2.1 Charged Kaons and Pions

The beam MC used charged K and π spectra from the Malensek fits to the Atherton *et al.* [58] production measurements from 400 GeV protons striking a 50 cm long beryllium target at the CERN SPS. Figure 4.3 shows the predicted event-weighted energy distribution of charged K and π secondaries contributing neutrinos which hit the detector. The QTB cuts off the low energy secondaries and only transmits particles with momenta above 100 GeV.

Kaons and pions decay predominantly via 2-body decays for which the kinematics are completely determined and simple to model.

$$\begin{array}{ll} K^{\pm} \rightarrow \pi^{\pm}\, \overset{(-)}{\nu}_{\mu} & \text{B.R. } 63.51\% \\ \pi^{\pm} \rightarrow \mu^{\pm}\, \overset{(-)}{\nu}_{\mu} & \text{B.R. } 99.99\% \end{array} \tag{4.23}$$

Charged kaons and pions also decay via 3-body decays,

$$\begin{array}{ll} K^{\pm} \rightarrow \pi^0 \mu^{\pm}\, \overset{(-)}{\nu}_{\mu} & \text{B.R. } 3.18\% \\ K^{\pm} \rightarrow \pi^0 e^{\pm}\, \overset{(-)}{\nu}_{e} & \text{B.R. } 4.82\% \end{array} \tag{4.24}$$

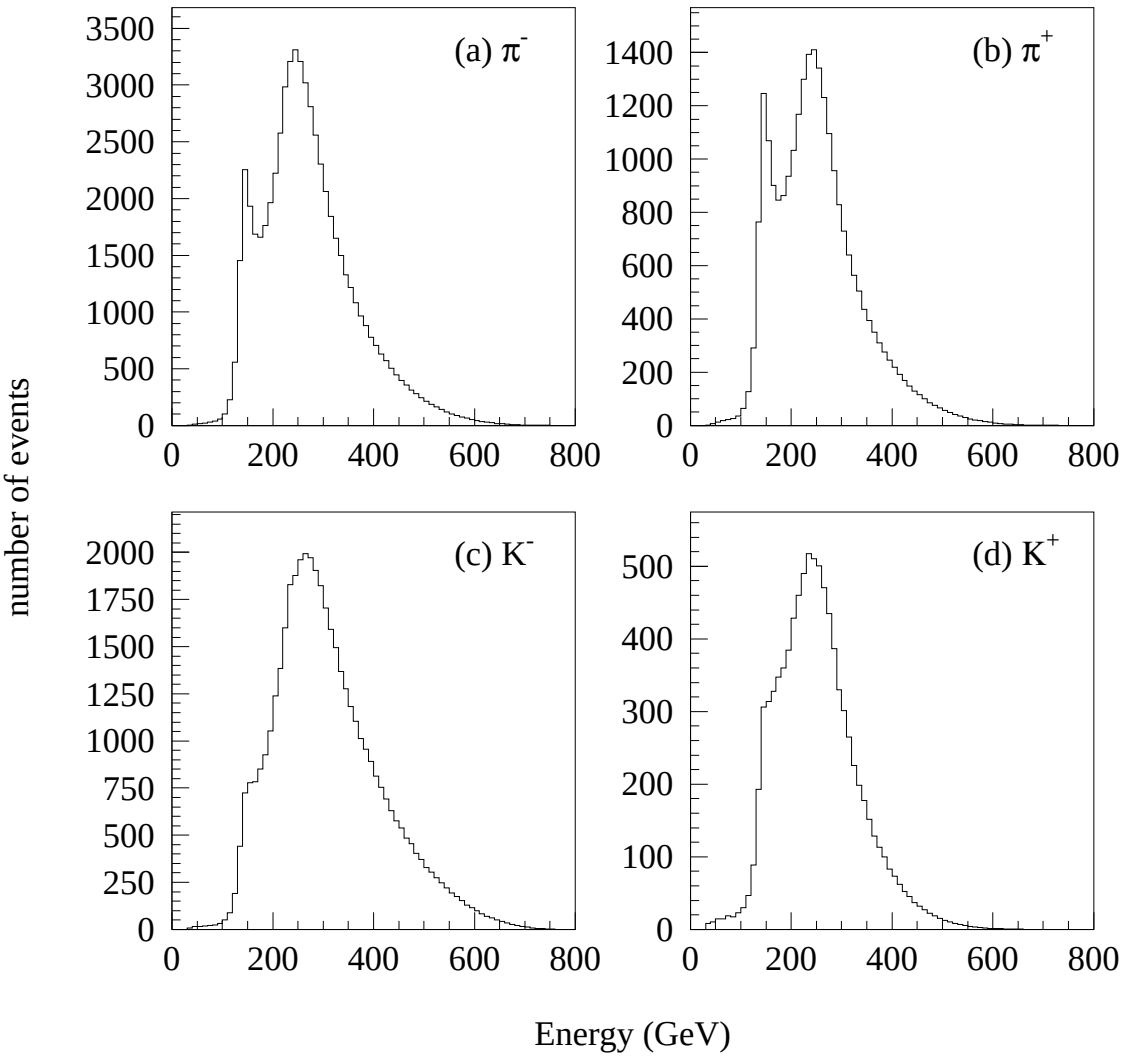

Figure 4.3: Event-weighted energy distribution of charged K and pi secondaries contributing neutrinos which hit the detector (Monte Carlo prediction).

decay mode	$\xi(0)$	λ_+
$K^+ \to \pi^0 \mu^+ \nu_\mu$	-0.35	0.033
$K^+ \to \pi^0 e^+ \nu_e$	0.	0.0286
$K^0 \to \pi^- \mu^+ \nu_\mu$	0.11	0.034
$K^0 \to \pi^- e^+ \nu_e$	0.	0.0300

Table 4.3: Matrix coefficients for 3-body K decays.

which we modeled using the following formula for Dalitz plot density and experimental decay matrix coefficients from a particle data group analysis [61]:

$$\rho(E_\pi, E_\nu) \propto f_+^2(t) \left[A + B\xi(t) + C\xi(t)^2 \right] \tag{4.25}$$

with

$$\begin{aligned} t &= m_K^2 + m_\pi^2 - 2 m_K m_\pi \\ f_+ &= 1 + \frac{\lambda_+ t}{m_\pi^2} \\ \xi(t) &= \frac{\xi(0)}{f_+} \\ A &= m_K(2E_\mu E_\nu - m_K E') + m_\mu^2(E'/4 - E_\nu) \\ B &= m_\mu^2(E_\nu - E'/2) \\ C &= \frac{E' m_\mu^2}{4} \\ E' &= \frac{m_K^2 + m_\pi^2 - m_\mu^2}{2 m_K} - E_\pi \end{aligned} \tag{4.26}$$

(for electron neutrinos replace E_μ by E_e, etc.). The 4 types of 3-body decays and the values of the experimentally determined matrix parameters $\xi(0)$ and λ_+ are given in table 4.3.

The events were generated using the following steps:

- Randomly generate the centre-of-mass energies of the decay products in the allowed phase space. The pion and muon (electron) energies were each generated uniformly within their kinematic limits. The choice was rejected if (i) the sum of the two energies was greater than the parent energy, (ii) the magnitude of any one of the momenta (p_π, p_μ or p_ν) was larger than the sum of the other two momenta.

- Use the acceptance-rejection method to keep or discard this choice of energies with probability given by the Dalitz plot density.
- Choose the z-position of the decay according to the lifetime.
- Randomly pick the neutrino direction in the kaon centre-of-mass frame such that the distribution of the cosine of the angle it makes with the z direction is flat.
- Boost the neutrino to the laboratory frame.

Figure 4.4 shows the predicted Monte Carlo energy distributions at the CCFR detector for muon neutrinos and antineutrino events from K's and π's.

4.2.2 Neutral Kaons

The modeling of neutral kaons is complicated by the phenomena of strangeness oscillations (analogous to neutrino oscillations): the quark eigenstates, K^0 and $\overline{K}^0$ which are produced by the strong interactions when protons strike the target change into each other by the mechanism shown in Figure 4.5. The objects which decay by weak interactions, K_S and K_L are not eigenstates of strangeness, and can be expressed in term of the quark eigenstates as:

$$\begin{aligned} |K_S\rangle &= \frac{1}{\sqrt{2}}\left(|K^0\rangle + |\overline{K}^0\rangle\right) \\ |K_L\rangle &= \frac{1}{\sqrt{2}}\left(|K^0\rangle - |\overline{K}^0\rangle\right) \end{aligned} \tag{4.27}$$

The CP-even K_S decays essentially 100% of the time vis $K_S \to \pi^+\pi^-$ and $K_S \to \pi^0\pi^0$, with a lifetime of 0.9×10^{-10} s. These modes are forbidden to the CP-odd K_L, which consequently has a much longer lifetime of 0.5×10^{-7} s. Here we have ignored CP-violation because the effect is very small. Some of the physical parameters of the neutral kaon system are given in Table 4.4.

The decay products in semi-leptonic decay modes are not CP eigenstates, so both K_S and K_L can decay to them with the branching ratio for K_S reduced by the ratio of the K_S

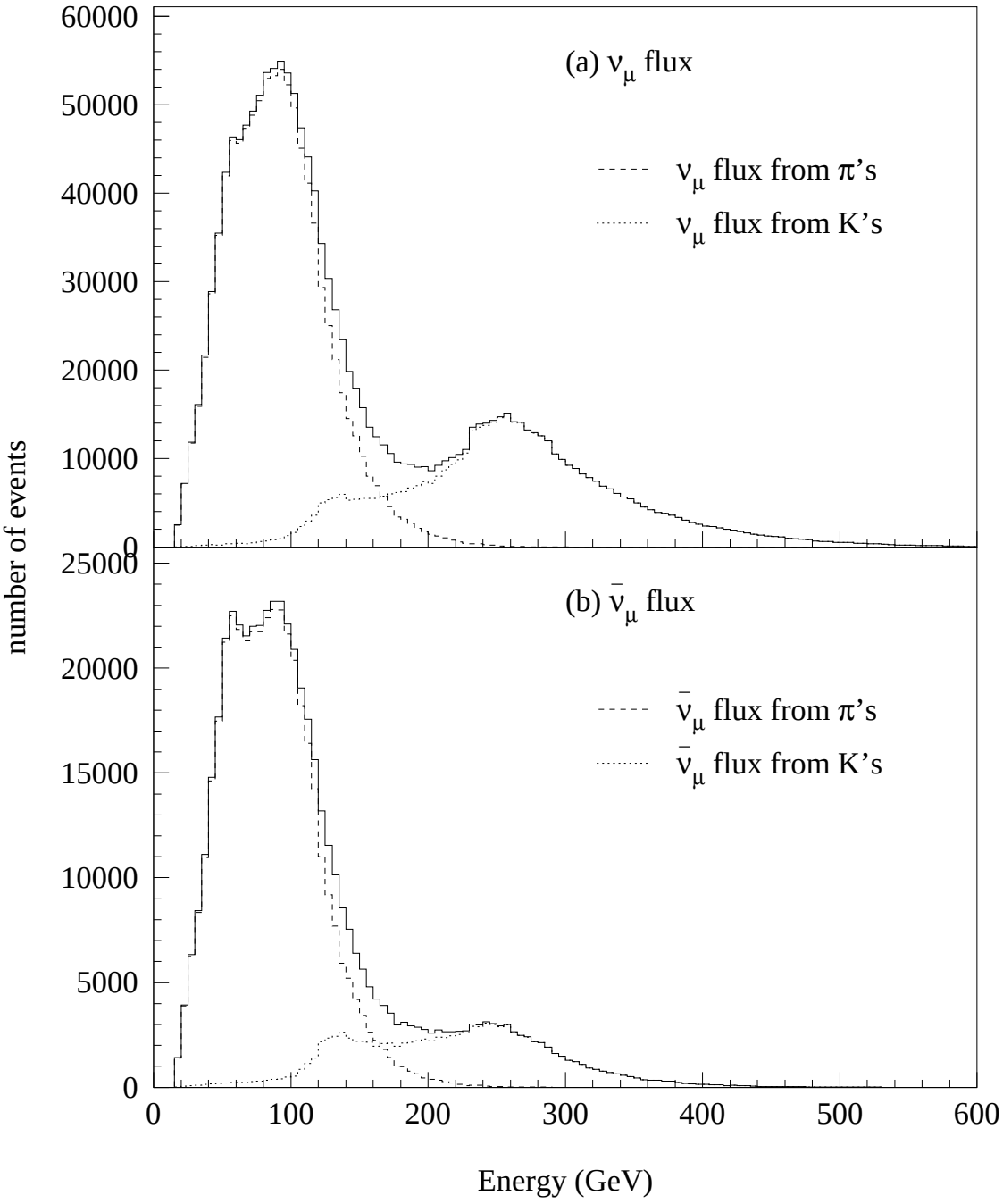

Figure 4.4: Energy distribution at the CCFR detector of events from (a) muon neutrinos, and (b) muon antineutrinos from K's and π's (Monte Carlo prediction).

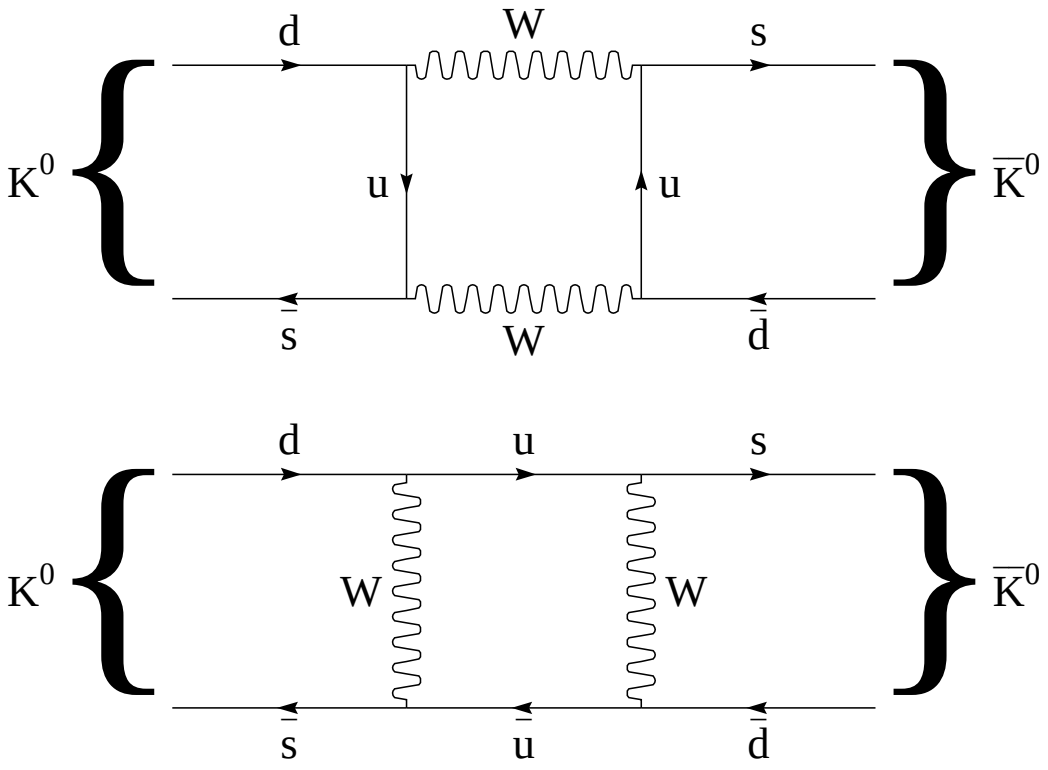

Figure 4.5: Feynman diagrams contributing to $K^0 \leftrightarrow \overline{K}^0$ mixing. Other contributions include diagrams with one or both u quarks replaced by the c or t quarks.

to K_L lifetimes. The quark eigenstates determine whether a neutrino or an antineutrino is produced in the decay:

$$K^0 \rightarrow \pi^- + \mu^+ + \nu_\mu \tag{4.28}$$

$$K^0 \rightarrow \pi^- + e^+ + \nu_e \tag{4.29}$$

$$\overline{K}^0 \rightarrow \pi^+ + \mu^- + \overline{\nu}_\mu \tag{4.30}$$

$$\overline{K}^0 \rightarrow \pi^+ + e - + \overline{\nu}_e \tag{4.31}$$

We can treat the time evolution of the kaon system the same way as for neutrino oscillations. If at time $t = 0$ we start with an initially pure $|K^0(\overline{K}^0)\rangle$ state, then at time t the system is in the same state with a probability given by:

$$\left|\langle K^0(\overline{K}^0)|\psi(t)\rangle\right|^2 = \frac{1}{4}\left[e^{-\frac{\Gamma_S t}{2}} + e^{-\frac{\Gamma_L t}{2}} \pm 2\cos(\Delta m t)e^{-\frac{(\Gamma_L+\Gamma_S)t}{2}}\right] \tag{4.32}$$

parameter	symbol	value
BR: $K_L \to \pi^{\pm}\mu^{\mp}\nu_\mu$	$(\mathrm{BR})_{\nu_\mu}$	(27.0 ± 0.4) %
BR: $K_L \to \pi^{\pm}e^{\mp}\nu_e$	$(\mathrm{BR})_{\nu_e}$	(38.7 ± 0.5) %
K_L decay rate	Γ_L	$1/15.50$ m
K_S decay rate	Γ_S	$1/0.02675$ m
neutral K mass	m_{K_0}	0.497671 GeV
$K_L - K_S$ mass diff.	Δm	$0.4774 \cdot \Gamma_S$

Table 4.4: Parameters of the neutral kaon system. Natural units are used with $\hbar = c = 1$.

The decay rates to neutrinos and antineutrinos are proportional to the probability of the system to be in a given quark eigenstate. The proportionality factor is the K_L decay rate, Γ_L, multiplied by the branching ratio of the K_L to the particular neutrino species:

$$\text{Decay rate to } \nu_{\mu,\mathrm{e}} = \Gamma_L \times (\mathrm{BR})_{\nu_{\mu,\mathrm{e}}} \left|\langle K^0|\psi(t)\rangle\right|^2 \tag{4.33}$$

$$\text{Decay rate to } \overline{\nu}_{\mu,\mathrm{e}} = \Gamma_L \times (\mathrm{BR})_{\nu_{\mu,\mathrm{e}}} \left|\langle \overline{K}^0|\psi(t)\rangle\right|^2 \tag{4.34}$$

The total probability of a K^0 ($\overline{K}^0$) produced in the target to decay to a particular neutrino before it reaches the beam dump is obtained by integrating the decay probability at a given time t over the time of flight, T:

$$\begin{aligned} \text{Decay rate to } \nu_{\mu,e} + \overline{\nu}_{\mu,e} &= (BR)_{\nu_{\mu,e}} \times \Gamma_L \int_0^T \left|\langle K^0|\psi(t)\rangle\right|^2 + \left|\langle \overline{K}^0|\psi(t)\rangle\right|^2 \, dt \\ &= (BR)_{\nu_{\mu,e}} \times \frac{1}{2}\left[1 - e^{-\Gamma_L T} + \frac{\Gamma_L}{\Gamma_S}\left(1 - e^{-\Gamma_S T}\right)\right] \end{aligned} \tag{4.35}$$

where

$$T = \frac{\Delta z m_{K^0}}{c E_K} \tag{4.36}$$

for a relativistic kaon produced in the target a distance Δz upstream of the beam dump.

The neutral kaon production spectrum was modeled using fits to measurements of K_S production near our energy range [59]. These measurements were made with a 300 GeV/c proton beam on Be and Pb targets. K_S production was measured at angles from .25 to 8.8 mrad and momenta from 65 to 250 GeV/c. The data most relevant to our experiment, taken with the Be target at 8.8 mrad, were used for the cross section fits to Malensek

parametrization (see Table 4.1). The K^0 and $\overline{K}^0$ production spectra were assumed to be equal to the measured K_S spectrum. The 3-body decay modes for neutrinos were modeled using the same method as that described for the charged kaons.

The production of neutrinos from neutral kaons proceeded as for the production from any other secondary (as itemized on page 70) except that (i) the probability of decay before the dump was given by Equation 4.35, and (ii) the z position of the decay and the choice whether the decay was a neutrino or an antineutrino were picked using the acceptance-rejection method with probabilities given by Equations 4.33 and 4.34.

4.2.3 Charm Production

The charm mesons, $D^{\pm}$ and D^0, and Λ_C contribute 2% of the electron neutrino flux at the detector. As an adequate approximation, only the following 3-body semi-leptonic decays were considered:

$$D^+ \rightarrow K^0 e^+ \nu_e \qquad \text{(B.R. 6.7\%)} \tag{4.37}$$

$$D^0 \rightarrow K^- e^+ \nu_e \qquad \text{(B.R. 3.48\%)} \tag{4.38}$$

$$\Lambda_C^+ \rightarrow \Lambda e^+ \nu_e \qquad \text{(B.R. 2.3\%)} \tag{4.39}$$

and were modeled in the same way as the 3-body decays of kaons, but with the kaon mass replaced by the D mass and the pion mass by the kaon mass.

The production spectra and the pp total cross section of $38 \pm 3 \pm 13$ μb for D^0 and $38 \pm 9 \pm 14$ μb for D^+ were measured by Kodama *et al.* using 800 GeV protons incident on emulsion [62]. The LEBC-MPS hydrogen bubble chamber experiment of Ammar *et al.* [63], also at 800 GeV, gives lower total cross sections of $22 \pm 4 \pm 6$ μb (D^0) and $26 \pm 8 \pm 7$ μb (D^+). Neither of these experiments measure Λ_C production, but the beam dump experiment of Duffy *et al.* [64] indicates that Λ_C's are responsible for as many ν_e's as D mesons. For this reason, we used the larger of the two measured D production spectra, the one from Kodama *et al.*.

Since the decay length for D's is shorter than the interaction length in aluminum, the protons that were not absorbed in the BeO target were allowed to interact and produce neutrinos in the beam dump following the decay pipe. This contributed approximately half of the total production of ν_e's from D's.

4.2.4 Other Small Sources of Neutrinos

The beamline Monte Carlo modeled all secondary species expected to contribute more than 0.1% of the ν_e or ν_μ flux in the final event sample, so in addition to the neutrino production from the secondaries listed above we also modeled μ decay, Λ decay and Σ^- decay.

Neutrinos from the decay of muons

$$\mu^+ \rightarrow e^+ + \nu_e + \overline{\nu}_\mu \tag{4.40}$$

account for 0.7% of the ν_e's at the detector. The muons were produced in the decays of pions and kaons. In the muon rest frame the ν_e distribution was modeled as [65]

$$\frac{d^2N}{dx\ d\cos\theta} \propto x^2(1-x)(1+\cos\theta) \tag{4.41}$$

where $x \equiv E_\nu/E_{\max}$, where $E_{\max} = (M_\mu^2 - M_e^2)/2M_\mu$ is the maximum energy the electron neutrino can have.

The decay of the Λ particle,

$$\Lambda \rightarrow p^+ + e^- + \overline{\nu}_e \tag{4.42}$$

generates about 0.4% of the electron neutrinos in the final sample. The production cross section was measured by Skubic *et al.* [59]. The formula for the differential decay density and experimental values for the decay matrix coefficients were obtained from Dworkin *et al.* [66].

The final, and smallest source of neutrinos modeled was the Σ^- decay,

$$\Sigma^- \rightarrow n + e^- + \overline{\nu}_e \tag{4.43}$$

which accounts for 0.2% of the ν_e's at the detector. The Σ^- production spectrum was parametrized as a fraction of π^- production by Cardello *et al.* [67]. As an adequate approximation, the decay was thrown flat in phase space.

4.3 Electron Neutrino Flux

Electron neutrinos are produced in the beam predominantly from decays of kaons: 80% of the ν_e's come from the decay of charged kaons, 16% from the decay of neutral kaons, and 2% each from the decay of charm particles and from the decay of π, μ, Λ and Σ^- particles as presented in the previous section. Since the main result of this thesis is a *direct* measurement of the electron neutrino flux which we compare to the beamline simulation in order to look for neutrino oscillations, it is very important to understand the Monte Carlo flux prediction and the systematic uncertainties associated with that prediction.

As stated, 80% of the ν_e flux comes from charged kaon decays. The QTB cuts off low energy charged secondaries (pions and kaons) and only transmits particles with momenta above 100 GeV with the maximum transmission at 300 GeV tune of the train. These high energy kaons decay into neutrinos that have a fairly narrow energy distribution that peaks around 260 GeV and is mainly above 200 GeV. Therefore, the beam flux normalization can be checked and corrected by comparing the observed ν_μ CC events for the Monte Carlo prediction for $E_\nu > 200$ GeV.

The beam Monte Carlo produces flux histograms for each of the four neutrino species, ν_μ, $\overline{\nu}_\mu$, ν_e, and $\overline{\nu}_e$, binned in energy and in x and y coordinates at the detector using the same energy and position binning as the data-based ν_μ and $\overline{\nu}_\mu$ flux files. The ν_μ and $\overline{\nu}_\mu$ contributions from K's and π's were binned in separate histograms and the separate pion and kaon-induced components of the neutrino and antineutrino flux files were normalized separately to the data-based muon neutrino files. The normalization was chosen such that the fraction of ν_μ flux above 200 GeV, which is produced predominantly from the decay

	ν_μ	$\overline{\nu}_\mu$
π	0.951	1.056
K	1.000	1.136

Table 4.5: Normalization factors for the π and K contributions to the ν_μ and $\overline{\nu}_\mu$ flux files from the beam Monte Carlo. The normalization factor for the K-induced ν_μ flux files was set to 1.

of kaons agreed with the data based files. The normalization factors required in the beam Monte Carlo is listed in Table 4.5. The overall normalization of Monte Carlo relative to the data is made by forcing the number of ν_μ CC events above 200 GeV in the Monte Carlo to be equal to the corresponding events in the data. Figure 4.6 shows comparisons between the beam Monte Carlo and data-based ν_μ and $\overline{\nu}_\mu$ flux files after applying the normalization factors.

The good agreement between the beamline Monte Carlo and the measured ν_μ flux files in the K-induced part of the ν_μ spectrum above 200 GeV constrains the uncertainty in the ν_e flux from charged kaons. We assign a 2.5% uncertainty in the ν_e flux due to the modeling of the ν_e spectra. An additional systematic uncertainty comes from a 1.2% uncertainty in the branching ratio for K decays into ν_e's ($4.82 \pm 0.06\%$) and estimated contribution of approximately 1% in the normalization of the π/K ratio which corresponds to a typical variation in the normalization for reasonable changes in the normalization procedure.

The ν_e's produced by the decay of neutral kaons are not constrained by the ν_μ data and unfortunately we have to rely on outside measurements. Consequently the largest single uncertainty in the number of ν_e's from neutral kaons comes from the relative normalization of the neutral K spectrum to the charge secondary spectrum. The Skubic *et al.* experiment [59] quotes an overall normalization uncertainty of 10%. Atherton *et al.*'s [58] normalization uncertainty is not clearly stated. Further uncertainties come from the parametrization of the Skubic *et al.* data and from conversion to the E770 conditions of 800 GeV protons and a 30.5 cm Be target. We estimate that the largest source of uncertainty in the ν_e

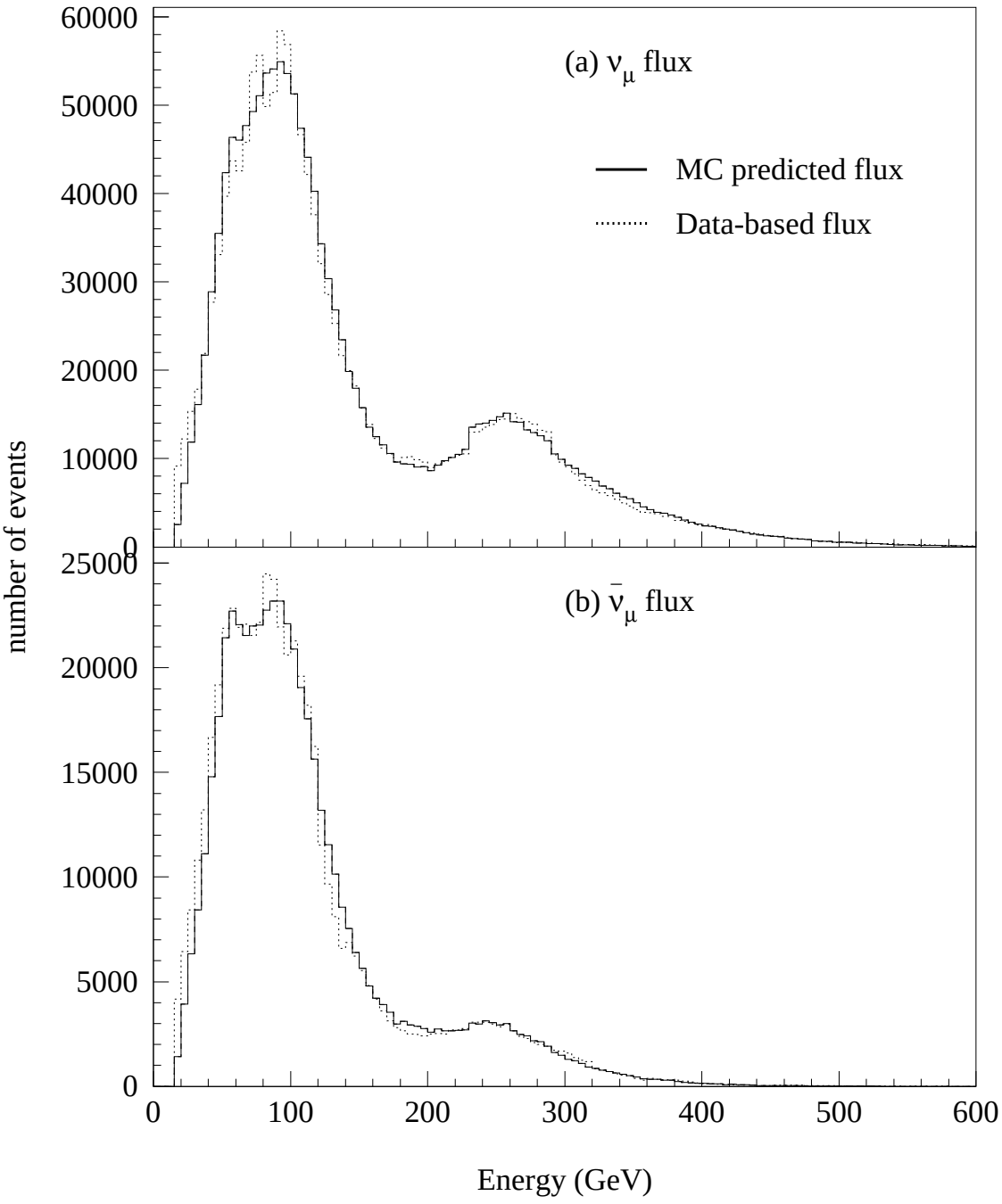

Figure 4.6: Comparison of beam Monte Carlo and data-based flux files for (a) muon neutrinos, and (b) muon antineutrinos. The overall normalization of Monte Carlo relative to data is made by forcing the number of ν_μ CC events above 200 GeV in the Monte Carlo to be equal to corresponding events in the data.

production from neutral kaons probably comes from the normalization uncertainties in these two experiments which we assign to be twice the normalization uncertainty of Skubic *et al.* , giving a 20% fractional uncertainty.

The 2% component of ν_e's from charm production was assigned a 50% fractional uncertainty due to poor knowledge of the production rates and spectra. The ν_e's from the remainder of the small sources were better modeled and were assigned a 10% fractional uncertainty. Table 4.6 itemizes the contributions to the ν_e uncertainty from the various species of secondary particles producing neutrinos at the detector, totaling a 4.1% uncertainty in ν_e production.

The number of events predicted by the Monte Carlo beamline simulation for ν_μ, $\overline{\nu}_\mu$, ν_e, and $\overline{\nu}_e$ as a function of neutrino energy is listed in Table 4.7.

4.4 Muon Neutrino Flux

Since a muon neutrino beam cannot be monitored *directly* the flux of neutrinos had to be determined *indirectly* from a measurement of the number of interactions in the detector itself. The extraction is done using the subset of the data sample with low hadron energy. This is called the fixed-ν method because it counts the number of neutrino interactions with $\nu = E_{had}$ less than a fixed-ν cut, ν_0. This method yields the *relative* flux, the ratio of fluxes at different energies, $\Phi(E_i)/\Phi(E_j)$, and the ratio of fluxes of the different species, $\Phi^\nu/\Phi^{\overline{\nu}}$. The *absolute* flux is found by normalizing the measured total neutrino cross section for $E_\nu < 230$ GeV to the world average, $\sigma^{\nu N} = (0.676 \pm 0.014) \times 10^{-38}$ cm^2 E_ν.

The general formula of the differential charged current neutrino-nucleon cross section is:

$$\frac{d\sigma}{d\nu} = \frac{G^2 M}{\pi} \int dx\, F_2 \left[1 - \frac{\nu}{E} \left(1 \mp \frac{\int x F_3}{\int F_2} \right) + \frac{\nu^2}{2E^2} \left(1 \mp \frac{\int x F_3}{\int F_2} + \int \mathcal{R} \right) \right] \tag{4.44}$$

where the $+(-)$ is for neutrino (antineutrino) interactions. The integrals are over all x and

$$\mathcal{R} = \frac{\nu + 2Mx}{\nu(1+R)} - \frac{Mx}{\nu} - 1 \tag{4.45}$$

species	**% of total**	**fract. uncert.**	**uncert. contrib**
charged K's	80%	3%	2.4%
neutral K's	16%	20%	3.2%
charm (D)	2%	50%	1.0%
π,μ,Λ,Σ^-	2%	10%	0.2%
TOTAL	100%		4.1%

Table 4.6: Hadron species producing the $\nu_e(\overline{\nu}_e)$ flux and their contributions to the electron neutrino flux uncertainty.

E_ν (GeV)	ν_μ events	$\overline{\nu}_\mu$ events	ν_e events	$\overline{\nu}_e$ events
15- 30	387083	159456	1837	1193
30- 40	407835	247162	2198	1791
40- 50	632695	383544	3950	2791
50- 60	857109	463208	6369	3417
60- 70	922474	468615	7461	4385
70- 80	1146633	453635	9928	4556
80- 90	1056141	527724	11517	6011
90-100	1232275	442214	12294	5366
100-120	1828506	791184	26553	10487
120-140	1071222	373849	27565	9928
140-160	708132	244743	26808	9145
160-180	440118	142543	26630	7528
180-200	438312	103548	23891	7031
200-230	633510	168160	28689	5351
230-260	906345	184154	17438	3100
260-290	868357	142599	10365	1692
290-320	510598	91938	6029	792
320-360	396645	32442	3717	536
360-400	267702	19913	1650	186
400-450	212254	9106	963	84
450-500	124888	3562	268	17
500-550	68490	1144	68	3
550-600	21222	499	9	0

Table 4.7: Number of ν_μ, $\overline{\nu}_\mu$, ν_e, $\overline{\nu}_e$ events as a function of neutrino energy (Monte Carlo prediction).

is the longitudinal structure function. F_2 and xF_3 are the structure functions of neutrino interactions defined in terms of the quark and antiquark distributions:

$$F_2 = xq(x) + x\overline{q}(x) \tag{4.46}$$

$$xF_3 = xq(x) - x\overline{q}(x) \tag{4.47}$$

The leading term of the differential cross section with respect to ν is a constant, $\left(\frac{G^2M}{\pi}\int F_2\right)$, and ν dependent corrections are of the order $\left(\frac{\nu_0}{E}\right)$ and $\left(\frac{\nu_0^2}{E^2}\right)$. These corrections are small and depend only on the ratio $\frac{\int xF_3}{\int F_2}$ and $\int \mathcal{R}$. The number of events with $\nu < \nu_0$ is found by multiplying the differential cross section by the flux and integrating up to ν_0

$$\begin{aligned} N(E,\nu<\nu_0) &= \Phi(E)\frac{G^2M}{\pi}\int F_2\nu_0\left[1-\frac{\nu_0}{2E}\left(1\mp\frac{\int xF_3}{\int F_2}\right)\right. \\ &\left. +\frac{\nu_0^2}{6E^2}\left(1\mp\frac{\int xF_3}{\int F_2}+\int\mathcal{R}\right)\right] \end{aligned} \tag{4.48}$$

Thus by simply counting the number of events with $E_{had} < \nu_0$ and applying corrections of order $\left(\frac{\nu_0}{E}\right)$ and $\left(\frac{\nu_0}{E}\right)^2$, one can determine the flux to an overall normalization.

The term that depends on $\mathcal{R}$ is determined by using measurements of the longitudinal structure function made by charged-lepton scattering experiments [68]. The ratio $\frac{\int xF_3}{\int F_2}$ can be calculated by fitting the low E_{had} data to a quadratic polynomial of the form

$$\frac{dN}{d\nu} = A + B\left(\frac{\nu}{E}\right) + C\left(\frac{\nu^2}{2E^2}\right) \tag{4.49}$$

where

$$A(E) = \frac{G^2M}{\pi}\int F_2\Phi(E) \tag{4.50}$$

$$B(E) = -\frac{G^2M}{\pi}\int F_2\left(1-\frac{\int xF_3}{\int F_2}\right)\Phi(E) \tag{4.51}$$

$$C(E) = B + A\int\mathcal{R} \tag{4.52}$$

The ratio of coefficients is independent of the neutrino flux $\Phi(E)$ and determines the ratio of the integrated structure functions

$$\frac{B}{A} = -\left(1\mp\frac{\int xF_3}{\int F_2}\right) \tag{4.53}$$

The ratio $\frac{B(E)}{A(E)}$ is approximately constant with energy because although the structure functions depend on $Q^2 = 2Mx\nu$ by imposing a fixed ν cut means that the same Q^2 range is used at all energies. The average of $\frac{B}{A}$ from fits in all energy bins determines $\left\langle \frac{B}{A} \right\rangle$ to high statistical precision. The relative flux is then obtained by integrating the observed event distribution, $\frac{dN}{d\nu}$, to the fixed ν cutoff:

$$\Phi(E) \propto \int_0^{\nu_0} d\nu \, \frac{dN}{d\nu} \left[1 - \frac{\nu}{E} \left\langle \frac{B}{A} \right\rangle + \frac{\nu^2}{2E^2} \left(\left\langle \frac{B}{A} \right\rangle + \int \mathcal{R} \right) \right]^{-1} \tag{4.54}$$

The fixed-ν cut is chosen at $\nu_0 = 20$ GeV to ensure sufficient statistics in the higher energy bins while minimizing the systematic correlations with the data sample. The other cuts imposed are $E_\mu > 15$ GeV and $\theta_\mu < 0.150$. A total of 407,000 neutrino and 140,000 antineutrino events are used for the flux extraction.

The values of $\frac{B}{A}$ are shown in Figure 4.7. The values show no energy dependence and the averages are $\left\langle \frac{B}{A} \right\rangle_\nu = -0.50 \pm 0.04$ and $\left\langle \frac{B}{A} \right\rangle_{\overline{\nu}} = -1.70 \pm 0.05$. The relative neutrino and antineutrino fluxes are shown in Figure 4.8.

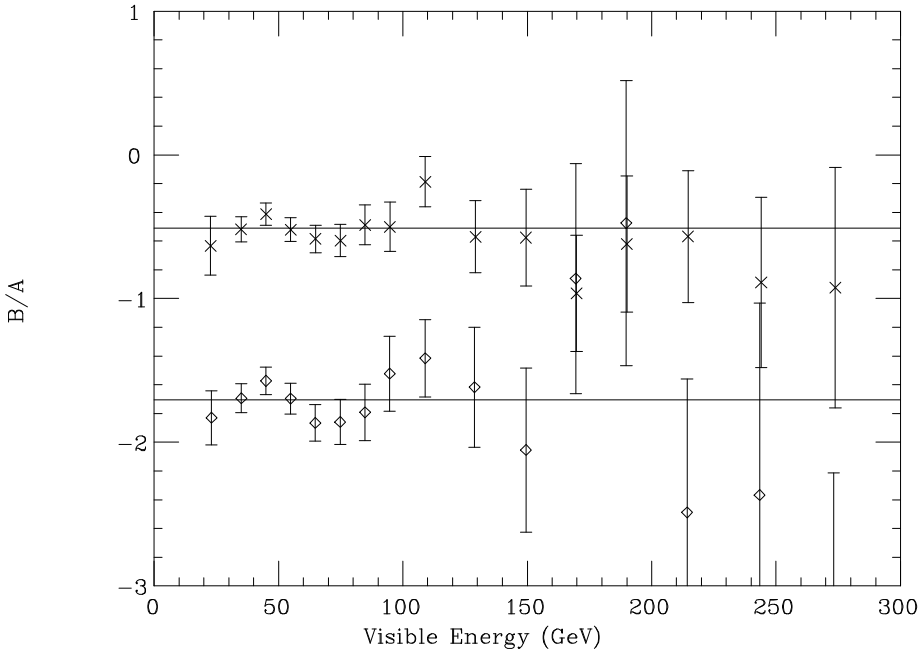

Figure 4.7: Energy dependence of $B/A = -(1 \mp \int xF_3/F_2)$ for events with $\nu < 20$ GeV, for neutrinos (x) and antineutrinos (diamonds). A and B are the coefficients of the $(\nu_0/E)^0$ and $(\nu_0/E)^1$ terms of $dN/d\nu$.

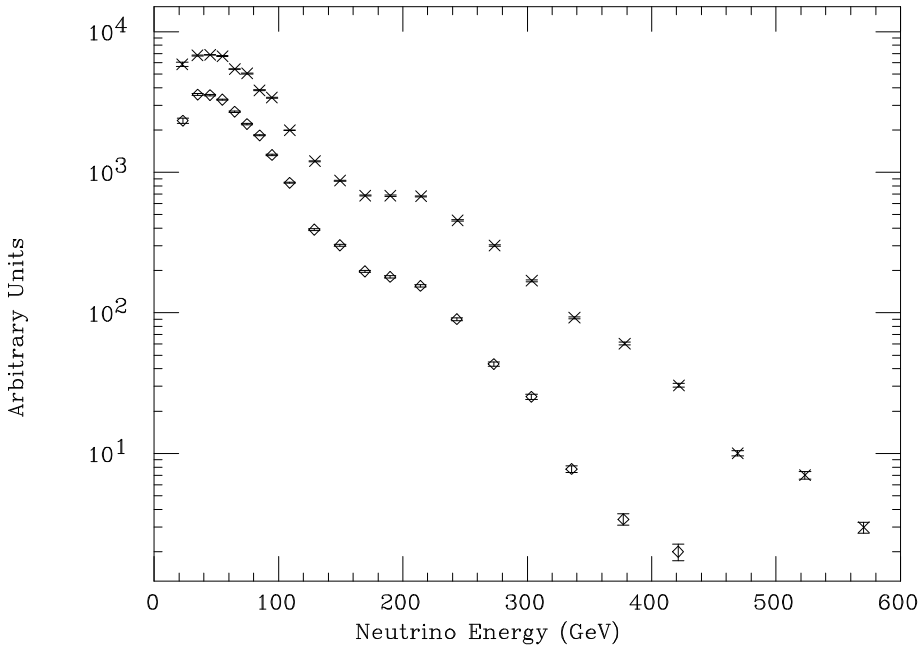

Figure 4.8: The relative neutrino (x) and antineutrino (diamonds) fluxes determined using the fixed-ν method.

Chapter 5

Data Analysis

The neutrino interactions observed in the detector can be divided into three categories depending on the type of the incoming neutrino and on the type of interaction:

1. $\nu_\mu N \rightarrow \mu^- X$ (ν_μ charged current (CC) events).

2. $\nu_{\mu,e} N \rightarrow \nu_{\mu,e} X$ ($\nu_{\mu,e}$ neutral current (NC) events).

3. $\nu_e N \rightarrow eX$ (ν_e CC events).

All three types of neutrino interactions initiate a cascade of hadrons that is registered by the drift chambers and scintillation counters. The ν_μ CC events are characterized by the presence of a muon produced in the final state which penetrates well beyond the end of the hadron shower, depositing energy characteristic of a minimum ionizing particle (mip) [51] in a large number of consecutive scintillation counters. Conversely, the electron produced in a ν_e CC event deposits energy in a few counters immediately downstream of the interaction vertex which changes the energy deposition profile of the shower. The electromagnetic shower is typically much shorter than the hadron shower and the two cannot be separated for an individual ν_e CC event. In this analysis four experimental quantities are calculated for each event: the length, the transverse vertex position, the visible energy and the shower energy deposition profile. The three sections of this chapter describe (i) the algorithm used to obtain the event parameters, (ii) the analysis cuts, and (iii) the analysis procedure.

5.1 Event Reconstruction

The characteristics of the neutrino interaction are determined by the energy deposited in the scintillation counters. The downstream end of the region is defined to be the first counter of two consecutive counters with more than a 1/4 MIP, and the upstream end, ISTRT, as the last counter followed by three counters with less than 1/4 MIP. Of the approximately one million events used in this analysis, 29.3% were found to have more than one interaction region, mostly due to inefficiencies in the scintillation counters. For these events we combine the longest interaction region with the adjacent regions if the number of counters separating the two regions is smaller than the length of the shorter region. If at the end of the combination process we still have multiple regions, the region with the highest energy deposition is assumed to be the neutrino interaction region, which was required only for 0.7% of the events.

We define PLACE to be ideally the counter immediately downstream from the event's real interaction vertex. The "44 PLACE" is the more upstream of two consecutive counters with more than 4 MIPs immediately downstream of ISTRT. The end of the shower, SHEND, is assigned to be the last counter upstream of three consecutive counters each with less than 4 MIPs and immediately downstream of PLACE.

The visible energy deposited in the calorimeter, E_{vis}, is calculated by summing the energy deposited in the scintillation counters from ISTRT to five counters downstream of SHEND. This definition was chosen to include the energy deposited upstream of the interaction vertex by both particles traveling backwards in the detector and particles penetrating past SHEND, while minimizing the difference between CC and NC showers due to the muon track present in CC interactions.

Studies based on Lund/GEANT [69] generated showers indicate that at high energies the 44 PLACE is not a good estimator of the "true" interaction place. Figure 5.1 shows the

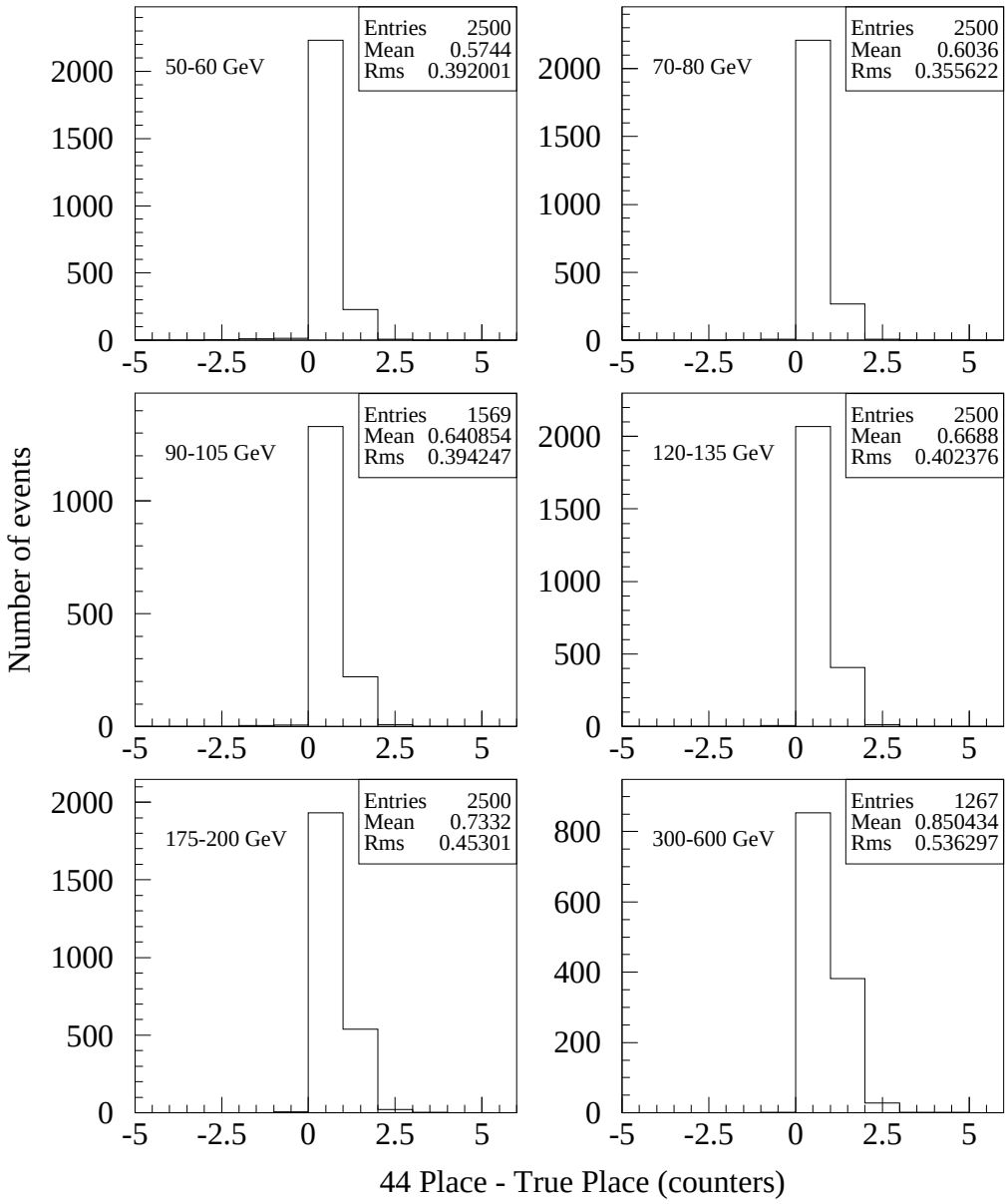

Figure 5.1: The difference between the 44 PLACE and the true place for a neutrino neutral current interaction. At high energies the 44 PLACE is not a good estimator of the true interaction place (based on Monte Carlo studies).

difference between the generated place and the 44 PLACE in six of the E_{vis} bins studied. Similar to the 44 PLACE, we define the NN PLACE to be the more upstream of two consecutive counters with more than N MIPs, where N varied from 4 to 25 MIPs. For each energy bin N was chosen such that the rms of the difference between the generated place and the NN PLACE was the smallest. Table 5.1 shows the value of N for each energy bin.

Energy (GeV)	N (MIP's)
20 - 30	4
50 - 60	6
70 - 80	7
90 - 105	8
120 - 135	10
150 - 175	12
175 - 200	11
200 - 250	14
250 - 300	16
300 - 600	19

Table 5.1: The value of the minimum energy in MIP's which when deposited in each of two consecutive scintillation counters signals the start of a neutrino interaction. The more upstream of the two counters is assigned to be the interaction place (based on Monte Carlo studies).

We parameterize the value of N as a function of energy by fitting to the values in Table 5.1 a function of the form:

$$N = -1.0679 + 0.9660 \times \sqrt{E_{vis}} \tag{5.1}$$

where, as before, N is in MIP's and E_{vis}, the energy deposited in calorimeter from ISTRT to SHEND-5, is in GeV. Figure 5.2 shows the difference between estimated and true interaction place for six energy bins.

The Monte Carlo prediction for the NN PLACE was checked by studying the shift from the 44 PLACE to the NN PLACE in the Monte Carlo and comparing it against that in the data. This value depends on quantities measured directly in both the data and the MC. The good agreement between the data and the MC shown in Figure 5.3 gives us confidence

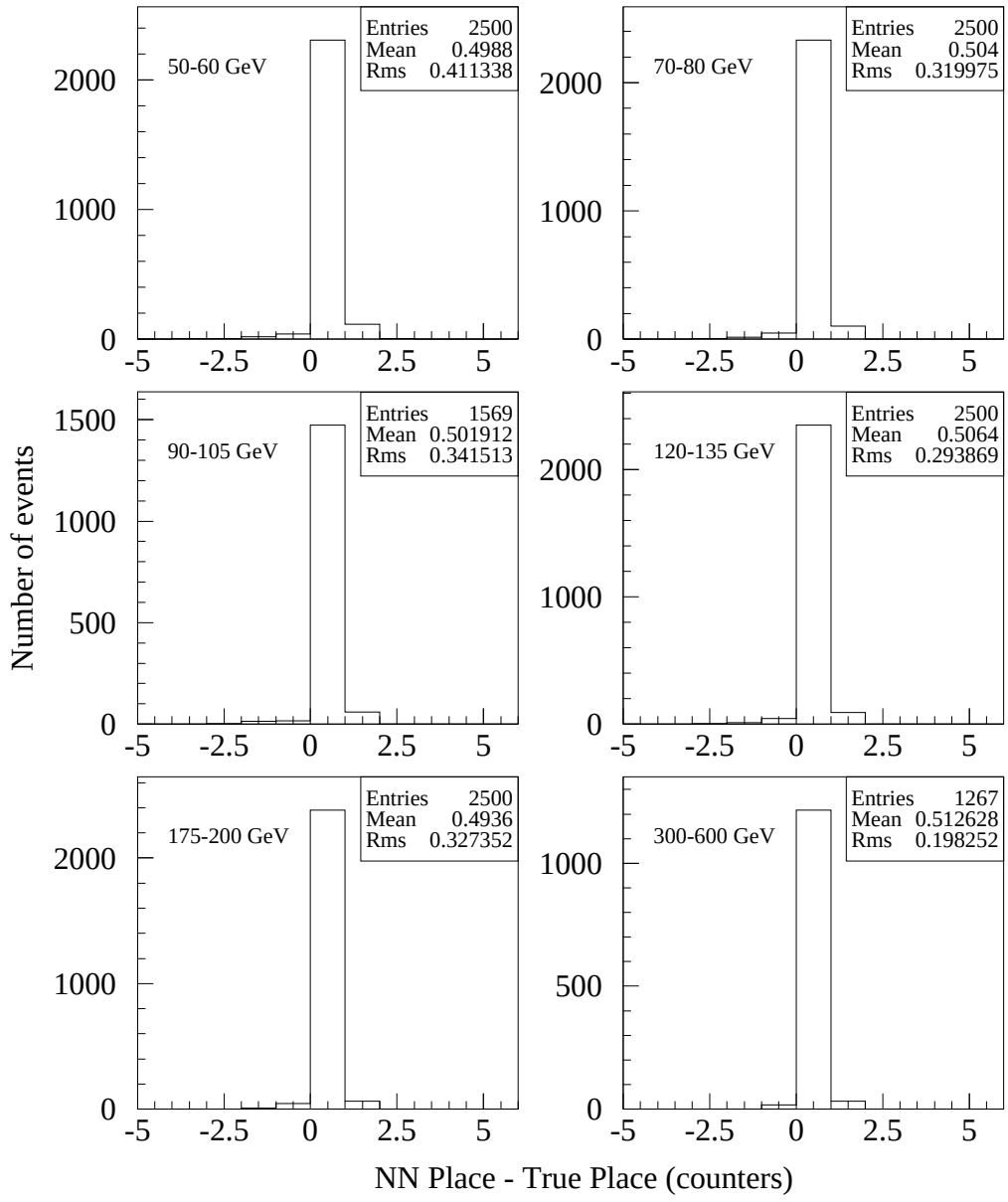

Figure 5.2: The difference between the NN PLACE and the true place for a neutrino neutral current interaction. At high energies the NN PLACE is a much better estimator of the true interaction place than the 44 PLACE (based on Monte Carlo studies).

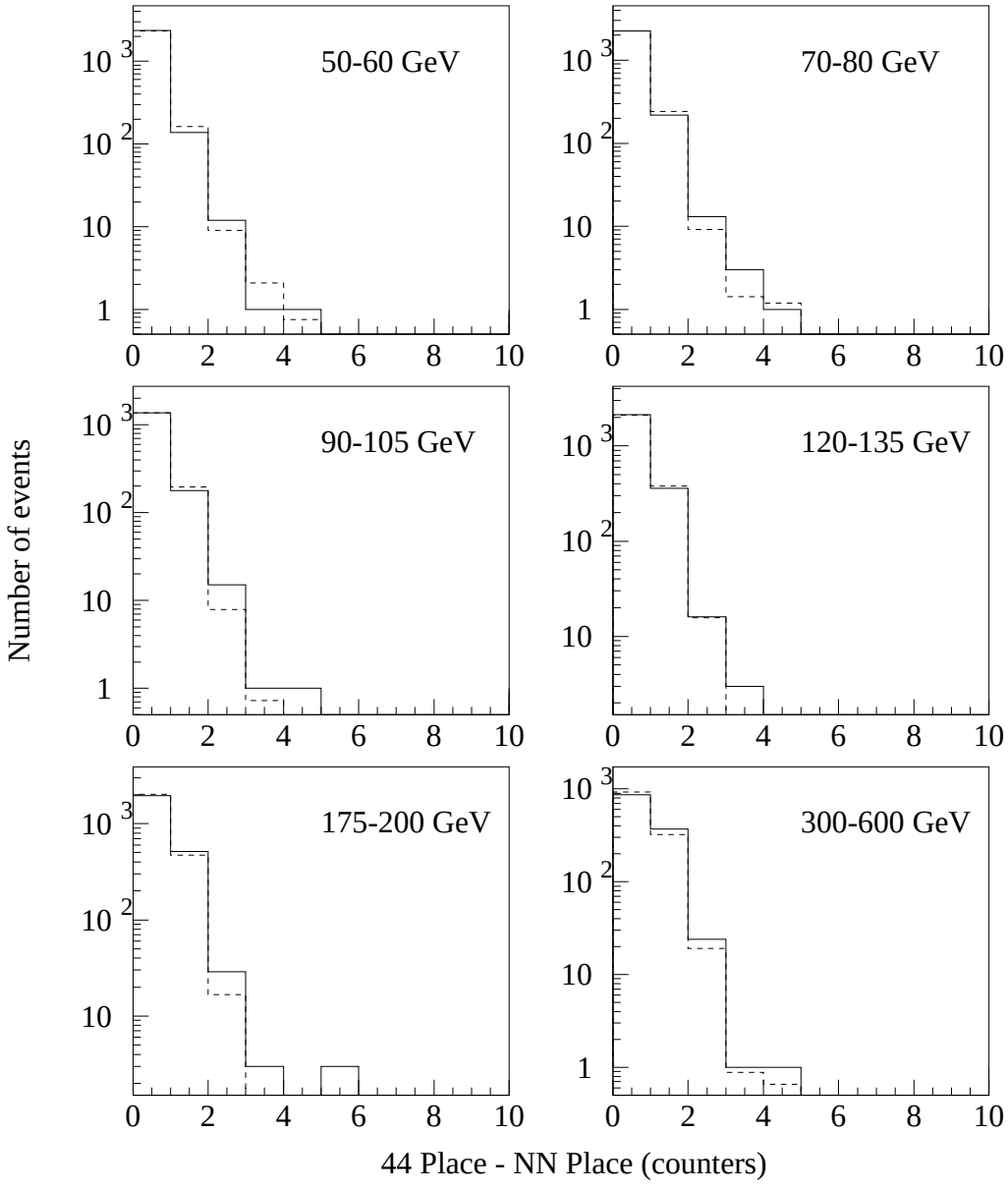

Figure 5.3: Data and Monte Carlo difference between the NN PLACE and the 44 PLACE for neutrino neutral current interactions. The solid (dashed) histogram is the MC (data).

that the measured shift in the MC between the NN PLACE and the true interaction place is a good indicator of the shift in the data.

The event length, L, is defined to be the number of scintillation counters spanned by the event:

$$\mathrm{L} = \mathrm{PLACE} - \mathrm{CEXIT} + 1 \tag{5.2}$$

where PLACE is the experimental determination of the interaction vertex, calculated as the NN PLACE, and CEXIT is the most downstream counter with energy deposited from the products of the neutrino interaction. CEXIT is the first counter downstream of SHEND followed by three consecutive counters with less than 1/4 MIP. CEXIT occurs at the end of the hadron shower for neutral current events, but is determined by the muon track for most charged current events.

The mean position of the hits in the drift chamber immediately downstream of PLACE determines the transverse vertex position.

The shower energy deposition profile is characterized by the ratio of the sum of the energy deposited in the first three scintillation counters to the total visible energy. The electron produced in a ν_e CC interaction deposits all of its energy in counters immediately downstream of the interaction place. A ν_e CC interaction will appear in the calorimeter just like a ν_μ NC interaction, but, on average, it will deposit more energy in the first scintillation counters than a ν_μ NC interaction with the same visible energy. Accordingly, we define

$$\eta_3 = 1 - \frac{E_1 + E_2 + E_3}{E_{vis}} \tag{5.3}$$

where E_i is the energy deposited in the i^{th} scintillation counter downstream of the interaction place (see Fig. 5.4), to describe the energy deposition profile of the shower produced by the neutrino interaction.

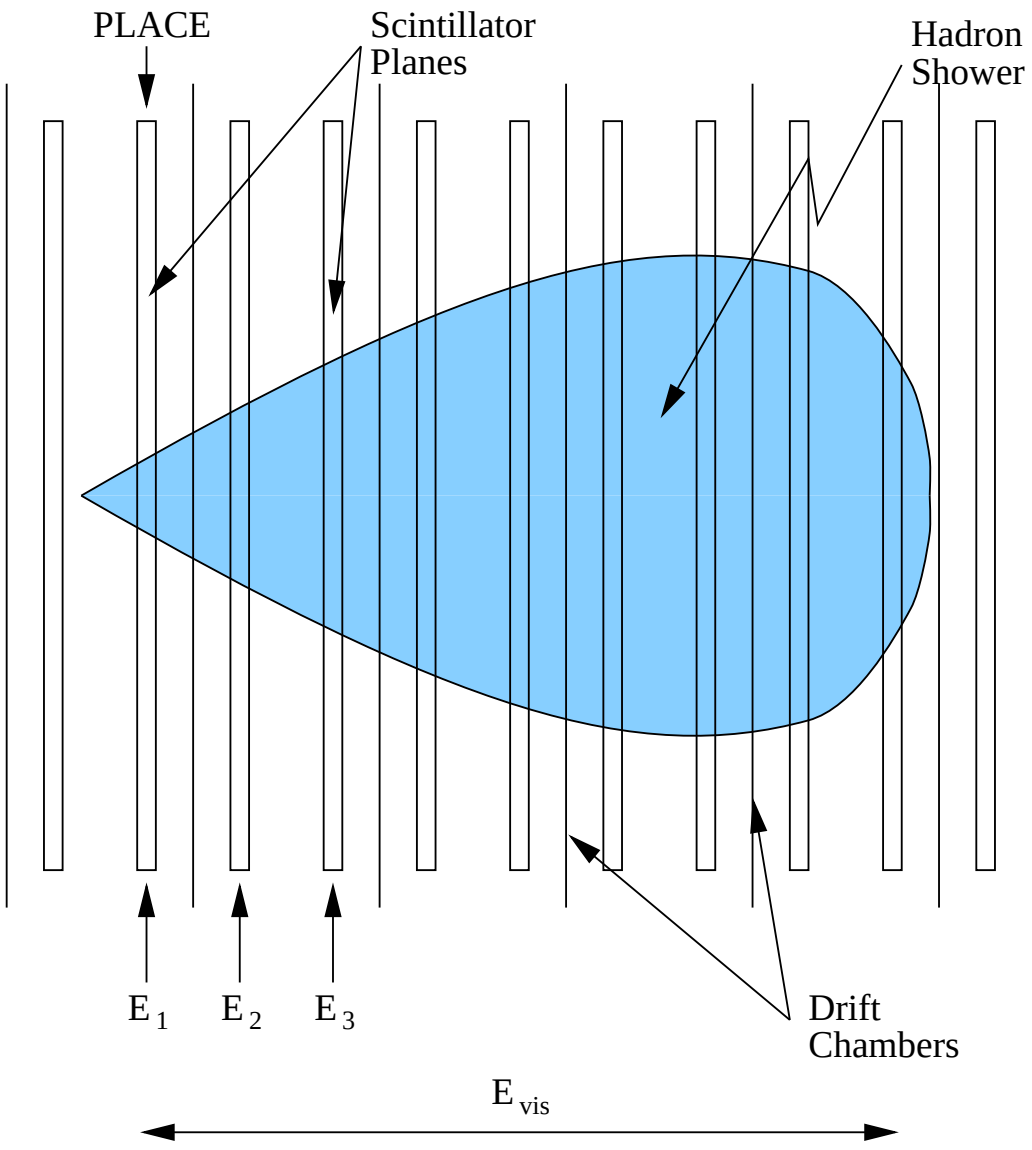

$$\eta_3 = 1 - \frac{E_1 + E_2 + E_3}{E_{vis}}$$

Figure 5.4: Definition of the event shape variable η_3.

5.2 Event Classification

Since ν_e CC events have no muon track, we isolate these events by partitioning the event sample into events with a muon track and events without one. Typical event displays from ν_μ NC and CC interactions are shown in Figure 5.5. The muon produced in CC interactions is clearly visible in the event display pictures as both hits in the drift chambers and, more important for this analysis, as small energy deposits in the scintillation counters. The presence of this penetrating muon allows us to isolate the events without a muon track simply by partitioning the event sample of neutrino interactions by length.

The simplest partition scheme employed by previous CCFR analyses uses a fixed number of counters, L_{NC}, as cut off where $L_{NC} = 30$ counters. The neutrino events are divided into two classes: "short" if the event length is shorter than L_{NC}, and "long" otherwise . This cut off was chosen to include all the NC events in the "short" category. Accordingly, the "long" events consist almost exclusively of class 1 events, while the short ones are a mixture of class 2, class 3, and class 1 events which cannot be separated on an event by event basis.

The main drawback of this method is that, especially at low energy, the fraction of CC events with a low energy muon contained in the short sample is on the order of 30%.

For this analysis, we attempt to reduce the short CC contamination by making the length cut energy dependent. We attempt to identify events with a muon track by studying the SHEND $-$ CEXIT distribution. For events with a muon track CEXIT will be in general far downstream of SHEND, while for events without a muon track CEXIT will be approximately equal to SHEND. Based on the distributions such as that shown in Figure 5.6, we isolate events without a muon track by requiring CEXIT to be less than 11 counters downstream of SHEND. We then parameterize the event length which contains 99% of such events for each E_{vis} bin as:

$$L_{NC} = 4. + 3.81 \times \log(E_{vis}) \tag{5.4}$$

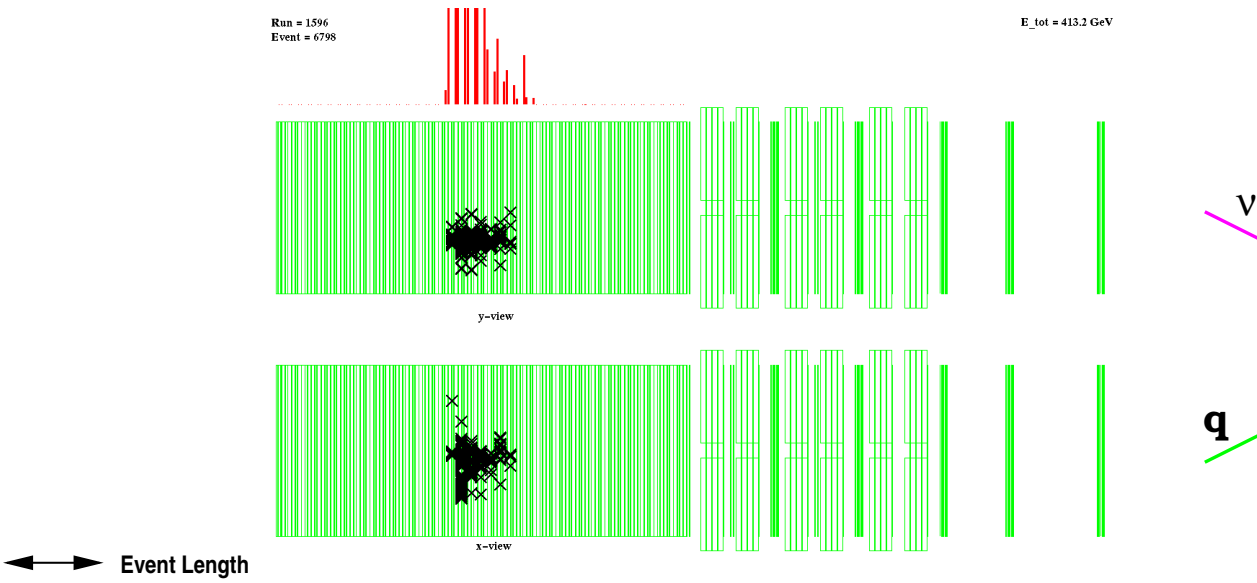

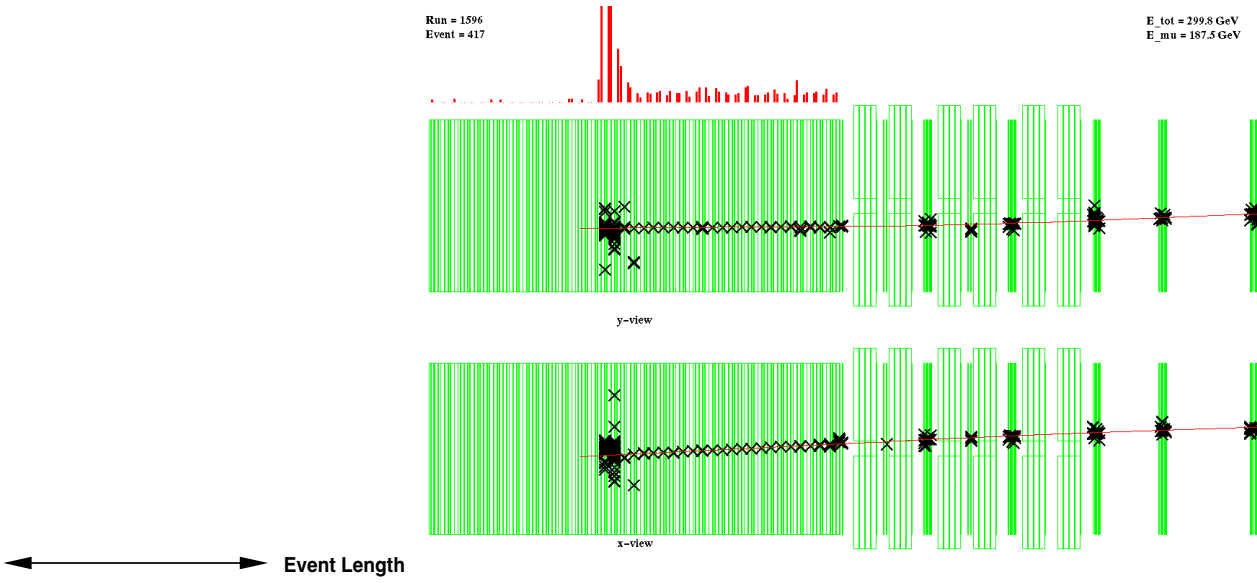

Figure 5.5: Event displays of typical "short" and "long" neutrino events in the CCFR detector.

Energy (GeV)	Long Evts.	Short CC Evts.	Frac. (%)
30 - 40	168852.8	19828.4	23.9
40 - 50	137987.2	18643.5	26.4
50 - 60	116427.4	18026.0	28.7
60 - 70	96174.6	15802.5	29.8
70 - 80	77691.2	13095.2	29.9
80 - 90	64549.5	10500.4	29.0
90 - 105	77888.1	11968.0	27.4
105 - 120	62092.6	8458.7	24.7
120 - 135	50738.2	6000.7	21.9
135 - 150	42199.3	4701.8	20.6
150 - 175	57353.9	6463.3	20.7
175 - 200	44866.5	5793.3	22.7
200 - 250	56233.5	9053.1	26.9
250 - 300	25527.7	4357.6	28.4
300 - 600	20599.5	3556.8	29.5

Table 5.2: Fraction of ν_μ CC events with a length shorter than 30 counters. These are mostly events with a low energy muon in the final state (Monte Carlo prediction).

and use this as our new energy dependent cut off length.

In order to compare the number of events predicted by the Monte Carlo and in the data we need to normalize the Monte Carlo sample to the data. We use the long events to normalize the Monte Carlo to the data since their length distribution is much better understood than for short events: PLACE is uniformly distributed in the detector smeared by the NN PLACE distribution, and CEXIT involves tracking the muon through the calorimeter. Conversely, the length of short events is determined by the end of the hadron shower which is harder to simulate. Figure 5.7 shows a good agreement between the length distribution of long events from the data which exit in the calorimeter (CEXIT > 3) and the corresponding Monte Carlo prediction. The Monte Carlo is normalized to the data using the total number of long events with $E_{vis} > 30$ GeV. Any variation as a function of energy is taken as a systematic error.

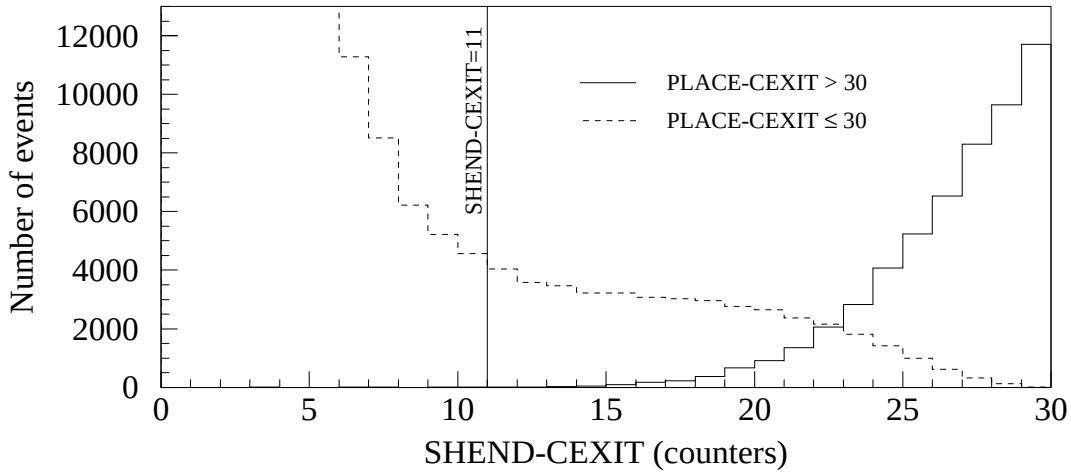

Figure 5.6: SHEND − CEXIT distribution for events longer than 30 counters (solid) and shorter (dashed) with $E_{vis} > 30$ GeV. We isolate events without a muon track by requiring SHEND − CEXIT ≤ 10.

5.3 Cuts

During the running of the E770 experiment, 5,166,884 events were written to tape. The data were divided into runs by inserting end of file markers onto the tape to mark significant changes in run conditions such as a change in toroid polarity, beam intensity or a stoppage caused by malfunction in the detector electronics. For this analysis, the full data sample is reduced by a series of cuts. The cuts impose precisely defined requirements on the data and are designed to remove backgrounds, poorly reconstructed events, overlaid or multiple interaction events and other anomalies.

The cuts applied to the data and the number of events passing each cut are given in Table 5.3. The cuts are:

- **Bad Runs.**

  Examination of the E770 run log books resulted in the removal of some runs from the analysis because of detector malfunctions or problems with the neutrino beam.

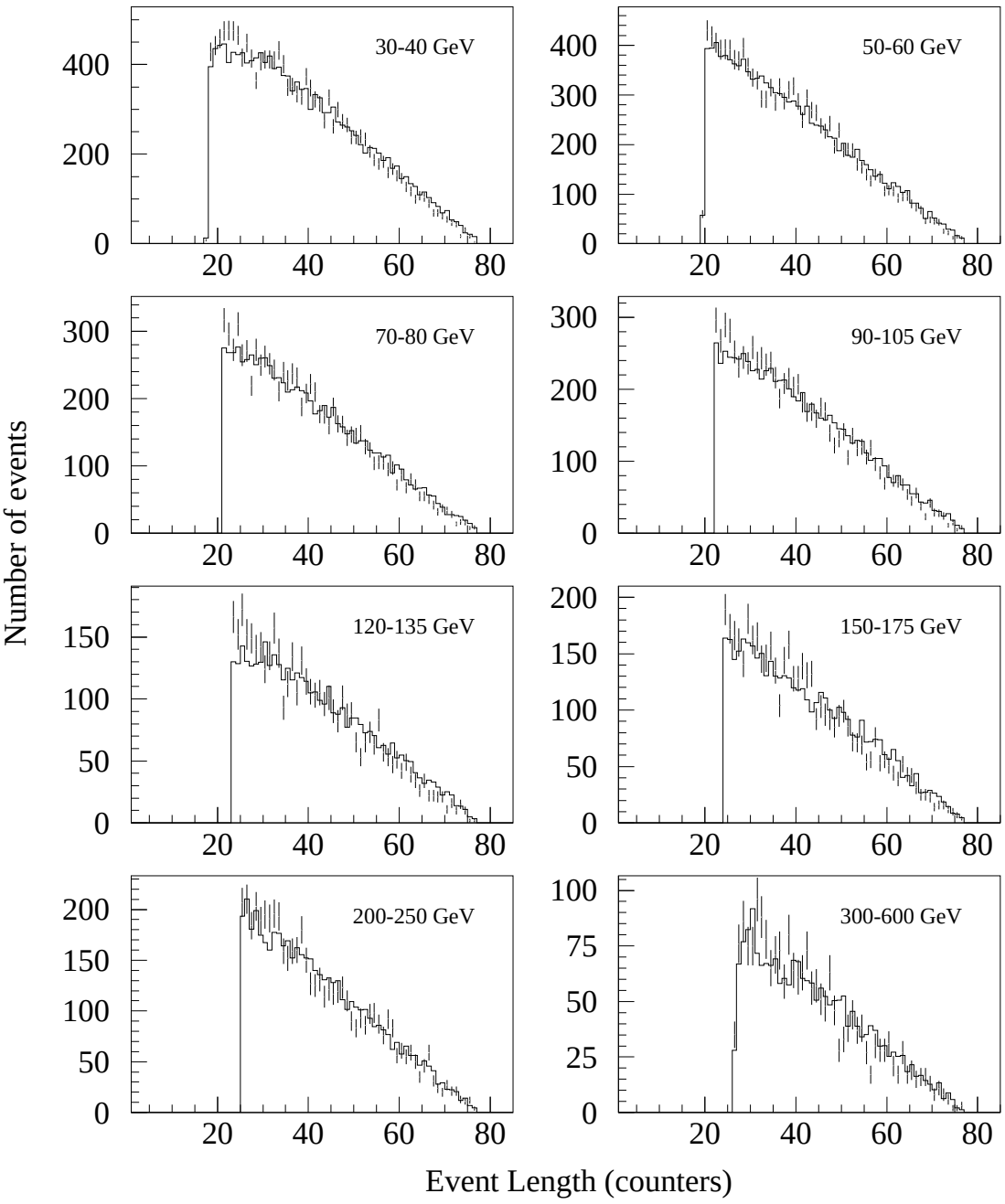

Figure 5.7: Event length distribution for long events for which the muon exits in the calorimeter ($CEXIT > 3$) for various E_{vis} bins. Data (bars) compared to Monte Carlo prediction (solid line).

Cut	Events passing cut	(failing cut)
	5166884	
bad runs	5078655	(88229; 1.7%)
phantom events	5068964	(9691; 0.2%)
data + cosmic gate	4745431	(323533; 6.4%)
event time	4534293	(211138; 4.4%)
trigger 6	3445559	(1088734; 24.0%)
radial vertex pos.	2298016	(1146543; 33.3%)
adc noise	2296270	(1746; 0.1%)
interaction region	2295277	(993; 0.0 %)
deep mu	2189202	(106075; 4.6%)
long. vertex pos.	1538601	(650601; 29.7%)
trigger 6 inefficiency	1538245	(356; 0.0%)
trigger requirement	1530872	(7373; 0.4%)
E_{vis}	926493	(604379; 39.5%)

Table 5.3: The cuts which reduce the raw data sample to the final sample.

- **Data Gate.**

  Events from gates other than the neutrino (fast spill) gate (gate 1-4) or cosmic gate (gate 7) were discarded. Events taken during the cosmic gate were analyzed the same as neutrino events and were used for background subtraction.

- **Event Time.** The event time is measured at each counter using the same time-to-digital converters used for the drift chambers. The s-bit pulse is fed to the TDC providing a time resolution of 4 ns. When information from all active counters is combined, the overall event time resolution has an rms of 2.4 ns. "Out of time" events and events with more than one "in time" interactions were removed from the final data sample. A neutrino interaction is classified as being "in time" if the event time as measured from the s-bits (see page 57) agrees to within 36 ns to the one predicted from the trigger. Figures 5.8 (a) and (b) show that the timing resolution is good enough such that this cut doesn't remove too many legitimate events.

- **Straight through muon cut.**

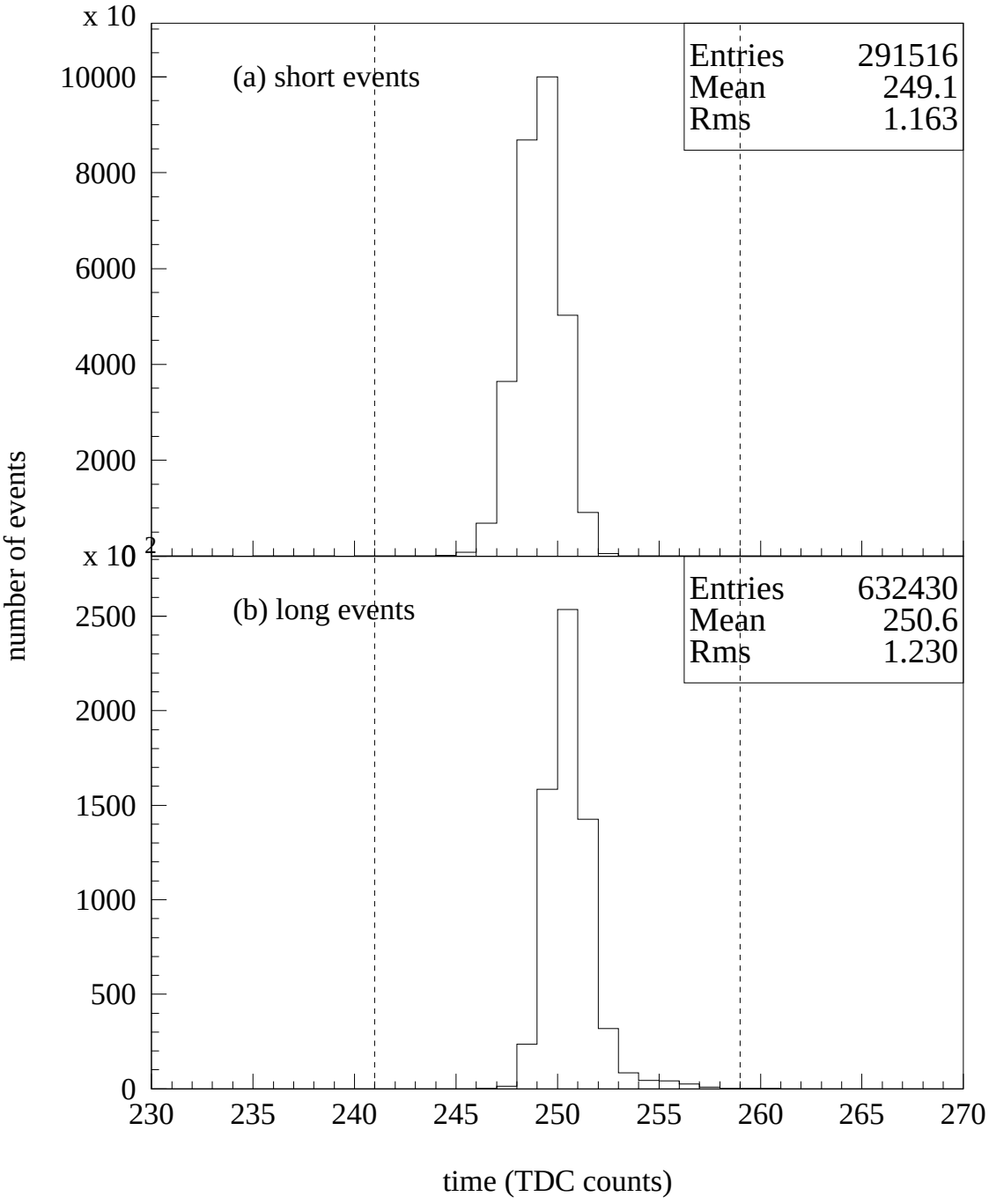

Figure 5.8: Event trigger time distribution for **(a)** short events (require trigger 2 or 3) and **(b)** long events (require trigger 1 or 3), and with $E_{vis} > 30$ GeV. Each clock count is 4 ns. The analysis cut requires a trigger time in the range 241 to 259 clock counts, inclusive.

All the events which fired trigger 6 were removed from the final sample. To account for trigger 6 inefficiency events for which the start of the interaction region was less than five counters away from the upstream end of the detector and any three of the first five counters had more than .25 MIPs were also removed.

- **Fiducial volume cut.**

  We require SHEND to be more than five counters upstream of the downstream end of the detector (*i.e.* SHEND ≥ 6). This ensures an unbiased calculation of E_{vis} for all hadron showers. Additionally, we require PLACE to be more than 5 counters from the downstream end of the target and five counters plus the separation length from the downstream end (*i.e.* $5 + \mathrm{L_{NC}} \leq \mathrm{PLACE} \leq 78$). This allows for (i) an unambiguous partition of the neutrino interactions by event length, and (ii) full containment of the hadron shower.

  The transverse interaction vertex is required to be less than 50 inches from the detector centre-line. The algorithm for finding the transverse vertex position failed for a small fraction of events(.31% for a 20 GeV E_{vis} cut). It was assumed that some of these events are cosmic rays at the edges of the detector. This cut was chosen such that it maximizes the event sample while making sure the hadron shower is still fully contained in the target calorimeter.

- **Phantom Events**

  The digitized detector information for up to 32 events, stored in the TDC's for the drift chamber hits and the s-bits and in the FERAs for the pulse heights, was read out all at once at the end of each ping. The three data branches were read out in parallel independent of each other and were matched by the data acquisition program. Readout problems with any one of the branches caused a mismatch of the data where information from different events in a readout cycle was matched together

in one event. We identify such events by determining the interaction region based on information from the scintillation counters, and from information from the s-bits which are equivalent to 1/4 MIP. We require the upstream and downstream end of the interaction region for the two methods to agree to within 3 counters for each method. Additionally, a visual inspection of all the events in a cycle which contains an event which failed the cut was performed, and the whole cycle was thrown out if it looked like there was a readout problem.

- **Deep-mu events**

  Muons passing through the detector deposit, on average, one MIP per scintillation counter due to ionization losses. It is also possible for muons to lose energy catastrophically as a result of interactions in the detector. These showers are electromagnetic in nature. For a low y neutrino event with a muon track ($\nu_\mu CC$) the place finding algorithm will fail to find the start of the neutrino interaction at the event vertex but will instead identify the deep μ interaction as the vertex. Figure 5.9 shows an example of such an event.

  Deep-mu events have a muon track, and as such, most of these events will end up in the long sample[1] which is assumed to be purely hadronic. The presence of electromagnetic showers will cancel the signature of ν_e CC interactions present in the short sample, so it is important to remove them.

  To identify a cut for removing deep-mu events without introducing a strong bias in the neutrino event sample, we studied the distribution of the number of counters between the beginning of the neutrino interaction region, ISTRT, and PLACE.

  We require:

$$\text{ISTRT} - \text{PLACE} \leq 5 \tag{5.5}$$

[1] For a definition of long events see page 93

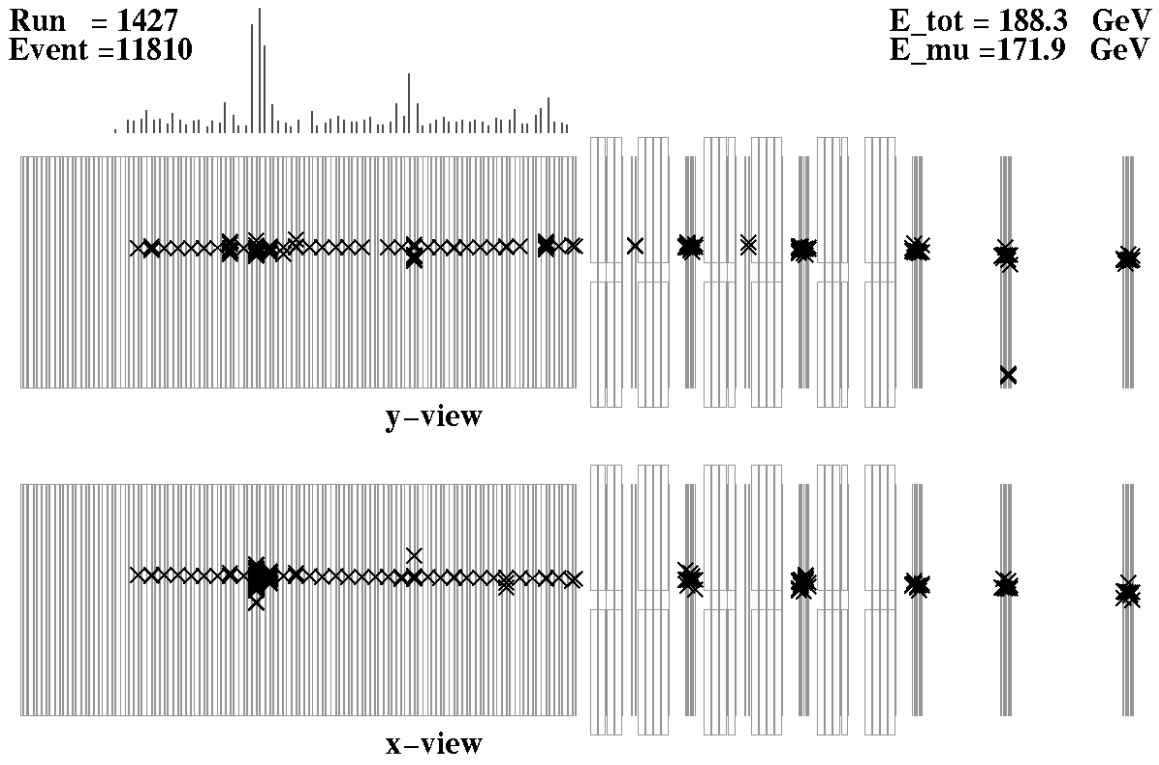

Figure 5.9: An event which failed the deep-mu cut (ISTRT − PLACE ≤ 5). This event is most likely a neutrino induced deep-mu event.

to eliminate as many of the deep-mu events as possible. To study the events removed by the cut, we look at the energy deposition profile distribution of such events. If the events removed are indeed deep-mu events, then the energy deposition profile distribution should be comparable to that of electromagnetic showers.

- **Energy**.

  A minimum E_{vis} cut of 30 GeV (i) ensures complete efficiency of the energy trigger, (ii) rejects low energy events spanning too few counters for an accurate measurement of the energy deposition profile, and (iii) reduces cosmic ray and deep-mu contamination.

- **Trigger requirement**

  This cut removed long events which didn't fire trigger 1 or 3, and short events which

didn't fire trigger 2 or 3.

5.4 Analysis Procedure

The analysis assumes that hadron showers produced in NC and CC interactions have the same energy deposition profile (characterized by the η_3 distribution) and calibration in the calorimeter. It is possible for the calibration and η_3 to differ because the two shower types have different mean electromagnetic components. A Lund Monte Carlo simulation[2] provided the conservative estimate that the energy calibration for CC and NC hadron showers differ by no more than 0.4%. The Lund generated showers were input into a GEANT simulation and tracked in the calorimeter. We used a Kolmogorov test to compare the shape of the η_3 distributions for neutral and charged current showers, and the distributions were found to be statistically the same. For a more detailed description see Section 5.5. To measure the number of ν_e CC events we compare the η distributions of "long" and "short" events. Any difference is attributed to the presence of ν_e CC interactions in the short sample.

5.4.1 η_3 Distribution for "short" Events

To compare directly the long and short events we need to compensate for the absence of a muon in NC and ν_e CC events. The muon energy loss distribution consists of a pronounced peak due to ionization loss and a long tail due to less frequent catastrophic energy losses, with the most probable energy loss being one MIP (see page 46). This has the effect of smearing the energy distribution of the hadron shower. Three different approaches for making this correction were considered:

1. Subtract in software one MIP for each counter of the hadron shower. Although it corrects for the most probable muon energy loss, this method lacks proper treatment of the catastrophic loss which in the lower energy bins can be a significant fraction of the total energy deposited in each scintillation counter.

[2]Lund is a hadron shower MC which is used widely in high energy physics

2. Modify CC events by subtracting in software the random pulse heights corresponding to a muon track from the data. This method attempts to correct for the muon catastrophic energy loss by unsmearing the hadron shower energy distribution. Unfortunately, this correction is made on a statistical basis so for any pulse height it can be wrong by as much as twice the spread of the distribution since the subtraction does not mimic the actual muon energy loss. To understand this, consider the example of one counter in which the muon deposits $1+\sigma$ MIPs of energy total where sigma is the spread of the distribution characterizing the muon energy loss (we cannot measure this in the data but we can assume it for the sake of the argument). Let's also assume that the pulse height of the muon track we subtract is $1-\sigma$ MIPs. Subtracting the two values one can easily see that we end up adding a 2σ MIPs to the CC hadron shower pulse height which is not in the NC hadron shower. Of course, we are just as likely to end up subtracting 2σ MIPs from the CC hadron shower pulse height, and on average the discrepancy will be zero, but this method has the effect of introducing a noise term in the CC hadron shower energy distribution which is not present in the equivalent NC showers.

3. Modify NC events by adding in software the pulse heights corresponding to a muon track from the data. Adding a μ track to the NC hadron showers properly takes into account the energy fluctuations of the muon energy loss and it has the effect of smearing the NC hadron shower energy distribution in a manner similar to that of CC hadron showers. The effect of this correction on the η_3 for the short events is shown in Figure 5.10. As expected the correction is significant for the lower energy events and negligible at higher energy where the muon energy loss is only a very small fraction of the total energy deposited in each scintillation counter.

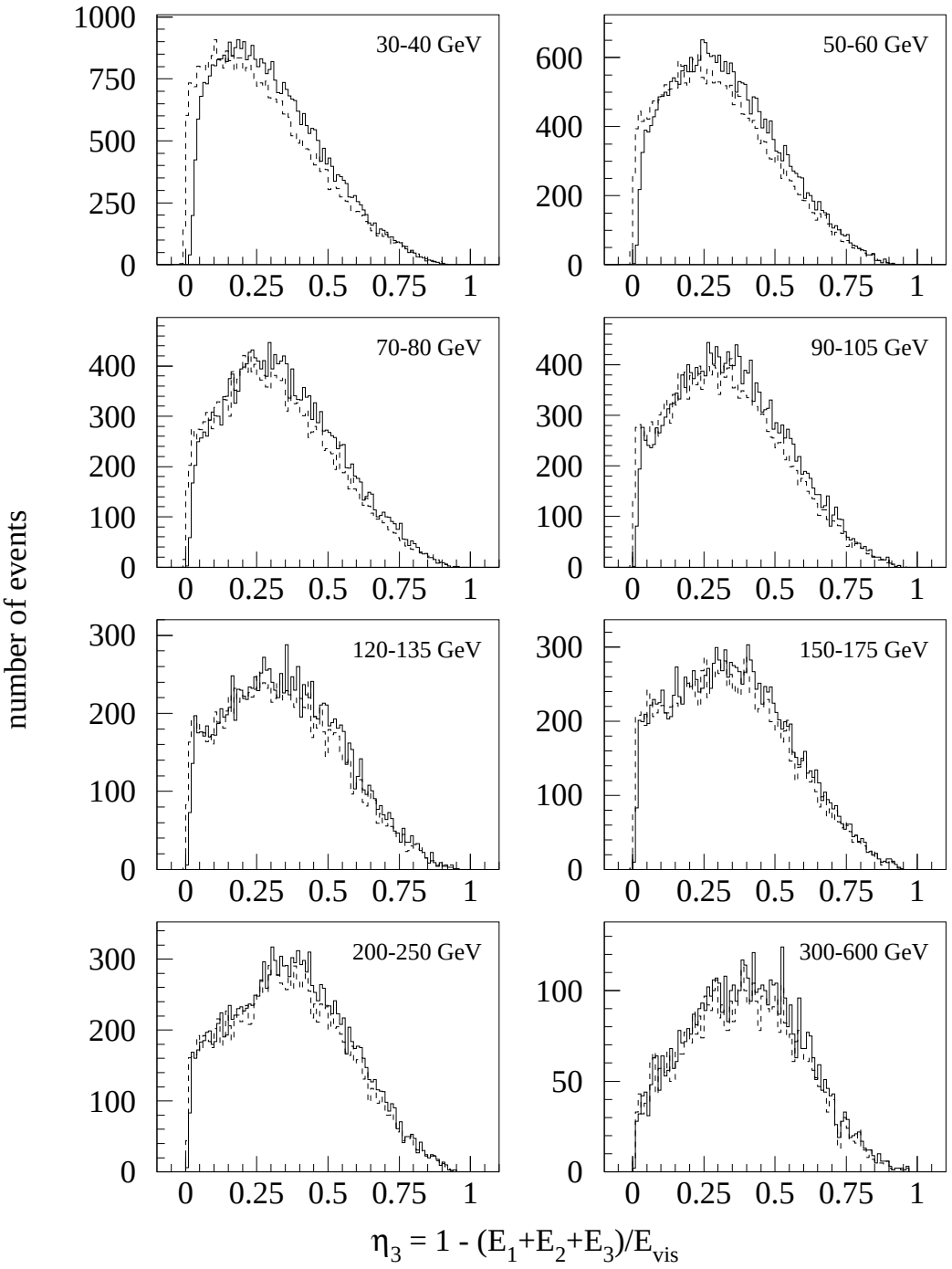

Figure 5.10: The effect on the η_3 distribution when adding a muon track to the short events sample. The solid line is the corrected distribution and the dashed line is the uncorrected one.

For this analysis we choose method 3 to correct for the absence of a muon track in NC ν_μ events. The muon tracks are obtained from the data by using the pulse heights of muons in long events for each of the E_{vis} bins separately. We ensure that the muon is uncontaminated in two ways: (i) the sampled pulse heights begin 10 counters downstream of the hadron shower, (ii) the first two consecutive pulse heights used must be < 3 MIPs to eliminate the case where the muon track starts in the middle of a deep-mu shower which would be unphysical.

5.4.2 Other Corrections to the η_3 Distribution

Since short events contain CC events with a low energy muon track which doesn't exit the shower, the short sample now contains a fraction of events with two muon tracks: a short one, the result of the muon coming from the CC neutrino interaction, and a long one added in the software. This category of events is not present in the long sample and we need to correct for it. The fraction f of ν_μ CC events with a low energy muon was estimated from the Monte Carlo (see Table 5.4), together with the E_{vis} distribution. A simulated sample of such events was obtained by choosing long events with the right energy distribution from the data to which a second muon track was added in the software. The pulse heights of the muon track were corrected by $1/\cos\theta$, where θ is the angle of the muon track with respect to the direction of the incident neutrino. The length of the short track and the angular distribution were obtained from a Monte Carlo of ν_μ CC events and are shown in Figures 5.11 and 5.12 respectively.

We correct the η_3 distribution of short events for background short ν_μ CC events by subtracting the η_3 distribution of the simulated sample of short ν_μ CC events for each $Evis$ bin separately. The total number of simulated short ν_ν CC events in each E_{vis} bin was normalized to the number of such events in the short sample predicted by the Monte Carlo.

Additionally, we also have to correct the η_3 distribution for both long and short events

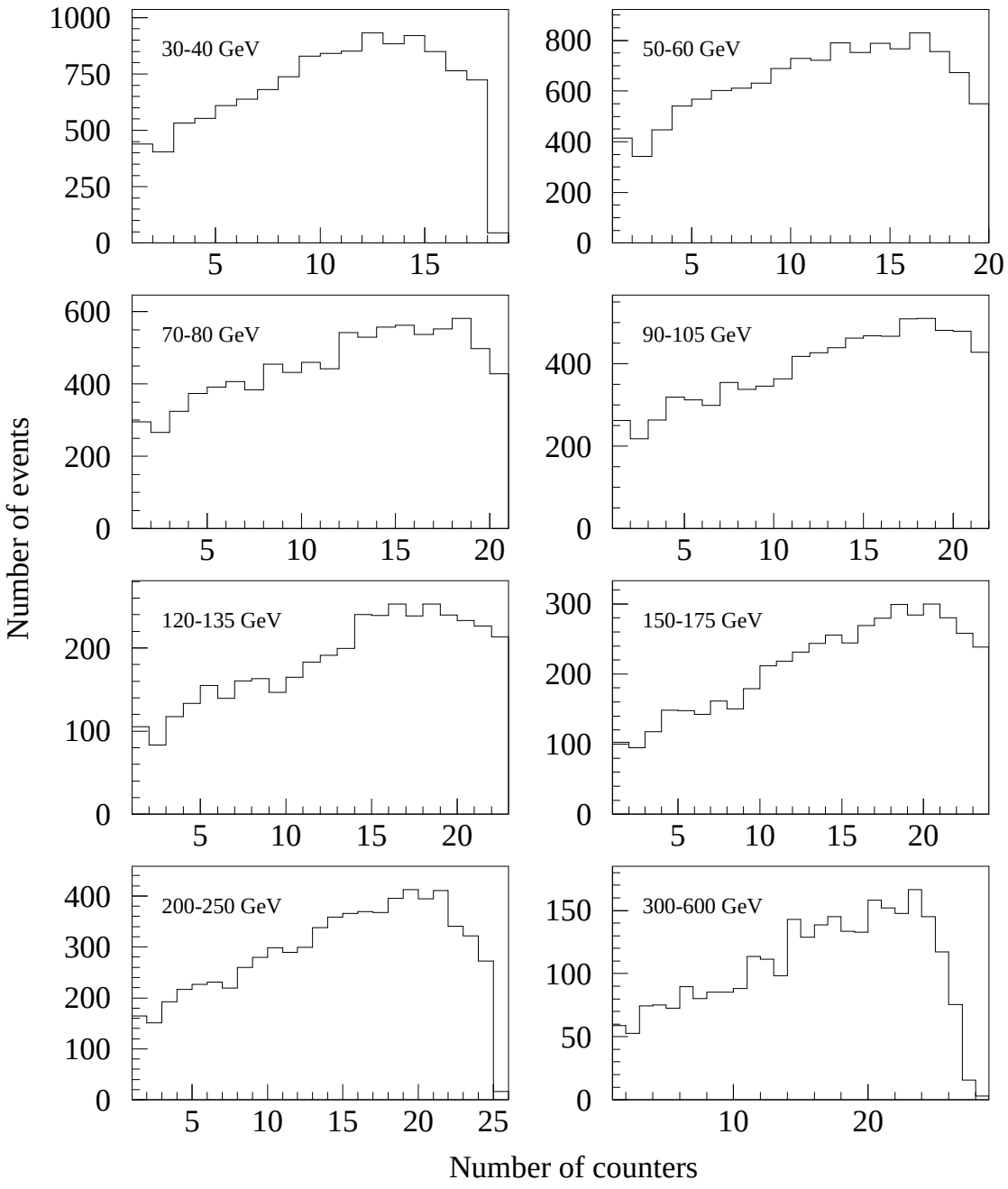

Figure 5.11: Length distribution of the muon track produced in short charged current interactions, where "short" is defined in the text (Monte Carlo prediction).

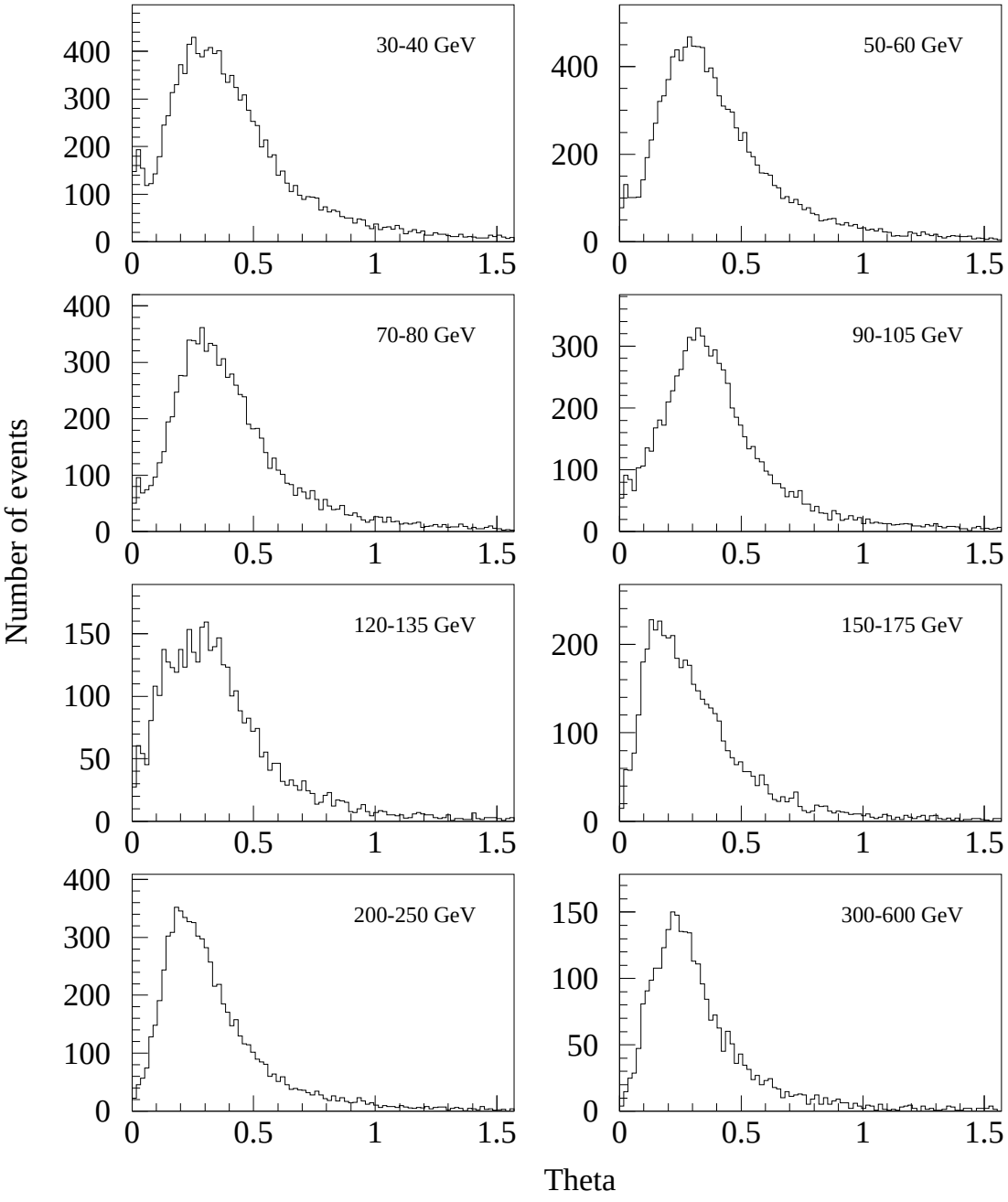

Figure 5.12: Angular distribution for short charged current events as predicted by the Monte Carlo. This distribution is used to correct by $1/\cos\theta$ the short muon track added in software to a fraction f of long events.

for background cosmic ray events. The cosmic ray background was estimated from the event sample collected during the cosmic ray gate using an identical event selection algorithm as for the data gates. The cosmic ray gate collected a total of 2911 events which pass all the analysis cuts. Of these events 2871 are short and 40 are long. Table 5.5 lists the number of cosmic ray events in each of the 15 E_{vis} studied. Unfortunately, the collaboration neglected to determine the exact ratio of live-times of the data and cosmic ray gates. The cosmic ray gate was estimated to be approximately 3 times longer than the sum of the data gates (gates of approximately 2 μs for each of the three bursts of neutrinos in a cycle of the Tevatron accelerator). Accordingly, we scale the cosmic ray η_3 distribution by 1/3. The cosmic ray correction affects mostly the short event sample at low energies. For the long events this is a negligible effect since, as shown by Table 5.5 there are very few long cosmic ray events. The correction is applied to the long events only for the sake of completeness.

The corrected η_3 distributions for short, long events, and ν_e events for various energy bins are shown in Figure 5.13.

5.4.3 Electron Neutrino Sample

To simulate ν_e interactions in the detector we assume $\nu_\mu - \nu_e$ universality. The electron neutrino events were generated by convoluting hadron showers taken from the long sample with electromagnetic showers generated by a GEANT simulation. In this way, the electron events also included an extra muon track. The interaction point for the GEANT showers was distributed uniformly in the steel plate, the same as for neutrino interactions. In order to be able to add GEANT generated showers to hadron showers from the data we need to convert the electron energy loss in the scintillation counters from the GEANT simulation to the equivalent energy of the incoming electron in GeV. The equivalent energy scale of the GEANT generated showers was calculated by dividing the energy of the incoming electron in GeV to the total energy loss in the scintillation counters. Table 5.6 lists the calibration

Energy (GeV)	Long Evts.	Short ν_μ CC	Frac. (%)
30 - 40	280403.2	8521.9	12.6
40 - 50	232427.1	11778.5	15.2
50 - 60	187263.5	11873.9	17.8
60 - 70	155872.1	12149.2	19.1
70 - 80	127349.1	11023.4	20.0
80 - 90	101615.4	9436.9	19.5
90 - 105	83360.1	7678.3	19.0
105 - 120	98898.2	8955.9	16.9
120 - 135	77474.3	6243.9	15.2
135 - 150	62312.4	4544.0	13.9
150 - 175	51702.5	3442.8	14.7
175 - 200	68976.8	4955.5	16.9
200 - 250	53814.9	4602.4	21.3
250 - 300	66543.8	7560.7	23.5
300 - 600	29485.0	3743.5	25.4

Table 5.4: Fraction of ν_μ CC events contained in the "short" sample. These are mostly events with a low energy muon in the final state (Monte Carlo prediction).

Energy (GeV)	Short CR	Long CR
30 - 40	1344	21
40 - 50	569	7
50 - 60	325	4
60 - 70	189	3
70 - 80	91	0
80 - 90	87	1
90 - 105	75	1
105 - 120	61	2
120 - 135	35	0
135 - 150	23	0
150 - 175	21	1
175 - 200	5	0
200 - 250	24	0
250 - 300	7	0
300 - 600	15	0
TOTAL	2871	40

Table 5.5: Number of cosmic ray events as a function of energy. The majority of such events are classified as low energy short events.

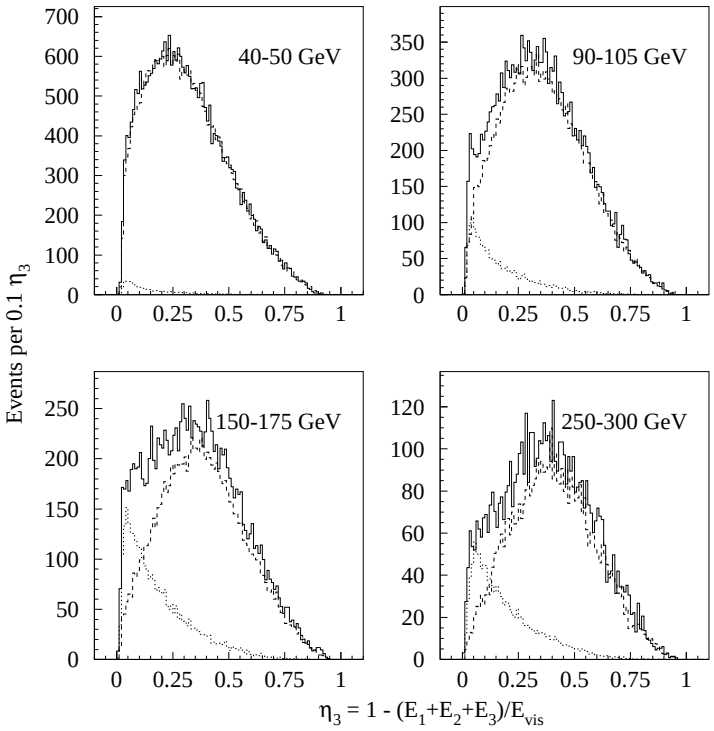

Figure 5.13: Eta distributions for short, long and ν_e events in 4 different energy bins.

constants for each of the energy bins studied. The overall calibration constant is equal to 41.95 GeV, and it was calculated for incoming electron energies greater than 30 GeV.

The energy distribution of the electron neutrinos and the fractional energy transfer y were generated using the Monte Carlo simulation of the experiment. The hadron shower energy was smeared by the hadron energy resolution calculated from the CCFR test beam calibration run to be $0.89\sqrt{E}$. The electromagnetic showers were smeared by the GEANT electron shower simulation, *i.e.* we look up an electromagnetic shower generated by an electron of the same energy as the requested energy, and multiply the pulse heights by the above-described calibration scale factor. The resolution functions for some of the energy bins studied are shown in Figure 5.14. For energies greater than 30 GeV the resolution is Gaussian and agrees with the resolution measured from the CCFR test beam calibration run of $0.6\sqrt{E}$. The high tails at low energies are due to the coarse granularity of the detector

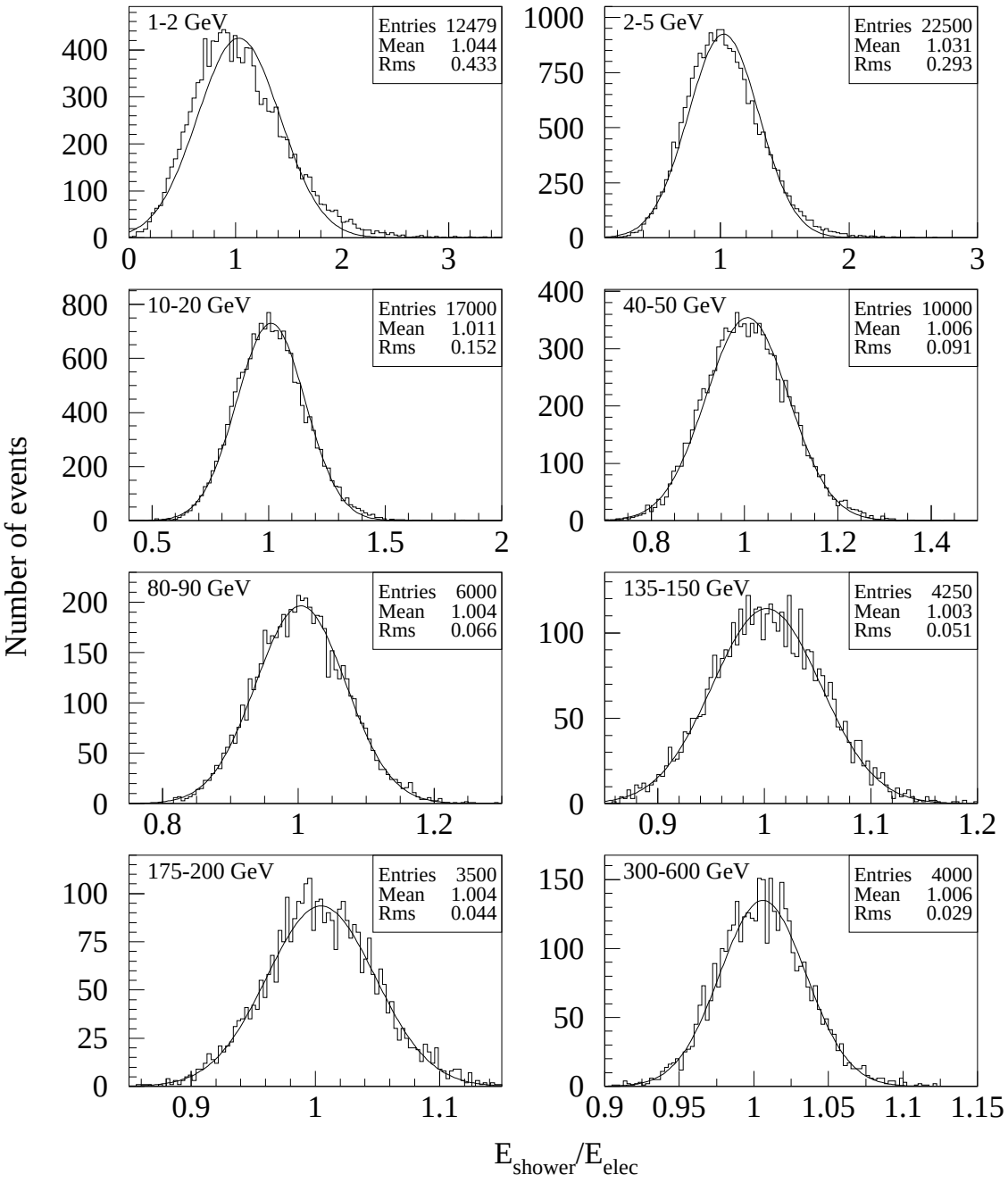

Figure 5.14: Resolution function for GEANT generated electromagnetic showers. The curves are Gaussian parametrizations of the data.

Energy (GeV)	Calib. Fact.	Variance	Energy (GeV)	Calib. Fact.	Variance
0 - 2	136.7	859.4	80 - 90	42.0	2.8
2 - 5	44.4	14.8	90 - 105	41.9	2.6
5 - 10	42.8	9.3	105 - 120	41.9	2.4
10 - 20	42.4	6.6	120 - 135	41.9	2.3
20 - 30	42.2	5.1	135 - 150	41.9	2.1
30 - 40	42.1	4.4	150 - 175	41.8	2.1
40 - 50	42.0	3.8	175 - 200	41.8	1.9
50 - 60	42.0	3.5	200 - 250	41.9	1.7
60 - 70	42.0	3.2	250 - 300	41.8	1.6
70 - 80	41.9	3.0	300 - 600	41.7	1.2

Table 5.6: Equivalent energy scale calibration factor for electromagnetic showers in GEANT.

with scintillation counters only every 6 radiation lengths. Since the hadron showers used to generate ν_e CC events already have a muon track, the ν_e sample can be compared directly with the short and long events.

5.4.4 Extraction of ν_e events

Electron neutrino charged current interactions initiate a cascade of hadrons that is registered by the drift chambers and the scintillation counters. Additionally, the electron produced in the final state deposits energy in the counters immediately downstream of the interaction place. The electromagnetic shower is typically much shorter than the hadron shower and the two cannot be separated for an individual ν_e CC event. Since ν_e events don't have a muon in the final state they appear short in the target-calorimeter, just like ν_μ NC events. Accordingly, the "short" sample consists of ν_μ NC and ν_e CC events (after we correct for background short ν_μ CC and cosmic ray events as described in Section 5.4.2), while the "long" sample consists only of ν_μ CC events.

The η_3 distribution for "short" events is a combination of distributions for purely hadronic events (ν_μ NC and ν_e NC) and events with a hadron shower and an electromagnetic shower, while the η_3 distribution for the "long" sample is determined only by hadronic events. As discussed previously, the electromagnetic shower present in ν_e CC in-

teractions changes the energy deposition profile for such events. Since we believe that the energy deposition profiles of hadron showers produced in NC or CC neutrino interactions are the same, we can use the "long" sample to fix the η_3 distribution for hadronic events. Consequently, any difference in the η_3 distribution of the "short" sample from the reference distribution given by the "long" sample is attributed to the presence of ν_e CC interactions in the "short" sample.

We can extract the number of ν_e CC events in each E_{vis} bin by fitting the corrected shape of the observed η_3 distribution for the "short" sample to a combination of "long" and ν_e CC distributions with appropriate short muon additions:

$$\text{Short events} = \alpha(\text{Long events}) + \beta\ \nu_{\text{e}}\text{CC}(+\mu) \tag{5.6}$$

The χ^2 function is given by:

$$\chi^2 = \sum_{i\,\in\,\text{bins}} \left(\frac{(\eta_3)_i^{\text{Short}} - \alpha[(\eta_3)_i^{\text{Long}}] - \beta[(\eta_3)_i^{\nu_e}]}{\sigma_{\text{stat}}} \right)^2 \tag{5.7}$$

where each η_3 distribution is divided into 120 bins from -0.1 to 1.1, and σ_{stat} is the statistical error

$$\sigma_{\text{stat}}^2 = (\sigma^{\text{Short}})^2 + \alpha_0^2(\sigma^{\text{Long}})^2 + \beta_0^2(\sigma^{\nu_e})^2 \tag{5.8}$$

α_0 and β_0 are our initial estimation of α and β respectively, and σ^{Short}, σ^{Long}, and σ^{ν_e} are equal to the square root of the number of entries in each bin of the respective distributions.

For each E_{vis} bin we minimize this χ^2 by letting α and β float. Since χ^2 depends on the values of α and β, we use an iterative procedure with α_0 and β_0 being equal to the values from the previous fit. We repeat the fit until the values of α_0 and β_0 converge (typically 3 to 4 iterations).

Table 5.7 lists the values of α, β, the statistical error and the χ^2 from the fit in each of the 15 E_{vis} bins. The number of ν_e's in each E_{vis} bin is equal to the number of ν_e events in the simulated sample multiplied by β, and is listed in Table 5.8. For electron neutrinos,

E_{vis} (GeV)	α	$\delta\alpha$	β	$\delta\beta$	χ^2/DoF
30 - 40	0.33294	0.00281	0.01685	0.01855	0.8
40 - 50	0.33932	0.00313	0.04712	0.01635	0.8
50 - 60	0.33916	0.00346	0.07870	0.01473	0.9
60 - 70	0.34755	0.00394	0.05957	0.01368	0.6
70 - 80	0.34355	0.00435	0.09479	0.01241	1.0
80 - 90	0.34592	0.00485	0.11246	0.01158	1.3
90 - 105	0.35307	0.00451	0.17271	0.01286	1.4
105 - 120	0.35940	0.00530	0.19524	0.01223	1.0
120 - 135	0.35327	0.00578	0.19702	0.01098	1.2
135 - 150	0.34808	0.00632	0.18440	0.01041	2.0
150 - 175	0.34507	0.00563	0.30205	0.01267	1.4
175 - 200	0.35206	0.00642	0.22879	0.01057	1.1
200 - 250	0.36242	0.00606	0.25413	0.01190	1.8
250 - 300	0.35012	0.00877	0.11673	0.00763	1.3
300 - 600	0.36477	0.01006	0.07158	0.00625	0.8

Table 5.7: The values of the parameters α and β from the fit for each E_{vis} bin. $\delta\alpha$ and $\delta\beta$ are the respective errors from the fit.

E_{vis} (GeV)	ν_e sample	ν_e measured	ν_e error
30 - 40	9992	168.4	185.4
40 - 50	10050	473.5	164.3
50 - 60	10028	789.2	147.7
60 - 70	9997	595.5	136.8
70 - 80	10025	950.3	124.4
80 - 90	10016	1126.4	116.0
90 - 105	10031	1732.4	129.0
105 - 120	10014	1955.2	122.5
120 - 135	10016	1973.4	110.0
135 - 150	10002	1844.3	104.1
150 - 175	10022	3027.2	127.0
175 - 200	10005	2289.0	105.7
200 - 250	10023	2547.2	119.3
250 - 300	10000	1167.3	76.3
300 - 600	10010	716.5	62.5

Table 5.8: The number of electron neutrinos measured from the fit and the error for each E_{vis} bin. The column labeled "ν_e sample" lists the number of ν_e's in the simulated sample we used to extract the number of ν_e's in the data.

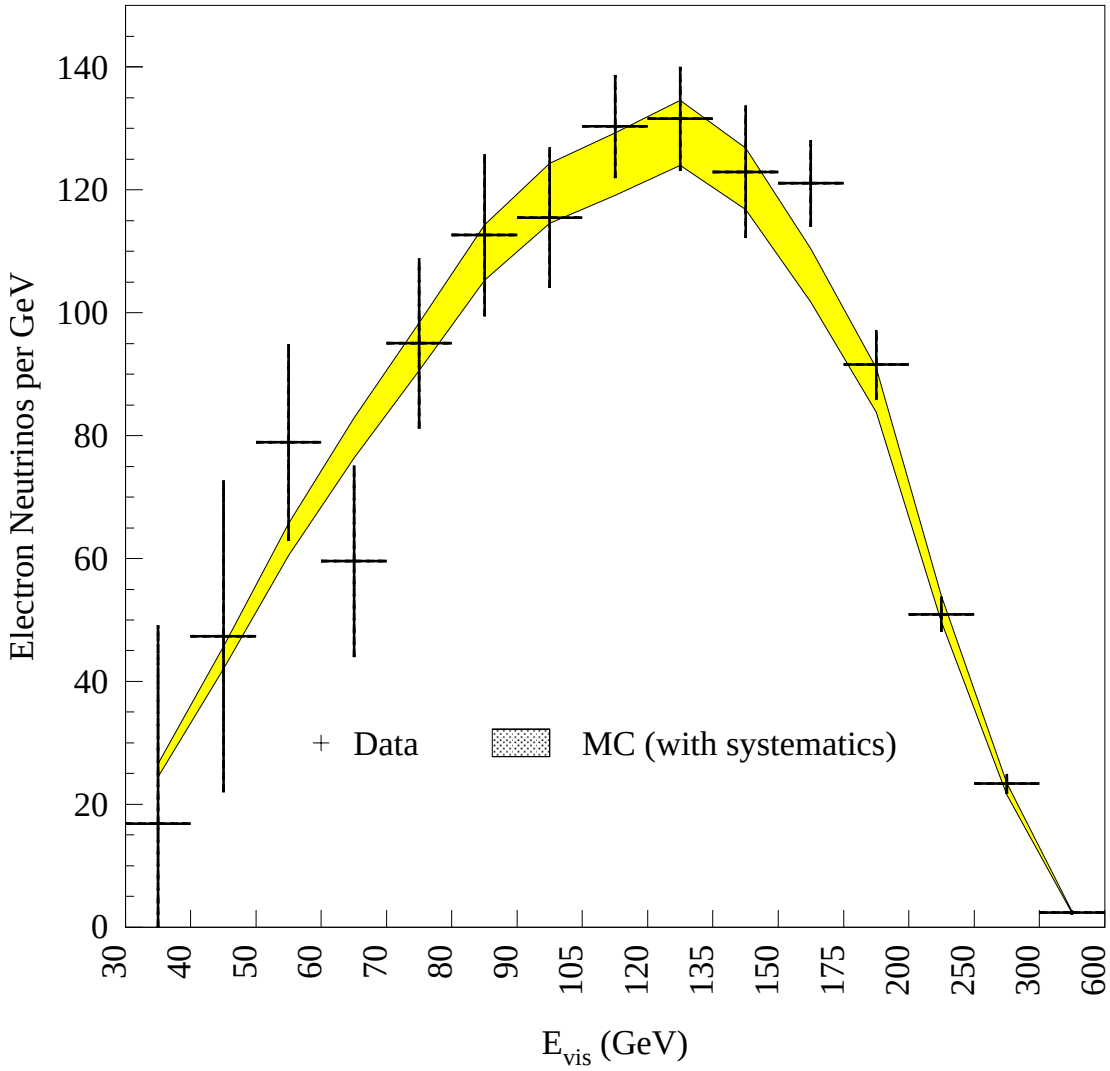

Figure 5.15: Number of electron neutrinos as a function of visible energy. For electron neutrinos the visible energy is equal to the total neutrino energy. The filled band shows Monte Carlo prediction.

E_{vis} is equal to the incoming neutrino energy. Figure 5.15 shows that the measured number of ν_e CC's agrees with the Monte Carlo prediction in each energy bin. The χ^2 for the comparison of the number of ν_e events to the Monte Carlo prediction is 9.97/15 degrees of freedom which has a probability of 80%.

5.5 Systematic Uncertainties

The major sources of uncertainties in the comparison of the electron flux extracted from the data to that predicted by the Monte Carlo are: the statistical error from the fit in extracting the ν_e events, the error in the shower shape modeling, the absolute energy calibration of the detector, and the uncertainty in the calculation of the incident flux of ν_e's on the detector. Other sources of systematic errors were also investigated and were found to be small.

5.5.1 Shower shape modeling

We estimate the error in the shower shape modeling by extracting the ν_e events using two definitions of η. Analogous to the definition of η_3 given in Equation 5.3, we define η_4 as:

$$\eta_4 = 1 - \frac{E_1 + E_2 + E_3 + E_4}{E_{vis}} \tag{5.9}$$

If the modeling of the showers were correct, the difference in the number of electron neutrinos measured by the two methods should be small, any difference is used as an estimate of the systematic error. Since this error can be shown not to be correlated among energy bins, we add it in quadrature to the statistical error from the fit and take this to be the combined basic error. Table 5.9 lists the number of ν_e's extracted using the two methods, and compares the difference to the statistical error from the fit.

We study the correlation among energy bins by extracting the ν_e events in one bin above 80 GeV using the same procedure described in the previous section. Using the original binning, the measured number of electron neutrinos above 80 GeV is 18378.9 using η_3 and 19160.6 using η_4 for a difference of 781.7 events. The number of electron neutrino extracted

Energy (GeV)	# ν_e's (η_3)	# ν_e's (η_4)	$\nu_e(\eta_3) - \nu_e(eta_4)$	fit error	combined
30 - 40	168.4	433.7	-265.3	185.4	323.7
40 - 50	473.5	666.7	-193.2	164.3	253.6
50 - 60	789.2	850.5	-61.3	147.7	159.9
60 - 70	595.5	520.3	75.3	136.8	156.1
70 - 80	950.3	888.8	61.5	124.4	138.8
80 - 90	1126.4	1189.5	-63.2	116.0	132.1
90 - 105	1732.4	1846.2	-113.8	129.0	172.0
105 - 120	1955.2	1984.8	-29.6	122.5	126.0
120 - 135	1973.4	2037.7	-64.3	110.0	127.4
135 - 150	1844.3	1968.6	-124.2	104.1	162.1
150 - 175	3027.2	3149.8	-122.7	127.0	176.6
175 - 200	2289.0	2382.9	-93.9	105.7	141.4
200 - 250	2547.2	2627.3	-80.2	119.3	143.7
250 - 300	1167.3	1193.0	-25.6	76.3	80.5
300 - 600	716.5	780.8	-64.2	62.5	89.6

Table 5.9: Number of CC ν_e's extracted using the η_3 and η_4 methods. The difference between the two methods is used to estimate the systematic error in the shower shape modeling.

in one single bin above 80 GeV is 18322.8 ± 354.8 using η_3, and 18663.7 ± 366.0 using η_4 for a difference of 340.9 events which is within the statistical error from the fit. From this we conclude that: (i) the number of measured ν_e's is not correlated among energy bins. (ii) the difference in the number of events measured by the η_3 and η_4 methods is an estimate of the systematic uncertainty in the shower modeling.

The shower modeling depends strongly on the experimental determination of the longitudinal vertex. A shift of one counter in PLACE would change: (i) The amount of energy deposited in the first three scintillation counters. We studied this effect by changing the value of PLACE by one counter downstream for all the showers and then recalculating the η_3 distribution. For each type of shower, we form a new η_3 distribution:

$$\eta_3^{\text{new}}(x) = (1-x)(\eta_3^{\text{orig}}) + x(\eta_3^{\text{shift}}) \tag{5.10}$$

where x is the fraction of events for which PLACE was shifted downstream by one counter. We vary x from 0 to 0.1 in steps of 0.01, and measure the change in the number of ν_e's. This

Energy (GeV)	misid. frac. (%)	Energy (GeV)	misid. frac. (%)	Energy (GeV)	misid. frac. (%)
30 - 40	5.15	80 - 90	4.07	150 - 175	2.75
40 - 50	5.15	90 - 105	4.07	175 - 200	2.73
50 - 60	5.15	105 - 120	3.91	200 - 250	2.99
60 - 70	4.16	120 - 135	3.91	250 - 300	3.19
70 - 80	4.16	135 - 150	2.75	300 - 600	2.80

Table 5.10: Fraction of events for which the place finding algorithm misidentifies the interaction vertex by 1 counter (Monte Carlo prediction).

is used to extract the systematic error due to the presence of a fraction x of events for which PLACE is misidentified. The fraction of such events is estimated from the NN PLACE distributions shown in Figure 5.2 and is listed in Table 5.10. The overall change in the number of ν_e's measured as a function of E_{vis} due to uncertainties in the determination of the NN PLACE is listed in Table 5.11. (ii) The muon track correction applied to the short events. We studied this effect by adding the muon track pulse heights starting one counter downstream from the NN PLACE. The η_3 distribution is calculated from the NN PLACE. Using the same procedure described above we calculate the change in the number of ν_e's measured which is listed in Table 5.12. (iii) The simulation of ν_e CC interactions. For this we assume the NN PLACE of the ν_e shower is known but that the electromagnetic shower was added one counter downstream from it. The change in the number of measured ν_e's due to this uncertainty is listed in Table 5.13.

5.5.2 Energy Calibration

The uncertainties in the energy calibration of the detector come from both the muon and hadron energy calibrations. The uncertainty in the muon energy calibration changes the energy scale of the relative flux extracted using low hadron energy CC events (events for which the muon carries most of the neutrino energy). On the other hand, an uncertainty in the hadron energy calibration directly affects the measurement of E_{vis}, the visible energy

E_{vis} (GeV)	$\Delta\nu_e$	E_{vis} (GeV)	$\Delta\nu_e$	E_{vis} (GeV)	$\Delta\nu_e$
30 - 40	1.0	80 - 90	3.5	150 - 175	40.9
40 - 50	5.8	90 - 105	10.5	175 - 200	24.3
50 - 60	0.7	105 - 120	12.2	200 - 250	10.9
60 - 70	7.9	120 - 135	24.1	250 - 300	0.6
70 - 80	10.0	135 - 150	17.2	300 - 600	7.1

Table 5.11: Change in the number of ν_e's measured due to events for which the interaction place was misidentified

E_{vis} (GeV)	$\Delta\nu_e$	E_{vis} (GeV)	$\Delta\nu_e$	E_{vis} (GeV)	$\Delta\nu_e$
30 - 40	-44.3	80 - 90	-3.3	150 - 175	-6.0
40 - 50	-20.5	90 - 105	13.0	175 - 200	2.5
50 - 60	1.8	105 - 120	-8.3	200 - 250	-5.8
60 - 70	-4.6	120 - 135	-6.4	250 - 300	-1.1
70 - 80	-10.7	135 - 150	8.3	300 - 600	0.7

Table 5.12: Change in the number of ν_e's measured due to short events for which the muon track correction was applied 1 counter downstream of the true interaction vertex.

E_{vis} (GeV)	$\Delta\nu_e$	E_{vis} (GeV)	$\Delta\nu_e$	E_{vis} (GeV)	$\Delta\nu_e$
30 - 40	9.9	80 - 90	20.2	150 - 175	45.8
40 - 50	7.4	90 - 105	39.7	175 - 200	35.3
50 - 60	13.0	105 - 120	39.4	200 - 250	44.0
60 - 70	7.9	120 - 135	44.3	250 - 300	24.6
70 - 80	20.4	135 - 150	24.3	300 - 600	15.3

Table 5.13: Change in the number of ν_e's measured due to adding the electron shower 1 counter downstream of the interaction vertex when simulating ν_e events.

E_{vis} (GeV)	$\Delta\nu_e$(mu)	$\Delta\nu_e$(had)	E_{vis} (GeV)	$\Delta\nu_e$(mu)	$\Delta\nu_e$(had)
30 - 40	-14.7	-0.1	120 - 135	16.8	10.4
40 - 50	9.6	-11.9	135 - 150	-87.5	39.3
50 - 60	1.8	1.2	150 - 175	-72.8	-51.3
60 - 70	2.5	20.0	175 - 200	-8.9	-32.5
70 - 80	4.3	36.5	200 - 250	44.7	17.8
80 - 90	8.0	-3.9	250 - 300	30.3	-16.2
90 - 105	-21.2	41.4	300 - 600	55.0	-22.2
105 - 120	-18.5	-3.0			

Table 5.14: Effect on the number of ν_e's predicted by the Monte Carlo from the 1%uncertainty on the calibration for the muon and hadron energy.

deposited in the calorimeter, and hence the neutrino flux. The calibration for the muon and hadron energy is known with an uncertainty of 1% [51]. The effect of the detector calibration on the predicted ν_e flux is listed in Table 5.14.

5.5.3 Electron Neutrino Flux

The error in the predicted ν_e flux was estimated to be 4.1% [56]. This error is dominated by a 20% production uncertainty in the K_L content of the secondary beam which produces 16% of the ν_e flux. The majority of the ν_e flux comes from $K^{\pm}_{e3}$ decays, which are well-constrained by the observed ν_μ spectrum from $K^{\pm}_{\mu 2}$ decays [56]. For a detailed description of the systematic uncertainties affecting the electron neutrino flux see section 4.3.

5.5.4 Ratio of Short to Long Events

The error in the ratio of short to long events is dominated by the uncertainty in the on-shell mixing angle from outside measurements. It has a large effect on the number of ν_e's because we extract the number of ν_e's as a fraction of short events, whereas the data and the Monte Carlo are normalized to a sample of long events with a well determined muon momentum. The $\sin^2\theta_W$ value in the on-shell renormalization scheme is 0.2232 ± 0.0018. This value is obtained using the world average value M_W measurement [70], the prediction from the measured M_Z, and the average of all LEP and SLD Z-pole measurements from

Energy (GeV)	$\Delta\nu_e$'s	Energy (GeV)	$\Delta\nu_e$'s
30 - 40	-0.31	120 - 135	-9.48
40 - 50	-2.16	135 - 150	-9.31
50 - 60	-4.13	150 - 175	-14.14
60 - 70	-3.02	175 - 200	-10.87
70 - 80	-4.84	200 - 250	-11.13
80 - 90	-5.89	250 - 300	-5.27
90 - 105	-8.89	300 - 600	-3.39
105 - 120	-9.60		

Table 5.15: Change in the number of electron neutrinos due to $+1\sigma$ change in the value of $\sin^2\theta_W$.

[71]. The M_Z extraction is corrected for the re-evaluation of α_{EM} by Swartz [72]. A top mass of 180 ± 12 GeV [73] and $60 < M_{Higgs} < 1000$ GeV are used to convert from the $\overline{MS}$ and M_Z schemes to the on-shell scheme used in this analysis. Table 5.15 lists the change in the ν_e flux in each of the energy bins studied due to the uncertainty in the measurement of $\sin^2\theta_W$.

5.5.5 NC/CC Shower Differences

This analysis assumes that NC and CC hadron showers have the same energy deposition profile and energy calibration in the calorimeter. It is possible for the calibration and η_3 to differ because the two shower types have different mean electromagnetic components. A Lund Monte Carlo simulation provided the conservative estimate that the energy calibration for CC and NC hadron showers differ by no more than 0.4%. The Lund generated showers were input into a GEANT simulation and tracked in the calorimeter. The energy deposition profile of hadron showers generated in NC and CC interactions was compared. The muon track pulse heights for the CC events were not included in the comparison. We used a Kolmogorov test to compare the shape of the NC and CC η distributions by calculating a probability PROB as a number between zero and one, which is a measure of the likelihood that the two distribution were the same. A PROB near one indicates very

similar histograms, and PROB near zero means that it is very unlikely that the two arose from the same parent distribution. For all energy bins studied the two shapes were found to be similar with probabilities greater than 0.9. As a further test, we used our ν_e analysis method to extract the number of "fake" ν_e events mixed in with NC events from the Monte Carlo. The "fake" ν_e events were generated by convoluting electromagnetic and CC GEANT generated showers appropriate for the ν_e energy spectrum. For all cases studied the extracted number of electron neutrinos was equal within errors with the input value. Consequently, we believe that any differences in the CC and NC shower energy deposition profiles does not affect the ν_e extraction. The η_3 distributions for NC and CC showers in some of the energy bins studied are plotted in Figure 5.16.

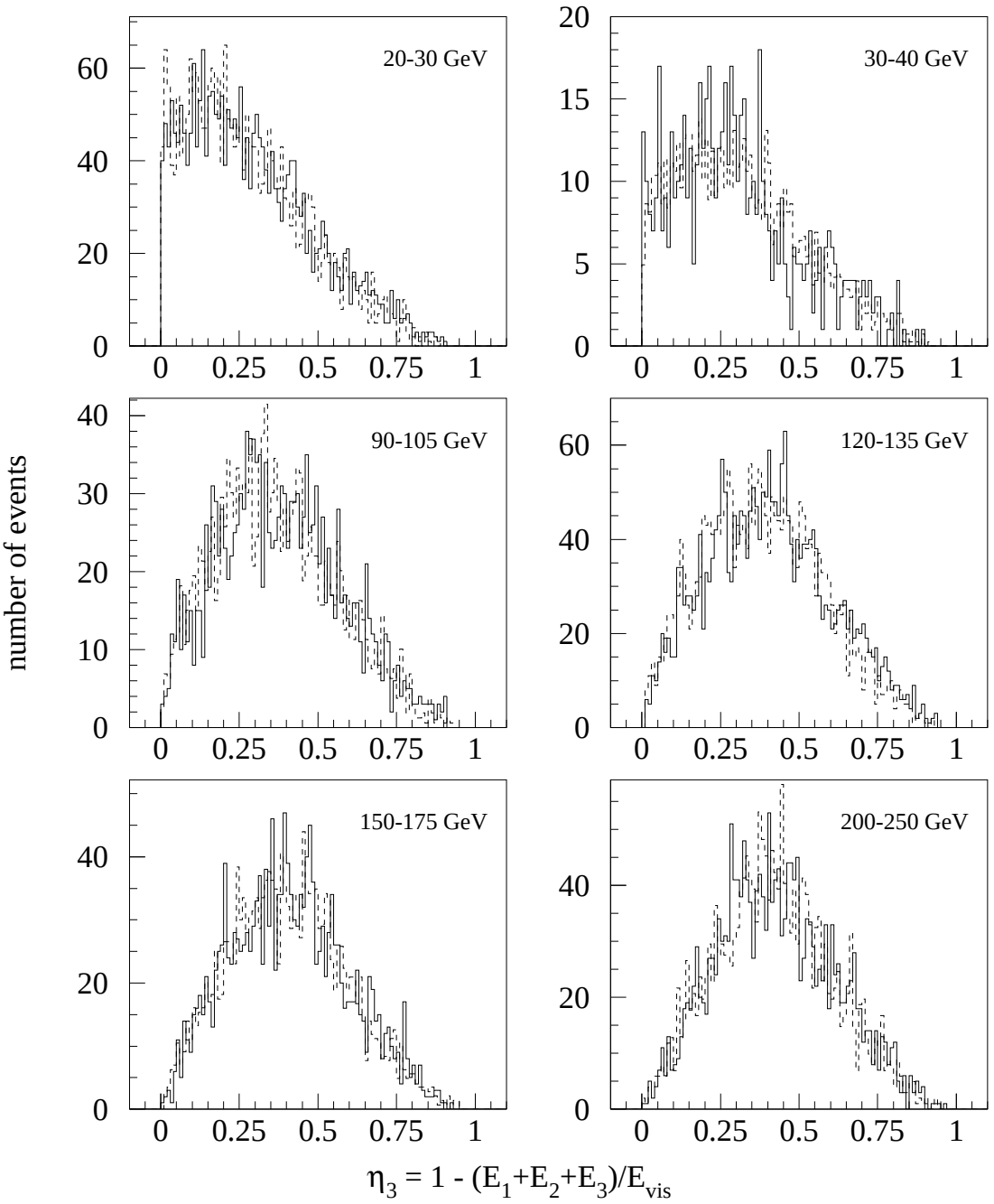

Figure 5.16: Comparison of the η distribution for Lund/GEANT simulated NC (solid line) and CC events (dashed line).

Chapter 6

Results

6.1 Oscillation Analysis

For this oscillation search we compare the absolute flux of ν_e's measured at the detector to the flux predicted by a detailed beamline simulation. Any excess could be interpreted as a signal of $\nu_\mu \to \nu_e$ oscillations. The ν_μ flux was determined directly from low hadron energy CC event sample, normalized to the total neutrino cross-section (see chapter 4). The same beamline simulation is used to tag the creation point of each simulated interacting ν_μ along the decay pipe. As it can be seen from Figure 6.1, the neutrino flight length distribution is almost flat over the length of the decay pipe.

The probability for a muon neutrino of energy E_ν having traveled a distance L to oscillate to an electron neutrino is given by:

$$P(\nu_\mu \to \nu_e) = \sin^2 2\theta \sin^2 \left(\frac{1.27 \Delta m^2 L}{E_\nu} \right) \tag{6.1}$$

If we take the average flight length to be on the order of 1 km, and using the neutrino average energy $\langle E \rangle \approx 160$ GeV, we find that

$$q = \frac{1.27L}{E} \sim \frac{1}{100}\,\mathrm{eV}^{-2} \tag{6.2}$$

The oscillation probability, given by Eq. 6.1, is maximal when Δm^2 is approximately equal to $1/q$. Therefore, we can expect the maximum sensitivity for this experiment to be at $\sim$ 100 eV^2.

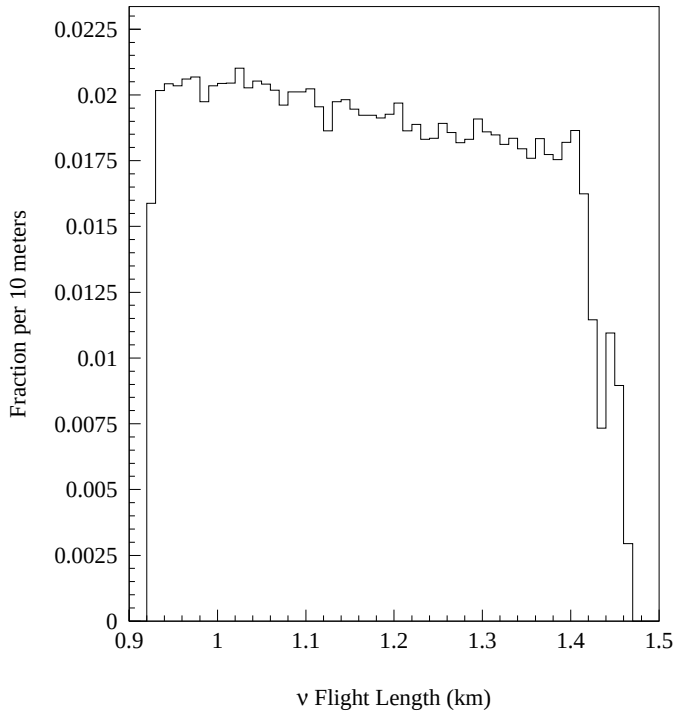

Figure 6.1: Neutrino flight length distribution. The mesons decay over a region between 1.5 and .9 km away from the detector.

The oscillation probability for all neutrinos is calculated by integrating Eq. (6.1) over the E_ν and flight length distributions for each species of neutrinos. To do this we use the beam Monte Carlo which also incorporates the detector acceptance. Given the flux of incoming muon neutrinos, for a given Δm^2 and $\sin^2 2\theta$ we can calculate the flux of electron neutrinos resulting from oscillations since the neutrino energy and the decay point are available for every generated event. The resulting fluxes are shown in Figure 6.2.

The number of ν_μ's at the detector predicted by the beam Monte Carlo is normalized to the number observed at the detector divided by $1 - P(\nu_\mu \to \nu_e)$ where $P(\nu_\mu \to \nu_e)$ is the oscillation probability determined from Equation 6.1. We assume CP invariance because we cannot distinguish between neutrinos and anti-neutrinos so $P(\nu_\mu \to \nu_e) = P(\overline{\nu}_\mu \to \overline{\nu}_e)$. The predicted electron neutrino flux is normalized to the *produced* number of ν_μ's. The ν_e

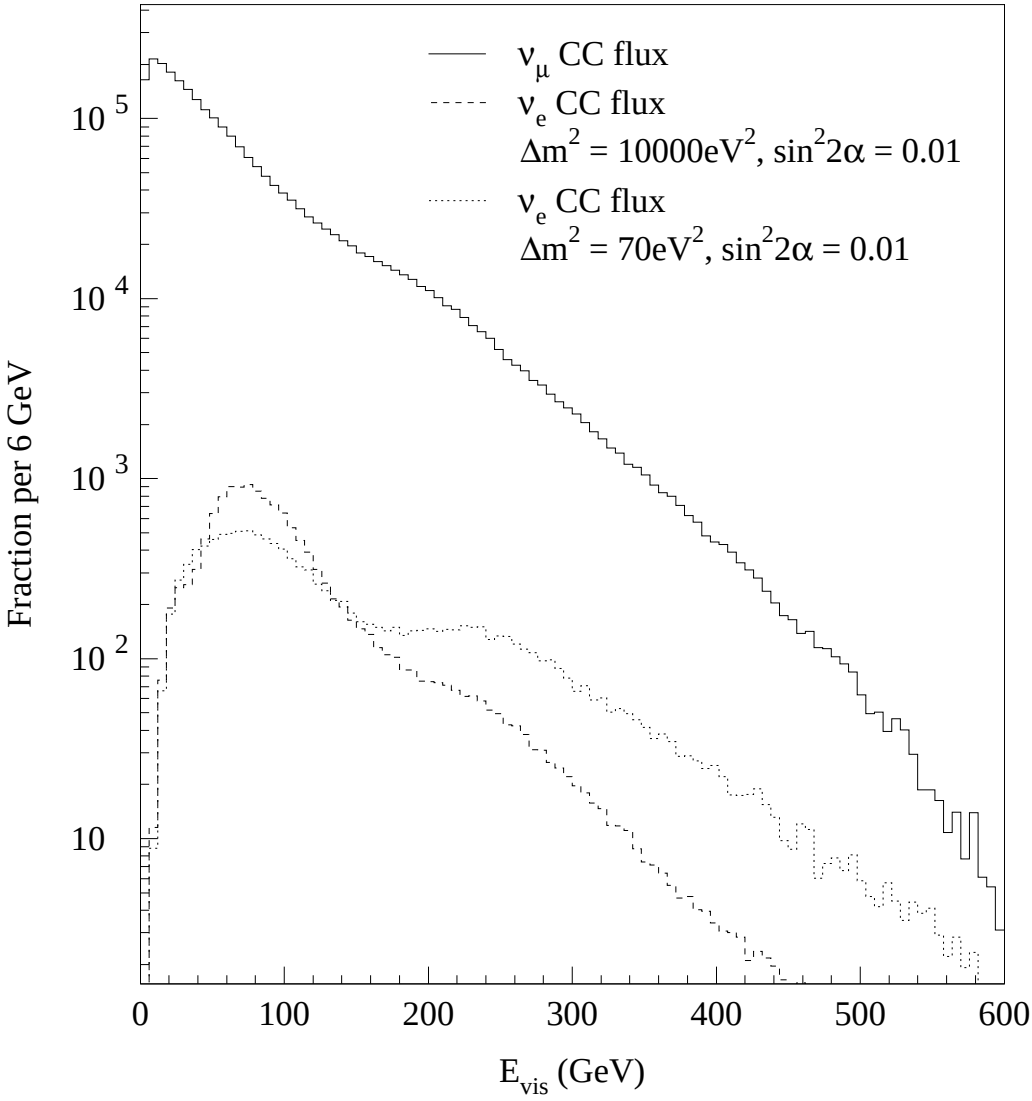

Figure 6.2: Monte Carlo prediction of the E_{vis} distribution for incoming ν_μ CC events (solid) and the resulting ν_e distributions assuming oscillations for $\Delta m^2 = 10000$ eV^2 and $\sin^2 2\alpha = 0.01$ (dashed line) and for $\Delta m^2 = 70$ eV^2 and $\sin^2 2\alpha = 0.01$ (dotted line).

flux from neutrino oscillations is calculated by multiplying the *produced* number of ν_μ's by $P(\nu_\mu \to \nu_e)$.

Figure 6.3 shows the measured number of ν_e's as a function of neutrino energy compared to the Monte Carlo prediction assuming no oscillations. The χ^2 for the no-oscillation case is 9.97/15 degrees of freedom which is consistent with the no oscillation hypothesis with a probability of 80%. The ν_e flux if we assume $\nu_\mu \to \nu_e$ oscillations with $\sin^2 2\alpha = 0.01$ and $\Delta m^2 = 2000$ eV^2 and $\Delta m^2 = 100$ eV^2 is also plotted and it is clearly highly unlikely.

To set the oscillation limits on the allowed $\Delta m^2 - \sin^2 2\alpha$ region at 90% confidence level we fit the data by forming a χ^2 which incorporates the Monte Carlo generated effect of oscillations, the basic error, and terms with coefficients accounting for systematic uncertainties. In order to include the systematic uncertainties with the correlation between the data points, one introduces a weighting factor, C_i, for each uncertainty that modulates the correlated changes in the data - Monte Carlo difference. The C_i factors are set up so that a value of 1 corresponds to a correlated one sigma shift in each of the data points. The contribution to the χ^2 from the given systematic uncertainty is then equal to C_i^2 divided by its standard error which is 1. Accordingly, we define the χ^2 function to be:

$$\chi^2 = \sum_{\text{energy bins}} \left(\frac{\text{Data}(E_{vis}) - \text{MC}(E_{vis}; \Delta m^2, \sin^2 2\theta, C_i)}{\sigma_{basic}} \right)^2 + \sum_{i \in \{\text{systematics}\}} C_i^2 \qquad (6.3)$$

where C_i are the coefficients of the nine systematic errors discussed in the previous section and listed in Table 6.1, and σ_{basic} is the basic error. This procedure can be shown to be equivalent to a full error matrix with all correlations between the set of data points taken into account.

At each Δm^2 we minimize this χ^2 letting all the C_i's float along with $\sin^2 2\alpha$. This assumes a linear effect in the number of ν_e's from oscillations with $\sin^2 2\alpha$ such that:

$$\Delta\nu_e^{\text{osc}}(E_\nu) = f_{\Delta m^2}(E_\nu) \sin^2 2\alpha \qquad (6.4)$$

where $f_{\Delta m^2}$ is the ν_e oscillation spectrum from oscillations at a given Δm^2 assuming full

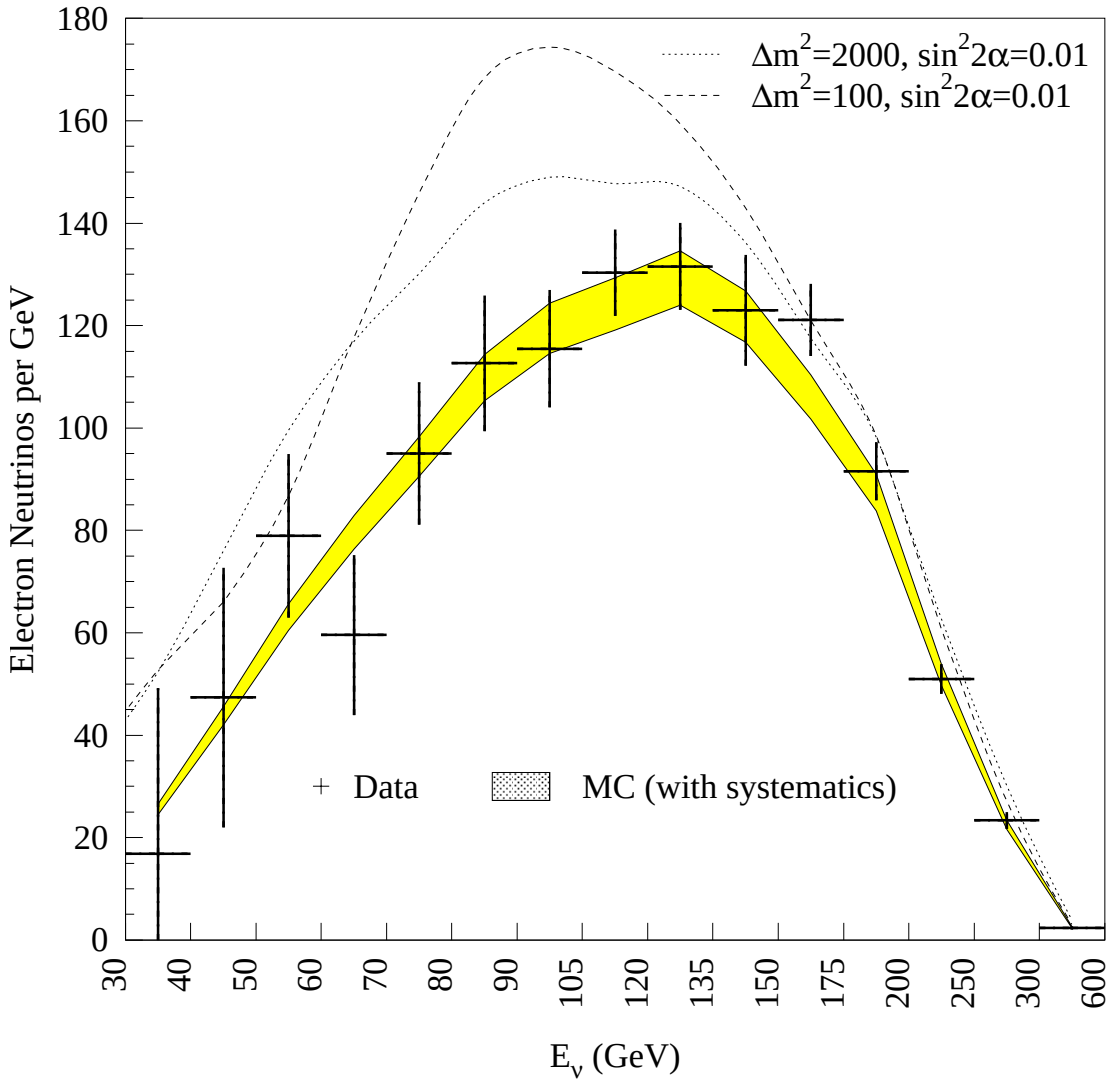

Figure 6.3: Comparison of the measured ν_e flux to the Monte Carlo prediction (filled band) assuming no oscillations. The dotted curve corresponds to $\nu_\mu \rightarrow \nu_e$ oscillations with $\Delta m^2 = 2000$ eV^2 and $\sin^2 2\alpha = 0.01$ and the dashed curve to $\Delta m^2 = 100$ eV^2 and $\sin^2 2\alpha = 0.01$

Energy (GeV)	(i)	(ii)	(iii)	(iv)	(v)	(vi)	(vii)	(viii)	(ix)
30 - 40	10.5	-0.7	16.8	0.9	9.9	-44.3	1.0	-0.1	-14.7
40 - 50	18.0	-6.5	6.5	1.4	7.4	-20.5	5.8	-11.9	9.6
50 - 60	26.0	-5.2	19.9	1.8	12.9	1.8	0.7	1.2	1.8
60 - 70	32.7	1.0	21.0	1.9	8.0	-4.6	7.9	20.0	2.5
70 - 80	38.7	-24.0	15.8	2.2	20.4	-10.7	10.0	36.5	4.3
80 - 90	45.0	-21.1	10.6	2.4	20.8	-3.3	3.5	-3.9	8.0
90 - 105	73.5	-28.6	21.6	2.9	39.7	13.0	10.5	41.4	-21.2
105 - 120	76.4	25.8	8.8	2.8	39.4	-8.3	12.2	-3.0	-18.5
120 - 135	79.5	19.2	24.3	1.8	44.3	-6.4	24.1	10.4	16.8
135 - 150	74.9	-1.6	-7.4	1.0	24.3	8.3	17.2	39.3	-87.5
150 - 175	108.7	52.8	-22.1	0.7	45.8	-6.0	40.9	-51.3	-72.8
175 - 200	89.6	94.4	-20.0	-0.5	35.4	2.5	24.3	-32.5	-8.9
200 - 250	106.3	129.8	-78.0	-2.0	44.0	-5.8	10.9	17.8	44.7
250 - 300	46.1	19.1	-50.1	-1.3	24.6	-1.1	0.6	-16.2	30.3
300 - 600	30.9	35.6	-42.6	-1.4	15.3	0.7	7.1	-22.2	55.0

Table 6.1: Systematic uncertainties in the number of ν_e events from (i) ν_e Monte Carlo prediction ($\pm 4.1\%$), (ii) normalization factor, (iii) e/π detector response (1.05 ± 0.015), (iv) charm mass (1.32 ± 0.24), (v) ν_e shower convolution, (vi) moun track correction, (vii) longitudinal vertex position, (viii) hadron energy calibration ($\pm 1\%$), and (ix) muon energy calibration ($\pm 1\%$).

mixing (*i.e.* $\sin^2 2\alpha = 1$). The dependence of $P(\nu_\mu \to \nu_e)$ with Δm^2 is shown in Figure 6.4. For low values of Δm^2 we are sensitive only to the low end of the energy spectrum. As the value of Δm^2 increases, so does the sensitivity at high neutrino energies.

Table 6.2 lists the best fit value of $\sin^2 2\alpha$ and the 1σ error from the fit for the 38 Δm^2 values used. The same values are shown in Figure 6.5, where we plot the best fit $\sin^2 2\alpha$ in units of σ as a function of Δm^2. It can be easily seen that although the the best fit $\sin^2 2\alpha$ values are slightly negative, they are well within the errors and consistent with zero.

The values of the systematic coefficients C_i are a measure of the information contained in the data on that particular systematic. A small value for any coefficient means that the data has no information on that particular systematic. An advantage of letting the systematic errors float in the fit is that it automatically includes the correlated error in $\sin^2 2\alpha$ from all the systematic errors which were assumed to be uncorrelated. Figure 6.6 shows the pull from the systematic errors listed in Table 6.1, where the pull is defined as the fit value of the C_i for the given systematic uncertainty. The major source of uncertainties in

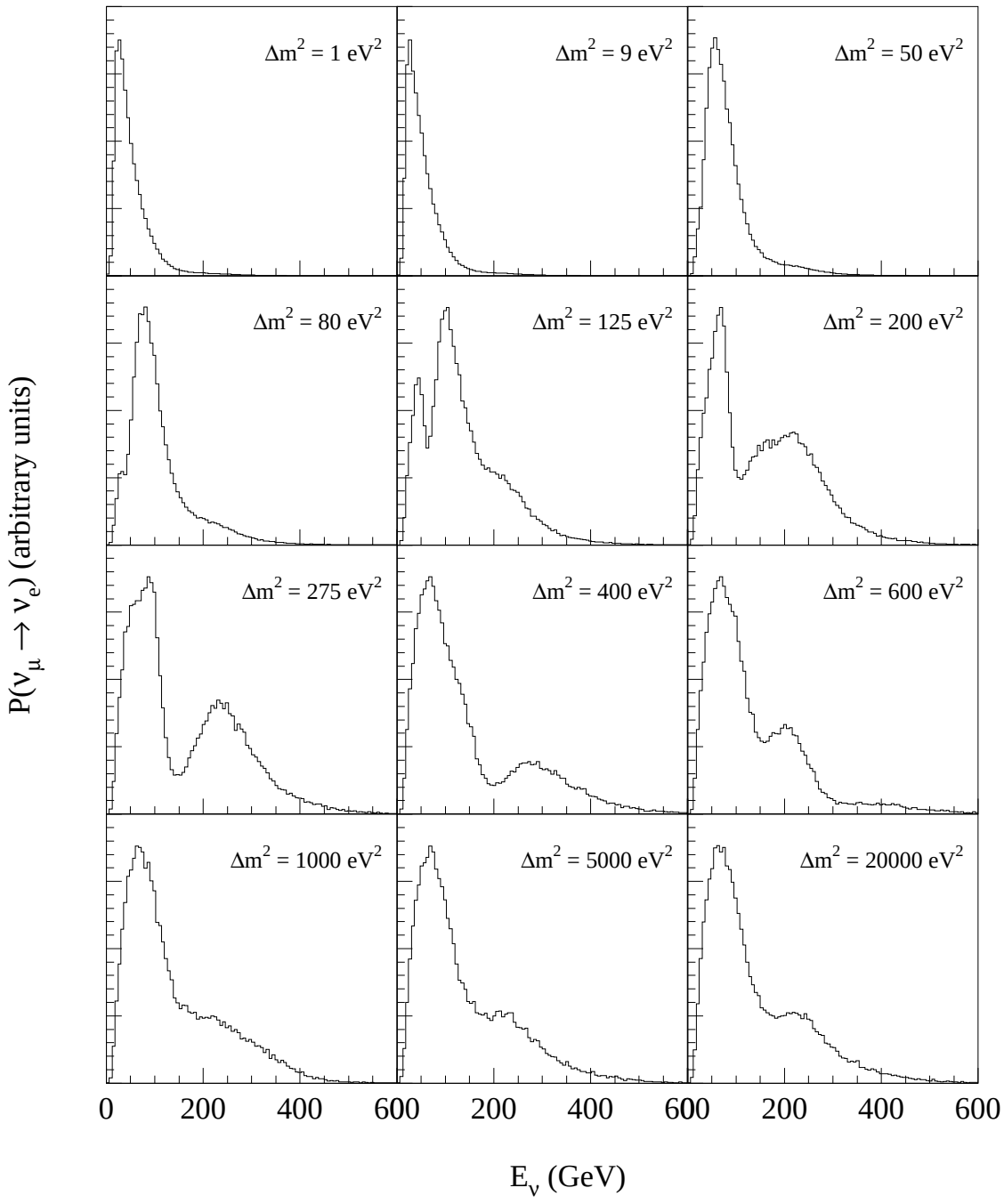

Figure 6.4: The oscillation probability for various Δm^2. For low Δm^2 values sensitivity comes only from the low energy end of the spectrum. As Δm^2 increases, so does the sensitivity to the high end of the energy spectrum.

Δm^2 (eV^2)	$\sin^2 2\alpha$	1σ	90% C.L.
1.0	-0.1741	1.6501	1.9380
2.0	-0.0501	0.4107	0.4756
3.0	-0.0153	0.1852	0.2218
4.0	-0.0112	0.1041	0.1220
5.0	-0.0051	0.0671	0.0808
7.0	-0.0036	0.0345	0.0405
9.0	-0.0021	0.0213	0.0252
10.0	-0.0023	0.0173	0.0198
20.0	-0.0004	0.0048	0.0057
30.0	-0.0003	0.0026	0.0030
40.0	-0.0002	0.0018	0.0022
50.0	-0.0002	0.0015	0.0017
60.0	-0.0002	0.0014	0.0015
70.0	-0.0002	0.0014	0.0015
80.0	-0.0003	0.0014	0.0015
90.0	-0.0003	0.0015	0.0016
100.0	-0.0002	0.0015	0.0018
125.0	0.0004	0.0018	0.0027
150.0	0.0005	0.0019	0.0028
175.0	0.0000	0.0016	0.0021
200.0	-0.0002	0.0014	0.0016
225.0	-0.0003	0.0013	0.0013
250.0	-0.0004	0.0012	0.0012
275.0	-0.0004	0.0012	0.0011
300.0	-0.0004	0.0012	0.0011
350.0	-0.0004	0.0012	0.0012
400.0	-0.0003	0.0013	0.0013
450.0	-0.0003	0.0015	0.0016
500.0	-0.0004	0.0016	0.0017
600.0	-0.0005	0.0019	0.0020
700.0	-0.0003	0.0018	0.0020
800.0	-0.0002	0.0018	0.0020
1000.0	-0.0004	0.0017	0.0018
1500.0	-0.0003	0.0017	0.0019
2000.0	-0.0004	0.0017	0.0019
5000.0	-0.0003	0.0018	0.0019
10000.0	-0.0004	0.0017	0.0018
20000.0	-0.0004	0.0017	0.0018

Table 6.2: The result for $\sin^2 2\alpha$ from the fit at each Δm^2 for $\nu_\mu \rightarrow \nu_e$ oscillations. The 90% confidence level limit is equal to the best fit $\sin^2 2\alpha + 1.28\sigma$.

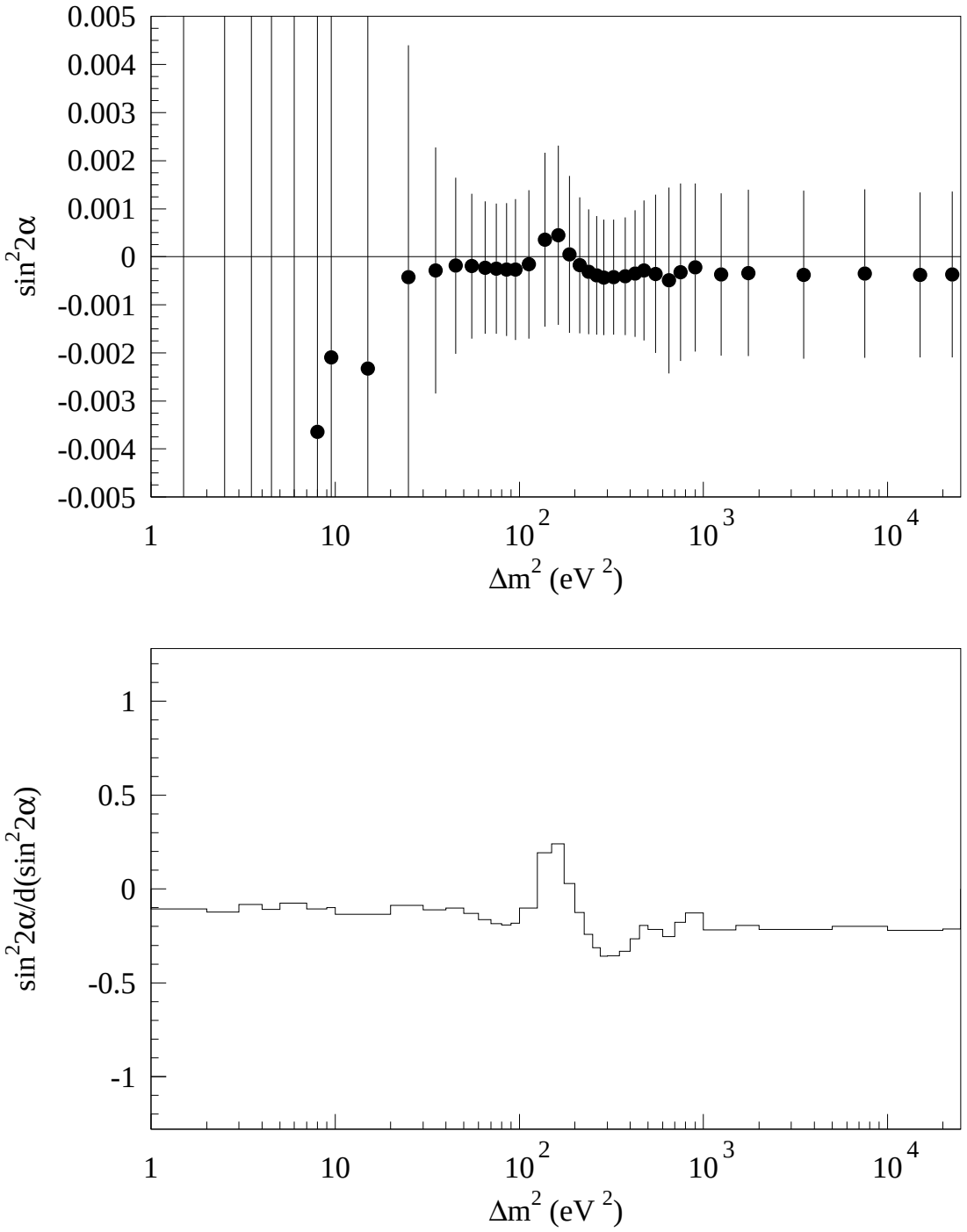

Figure 6.5: Best fit $\sin^2 2\alpha$ with 1σ errors as a function of Δm^2 (top), and $\sin^2 2\alpha$ divided by the 1σ error for each Δm^2 (bottom). The results are consistent with the no oscillation hypothesis ($\sin^2 2\alpha = 0$).

the extraction of $\sin^2 2\alpha$ is the basic error which is dominated by the statistical error. Other important uncertainties are: (i) the uncertainty in the incident flux of ν_e's at the detector. (ii) The uncertainty in the absolute energy calibration of the detector as measured by the muon and hadron scales. (iii) shower shape modeling of the ν_e sample. The effect these systematic errors have on $\sin^2 2\alpha$ is listed in Table 6.3. Figure 6.7 shows the correlation between each systematic error studied and $\sin^2 2\alpha$.

Source of Error	$\Delta m^2 = 2000$ eV^2	350 eV^2	70 eV^2
basic error	1.7×10^{-3}	1.2×10^{-3}	1.4×10^{-3}
shower shape modeling	3.5×10^{-4}	2.4×10^{-4}	1.5×10^{-4}
ν_e beam content	6.1×10^{-4}	4.1×10^{-4}	4.3×10^{-4}
norm. fraction	3.6×10^{-6}	4.3×10^{-6}	1.6×10^{-5}
e/π	8.2×10^{-6}	2.1×10^{-5}	1.1×10^{-5}
charm mass	1.4×10^{-7}	3.7×10^{-8}	3.4×10^{-7}
ν_e shower convolution	1.3×10^{-4}	8.4×10^{-5}	8.3×10^{-5}
μ correction	2.3×10^{-6}	8.9×10^{-7}	2.1×10^{-6}
long vertex position	2.1×10^{-5}	9.4×10^{-6}	1.5×10^{-5}
hadron scale	6.2×10^{-5}	1.9×10^{-5}	1.8×10^{-4}
muon scale	3.8×10^{-4}	3.0×10^{-4}	1.0×10^{-4}
total	1.8×10^{-3}	1.3×10^{-3}	1.5×10^{-3}

Table 6.3: The change in $\sin^2 2\alpha$ from a one sigma shift in the uncertainties studied. The row labeled "total" includes all the uncertainties added in quadrature.

Setting a 90% confidence upper limit means that for a given α_{true} we find a lower limit α_{limit} such that 90% of α_{exp} measurements lie above the this value of α_{limit}, where α_{exp} are the experimental measured values of α if we were to repeat the experiment many times. Consequently, we can say that the value of α_{true} lies below the 90% confidence limit α_{limit} with a 90% probability. In real life it is not possible (or at least not practical) to repeat an experiment like CCFR many times, so we have to determine this limit using statistical means.

In general, given a probability density function (p.d.f.) with known parameters we can predict the frequency with which a continuous variable lies in a given range. When we make a measurement we have the opposite problem of estimating the parameters of the

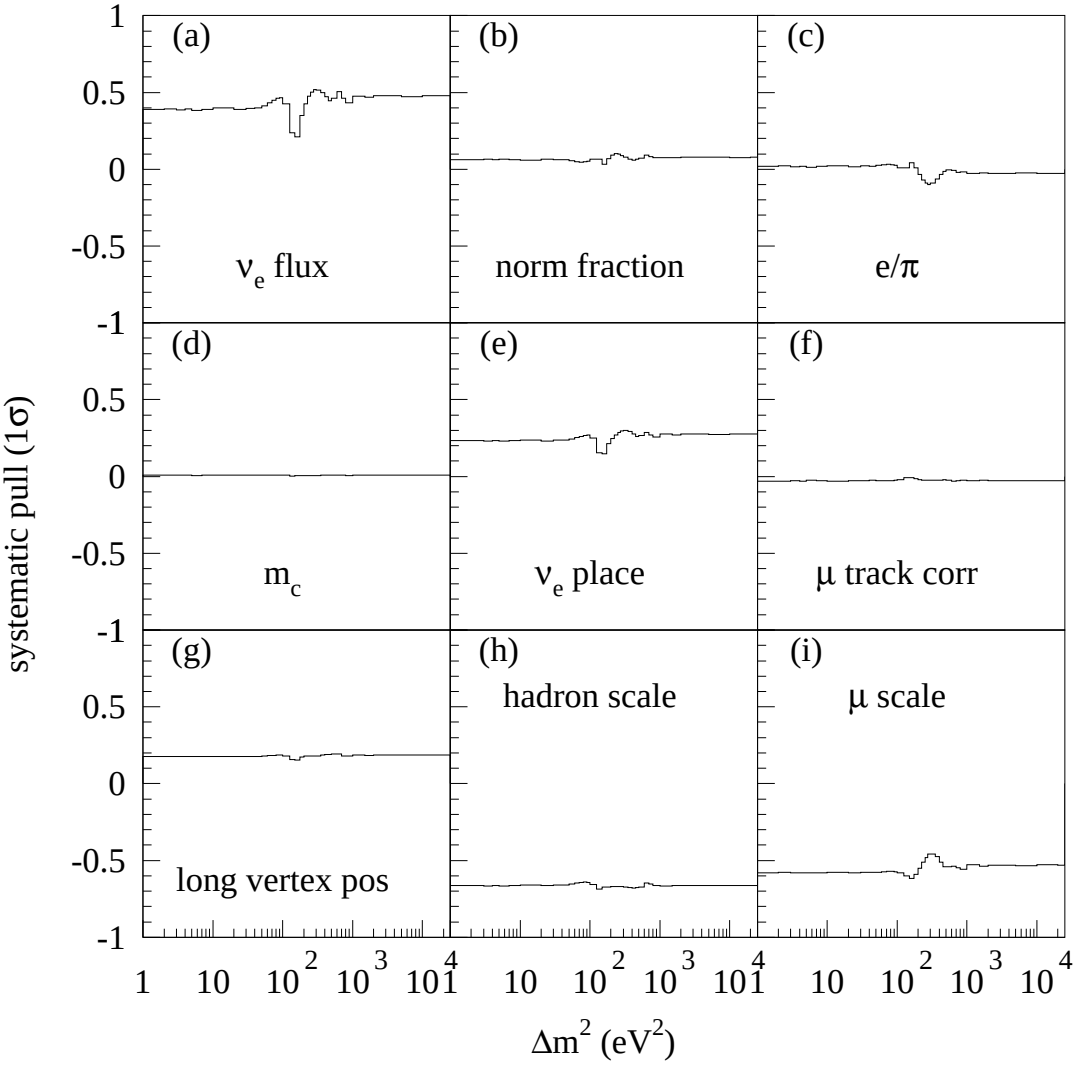

Figure 6.6: The effect of the systematics on the measurement of $\sin^2 2\alpha$ as a function of the mass squared difference Δm^2. (a) ν_e incident MC flux, (b) normalization fraction (c) the ratio of the hadron to the electromagnetic response of the detector, (d) charm mass, (e) ν_e CC shower simulation, (f) μ track correction, (g) longitudinal vertex position uncertainty, (h) hadron scale, and (i) μ scale.

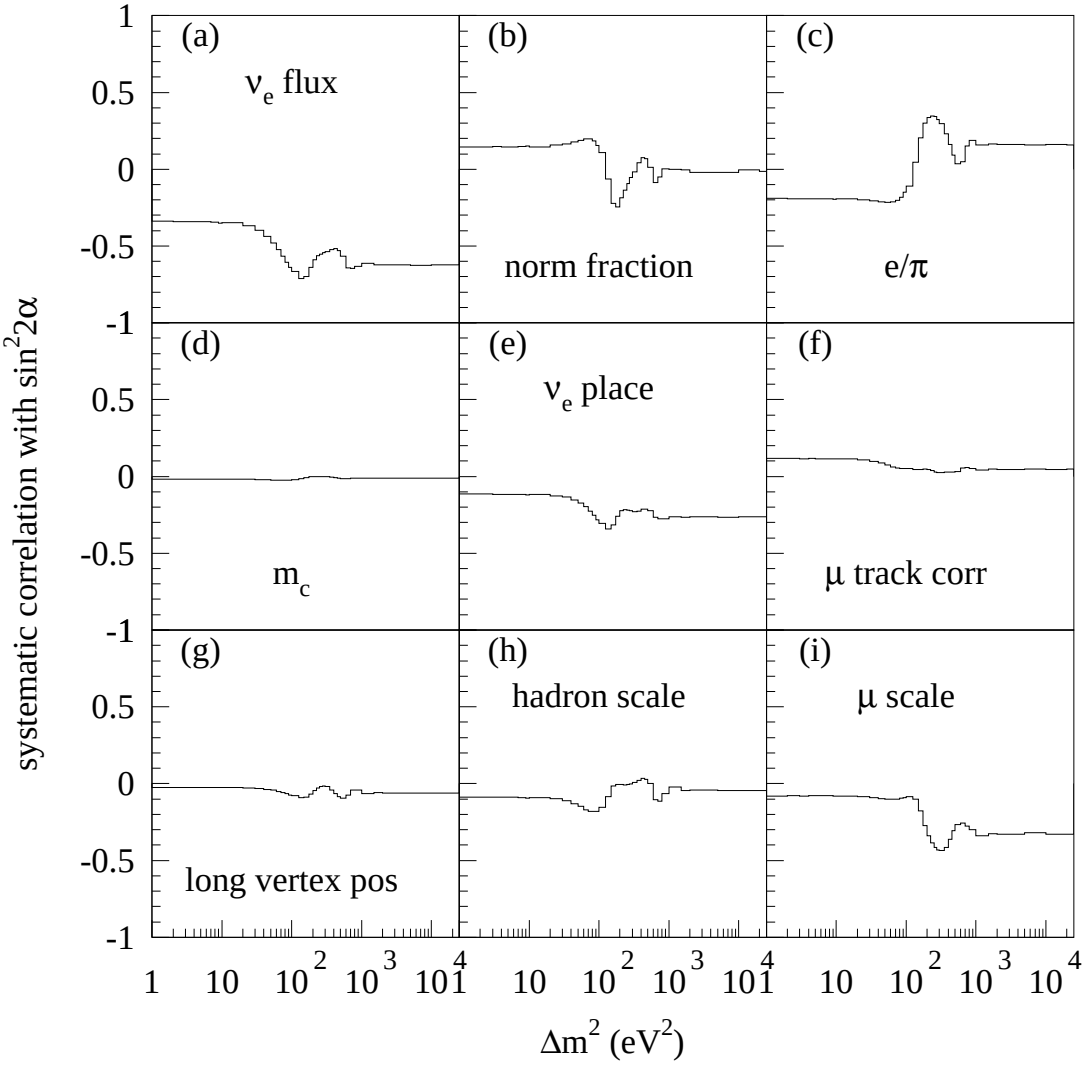

Figure 6.7: Systematic errors correlation to $\sin^2 2\alpha$ as a function of the mass squared difference Δm^2. (a) ν_e incident MC flux, (b) normalization fraction (c) the ratio of the hadron to the electromagnetic response of the detector, (d) charm mass, (e) ν_e CC shower simulation, (f) μ track correction, (g) longitudinal vertex position uncertainty, (h) hadron scale, and (i) μ scale.

p.d.f. from a set of actual observations. We define an *estimator* $\widehat{\alpha}$ as any function of the data, plus known constants, which does not depend upon any of the unknown parameters and whose value is intended as a meaningful guess of the unknown parameters.

The measurement of a physical constant α results in an estimator $\widehat{\alpha}$, together with some knowledge of the experimental error and therefore knowledge of the parametrized p.d.f. that allows us to state the probability with which repeated experiments would produce results in a given range. The measurement is made assuming that a "true answer" α exists and that the estimator $\widehat{\alpha}$ samples a distribution with p.d.f. $f(\widehat{\alpha};\alpha)$. Therefore we assume that for every value of α we can find two values $\gamma_1(\alpha,\epsilon)$ and $\gamma_2(\alpha,\epsilon)$ such that repeated experiments would produce results in the interval $\gamma_1 < \widehat{\alpha} < \gamma_2$ a fraction $1-\epsilon$ of the time, where

$$1-\epsilon = \int_{\gamma_1}^{\gamma_2} f(\widehat{\alpha};\alpha)\, d\widehat{\alpha} \tag{6.5}$$

where the choice of γ_1 and γ_2 can be made in an infinite number of ways. Our measurement does not permit us to comment about α itself, which in this language is a constant, instead we can say that with a given probability the unknown parameter lies between c_1 and c_2. The situation is shown in Fig. 6.8.

If the data are such that the distribution of the estimator satisfies the central limit theorem, the Gaussian distribution is the basis of the error analysis. The central limit theorem states that if a continuous random variable x is distributed according to *any* p.d.f with finite mean and variance, then the sample mean, $\overline{x}_n$, of n observations of x will have a p.d.f. that approaches a Gaussian as n increases. For this measurement, although we are not able to repeat it many times, we take the distribution of the estimator to be Gaussian. Consequently,

$$1-\epsilon = \int_{\widehat{\mu}-\delta}^{\widehat{\mu}+\delta} f(x;\widehat{\mu},\sigma^2)\, dx = \mathrm{erf}\left(\frac{\delta}{\sqrt{2}\sigma}\right), \tag{6.6}$$

where $\mathrm{erf}(x)$ is the error function available in computer math libraries and σ is the rms deviation, is the probability that the true value of μ will fall within $\pm\delta$ ($\delta > 0$) of the

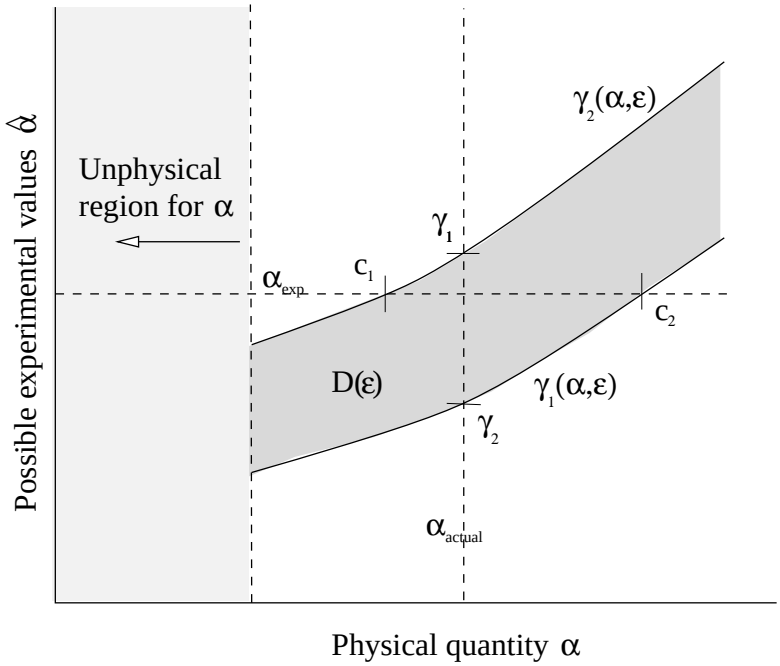

Figure 6.8: The confidence level method. The curves γ_1 and γ_2 represent fixed values for the experimental estimate $\widehat{\alpha}$. The domain $D(\epsilon)$ contains a fraction $1-\epsilon$ of the area under each of these functions.

measured $\widehat{\mu}$. This interval will cover μ in a fraction $1-\epsilon$ of all similar measurements. Confidence coefficients ϵ for frequently used choices of δ are given in Table 6.4. From these coefficients we can say that given a measurement $\widehat{\mu}$ the region of values above $\widehat{\mu}+1.64\sigma$ and below $\widehat{\mu}-1.64\sigma$ is excluded at 90% confidence level. For a one-sided (upper or lower) limit we exclude the region above $\widehat{\mu}+\delta$ (or below $\widehat{\mu}-\delta$). The values of the confidence coefficients ϵ for such limits are 1/2 of the values listed in Table 6.4. Since $\sin^2 2\alpha$ can have only positive physical values, being given a measurement of $\sin^2 2\alpha$ consistent with zero, then at 90% confidence level the region above $\sin^2 2\alpha + 1.28\sigma$ is excluded.

The question of how to extend the concept of confidence limit when a measurement is made near a physical boundary is one of the most divisive in high energy physics. If we assume, for simplicity, that α must be positive and that the true value is a small number close to the physical boundary, then a significant fraction of repetitions of the experiment

ϵ (%)	δ
20	1.28σ
10	1.64σ
5	1.96σ
2	2.33σ
1	2.58σ
0.1	3.29σ
0.01	3.89σ

Table 6.4: Area of the tails ϵ outside $\pm\delta$ from the mean of a Gaussian distribution.

would produce negative $\widehat{\alpha}$. The frequentist approach [74] states that there are several *ad hoc* ways to set confidence limits in such a case:

1. If $\widehat{\alpha}_{exp} > \gamma_1(0,\epsilon)$ then use c_2 for the upper limit, whether or not $\widehat{\alpha}_{exp} > 0$.

2. If $\widehat{\alpha}_{exp} < 0$ and $\widehat{\alpha}_{exp} < \gamma_1(0,\epsilon)$ use the c_2 corresponding to $\widehat{\alpha}_{exp} = 0$.

3. If c_1 is not defined, "lift up" $\widehat{\alpha}$ to $\gamma_2(0,\epsilon)$, where $c1 = 0$. Use the corresponding c_2 as the upper limit.

One should note that there are regions where more than one of the previous options can be used, with option 3 being the most conservative. For this analysis we choose to use option 1 since all measured values of $\sin^2 2\alpha$ lie above $\gamma_1(\epsilon)$, *i.e.* $\sin^2 2\alpha + 1.28\sigma > 0$.

Using the measured values of $\sin^2 2\alpha$ and the error, σ, for each Δm^2 value listed in Table 6.2 we can calculate for each Δm^2, at various confidence levels, the values of $sin^2 2\alpha$ excluded by this measurement. Since the real value of $\sin^2 2\alpha$ is always positive or zero, we set a one-sided upper limit. For example, at $\Delta m^2 = 100$ we measure $\sin^2 2\alpha$ to be -1.6×10^{-4} with an error $\sigma = 1.54\times10^{-3}$. Then, at 90% confidence level $\sin^2 2\alpha > 1.8\times10^{-3}$ is excluded by this measurement. Figure 6.9 shows the 90%, 95%, and 99% upper limits for this measurement. The region in the $(\sin^2 2\alpha, \Delta m^2)$ phase space to the right of the curve excludes neutrino oscillations at the corresponding confidence level.

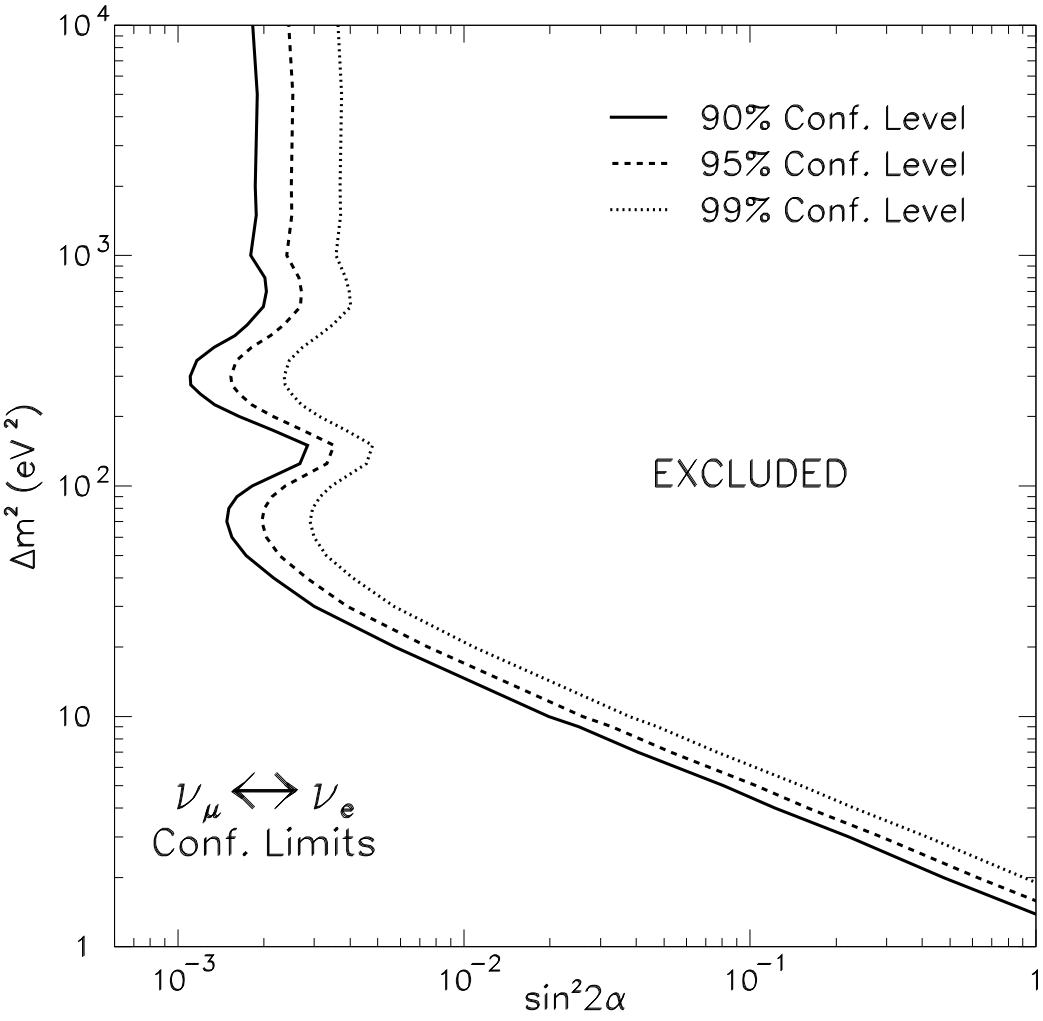

Figure 6.9: Upper limits for $\nu_\mu \leftrightarrow \nu_e$ oscillations from this analysis at 90%, 95% and 99% confidence level. The excluded region of $\sin^2 2\alpha$ and Δm^2 at a given confidence level is the area to the right of the corresponding curve.

6.2 Comparison to the R_{30} Method

The CCFR collaboration has previously reported a limit on $\nu_\mu \to \nu_e$ oscillations using the ratio of neutral to charged current events [18]. Accordingly we define R_{30} to be the number of "short" events divided by the number of "long" events [38, 56]. For this measurement "short" events were defined to be those events which deposit energy over an interval of 30 or fewer scintillation counters. This ratio is strongly dependent on the ratio of neutral to charged current events which is a function of the electroweak mixing angle, $\sin^2\theta_W$,

$$R_{\nu(\overline{\nu})} = \frac{\sigma_{NC}^{\nu(\overline{\nu})}}{\sigma_{CC}^{\nu(\overline{\nu})}} = \rho^2 \left[\frac{1}{2} - \sin^2\theta_W + \frac{5}{9}\sin^4\theta_W \left(1 + \frac{\sigma_{CC}^{\overline{\nu}(\nu)}}{\sigma_{CC}^{\nu(\overline{\nu})}} \right) \right] \tag{6.7}$$

Assuming the validity of the Standard Model, and using a value for $\sin^2\theta_W$ measured in other processes we can predict the ratio of neutral to charged current events in the CCFR detector, and thus R_{30}. The presence of ν_τ or additional ν_e in the neutrino beam would cause the measured R_{30} to be larger than the expected value because most charged current tau and electron neutrino interactions do not produce a muon in the final state and will thus appear in the "short" event sample. We attribute any deviation in our measured R_{30} from the predicted value to $\nu_\mu \to \nu_\tau$ or $\nu_\mu \to \nu_e$ oscillations. This technique, which has been discussed previously [75, 76, 77], assumes that only one of the two types of flavour oscillation contributes to a change in R_{30}, and is therefore conservative since both types of oscillations would increase the measured R_{30}.

We used a detailed Monte Carlo to relate a given $\nu_\mu \to \nu_\tau$ or $\nu_\mu \to \nu_e$ oscillation probability to the quantity R_{30}. A $\sin^2\theta_W$ value, from other experiments converted to the on-shell renormalization scheme, of 0.2232 ± 0.0018 is input to the Monte Carlo [18]. The other inputs to the Monte Carlo are parametrizations of the measured CCFR detector responses [51], nuclear structure functions [78], and relative neutrino beam fluxes extracted from the charged current data sample [55, 54]. The ν_e flux used is the beamline simulation prediction described in section 5.5.3 which is normalized by the observed ν_μ flux.

To simulate $\nu_{\tau,e}$ interactions in our detector we assumed the $\nu_{\tau,e}$ neutral current cross section is the same as for ν_μ interactions. The ν_τ charged current cross section was calculated including mass suppression terms. Following [79] we used the approximation that the structure functions $F_4 = 0$, and $xF_5 = 2xF_1$. The kinematic suppression for the massive tau production was also taken into account. The Monte Carlo program TAUOLA [80] was used to simulate tau decays.

For each Δm^2, the Monte Carlo prediction for $R_{30}(E_{cal}, \sin^2 2\alpha)$ is compared with $R_{30}(E_{cal})$ from the data, where E_{cal} is the energy deposited in the calorimeter in the first twenty counters following the event vertex. Figure 6.10 shows the R_{30} distribution as a function of E_{cal} for the data and for the Monte Carlo simulation. The detailed shape of $R_{30}(E_{cal})$ depends on many competing effects which are put in the Monte Carlo, but is dominated by the variation of short charged current events with E_{cal} and by the contribution from the predicted ν_e flux.

There are four major uncertainties in the comparison of $R_{30}(E_{cal})$ from the Monte Carlo to the data: the statistical error in the data, the uncertainty in the effective charm quark mass for charged current production, the uncertainty in the incident flux of ν_e's on the detector, and the uncertainty in the on-shell mixing angle from outside measurements. The charm mass error comes from the uncertainty in modeling the turn-on of the charm quark production cross section. The Monte Carlo uses a slow-rescaling model with the parameters extracted using events with two oppositely charged muons in this experiment [81]. Other sources of systematic uncertainties were also investigated [56].

The data are fit by forming a χ^2 which incorporates the Monte Carlo generated effects of oscillations, and statistical and systematic uncertainties. A best fit $\sin^2 2\alpha$ is determined for each Δm^2 by minimizing the χ^2 as a function of $\sin^2 2\alpha$ and the 33 systematic coefficients. The frequentist approach is used to set a 90% confidence upper limit for each Δm^2. The 90% confidence upper limits are plotted in Figure 6.11 for each case.

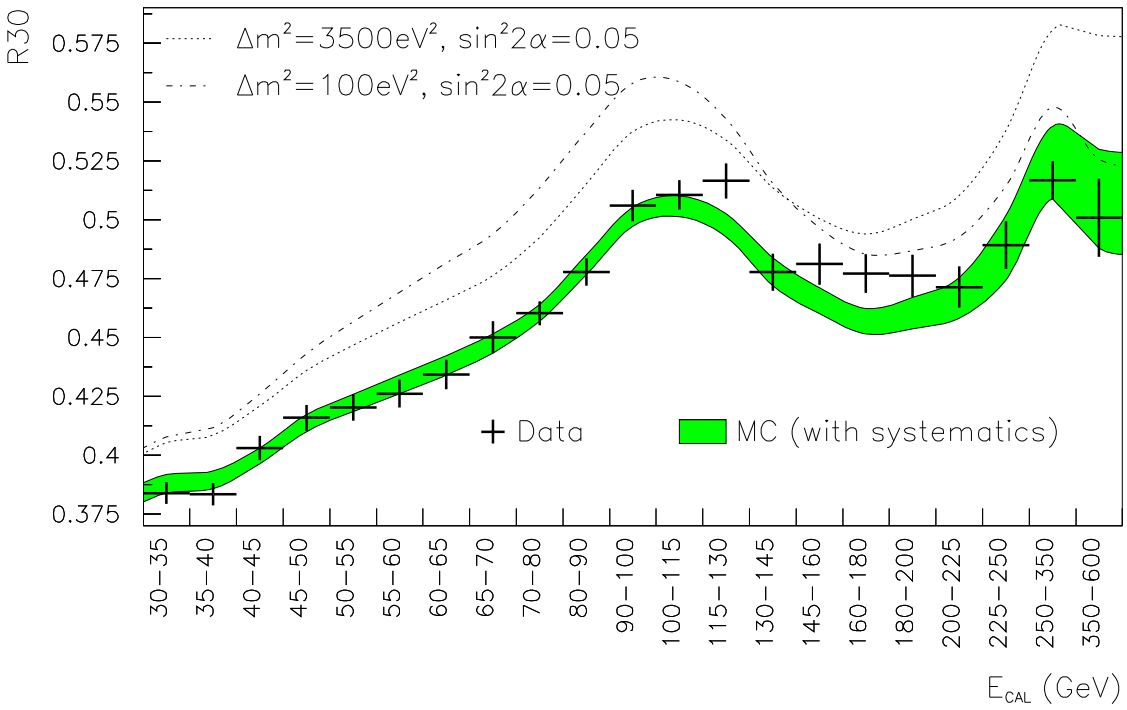

Figure 6.10: R_{30} as a function of E_{cal} for the data (points). The filled band shows the Monte Carlo prediction assuming no oscillations with 1σ systematic errors added in quadrature. Data points show statistical errors only. The dotted and dashed curves show the effect of $\nu_\mu \to \nu_e$ oscillations.

Figure 6.12 shows the 90% confidence upper limits using the R_{30} method and the η analysis method from $\nu_\mu \to \nu_e$ oscillations. The eta analysis method, which is the principal measurement of this thesis, shows an improvement in the limit for all Δm^2 values. The two methods use the same data sample; however, the η measurement uses additional information from the event shape. The two methods share the large systematic uncertainty from the predicted ν_e flux, but the R_{30} method has additional large contributions from external parameters such as the charm mass, and the world average value of the on-shell weak mixing angle, $\sin^2\theta_W$. The charm mass parameter comes into the charged current cross section, but does not affect the neutral current cross section, therefore the ratio R_{30} is affected by the uncertainty in this value. The η method is not sensitive to the charm mass

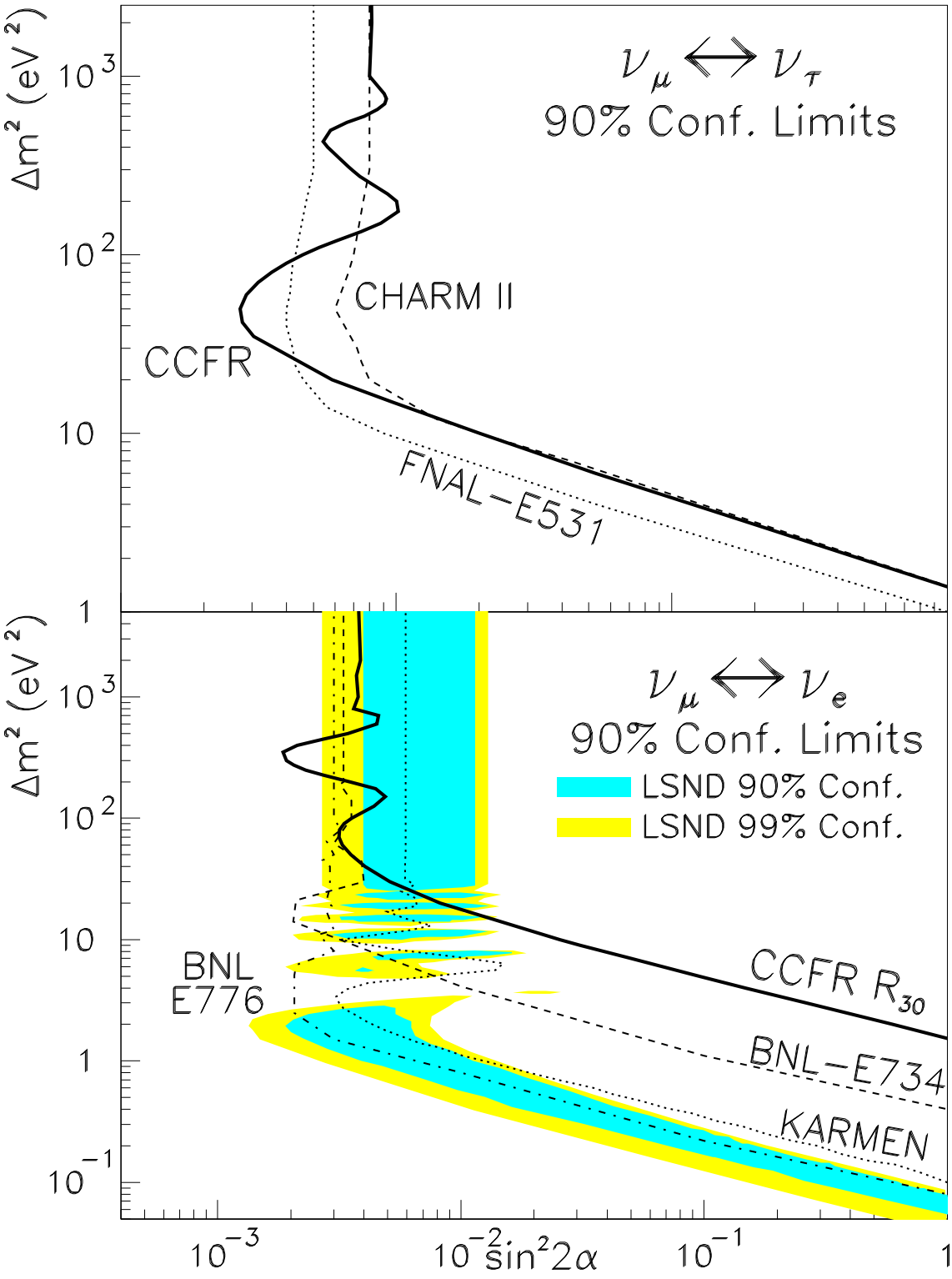

Figure 6.11: Excluded region of $\sin^2 2\alpha$ and Δm^2 for $\nu_\mu \to \nu_{\tau,e}$ oscillations from the R_{30} analysis at 90% confidence is shown as dark, solid curves.

since the charm mass comes into the cross section for both the predicted ν_e CC events, and the ν_μ CC events to which they are normalized. Consequently, the number of ν_e's predicted is not affected by this uncertainty. Additionally, the η measurement which can detect only CC ν_e interactions is independent of the weak mixing angle. Furthermore, the η method is far less dependent on Monte Carlo modeling. All these effects make the η method more sensitive in the search for neutrino oscillations than the R_{30} method and lead to the better limit shown in Figure 6.12.

6.3 Comparison with Other Oscillation Experiments

The results of this experiment can be compared with other oscillation experiments. Prior to the completion of this analysis, the regions in the $\Delta m^2 - \sin^2 2\alpha$ phase space for which $\nu_\mu(\overline{\nu}_\mu) \to \nu_e(\overline{\nu}_e)$ oscillations were excluded from accelerator experiments are shown in Figure 1.1. These experiments used either fine-grained calorimetric detectors (*e.g.* Brookhaven National Laboratory (BNL) E734, BNL E776), or fully active detectors (*e.g.* KARMEN, LSND), searching for quasielastic charged-current production of electrons. The LSND experiment, using a liquid scintillation neutrino target, has recently reported a signal consistent with $\overline{\nu}_\mu \to \overline{\nu}_e$ oscillations at a $\sin^2 2\alpha$ of $\sim 10^{-2}$ and a $\Delta m^2 \lesssim 1$ eV^2. The results presented in this thesis from data taken with a massive and relatively coarse-grained detector establishes such detectors as a viable option for future neutrino experiments searching for neutrino oscillations. The main advantages of this type of detector are increased interaction rate which will be particularly important in a low flux, long base line neutrino beam [82], and reduced cost.

Figure 6.13 shows the excluded region of $\sin^2 2\alpha$ and Δm^2 for $\nu_\mu \to \nu_e$ oscillations from this analysis at 90% confidence level compared with the previous measurements. Using the difference in the longitudinal shower energy deposition pattern of $\nu_e N$ versus $\nu_\mu N$ charged current interactions we set the most stringent limit to date for $\nu_\mu \to \nu_e$ interactions

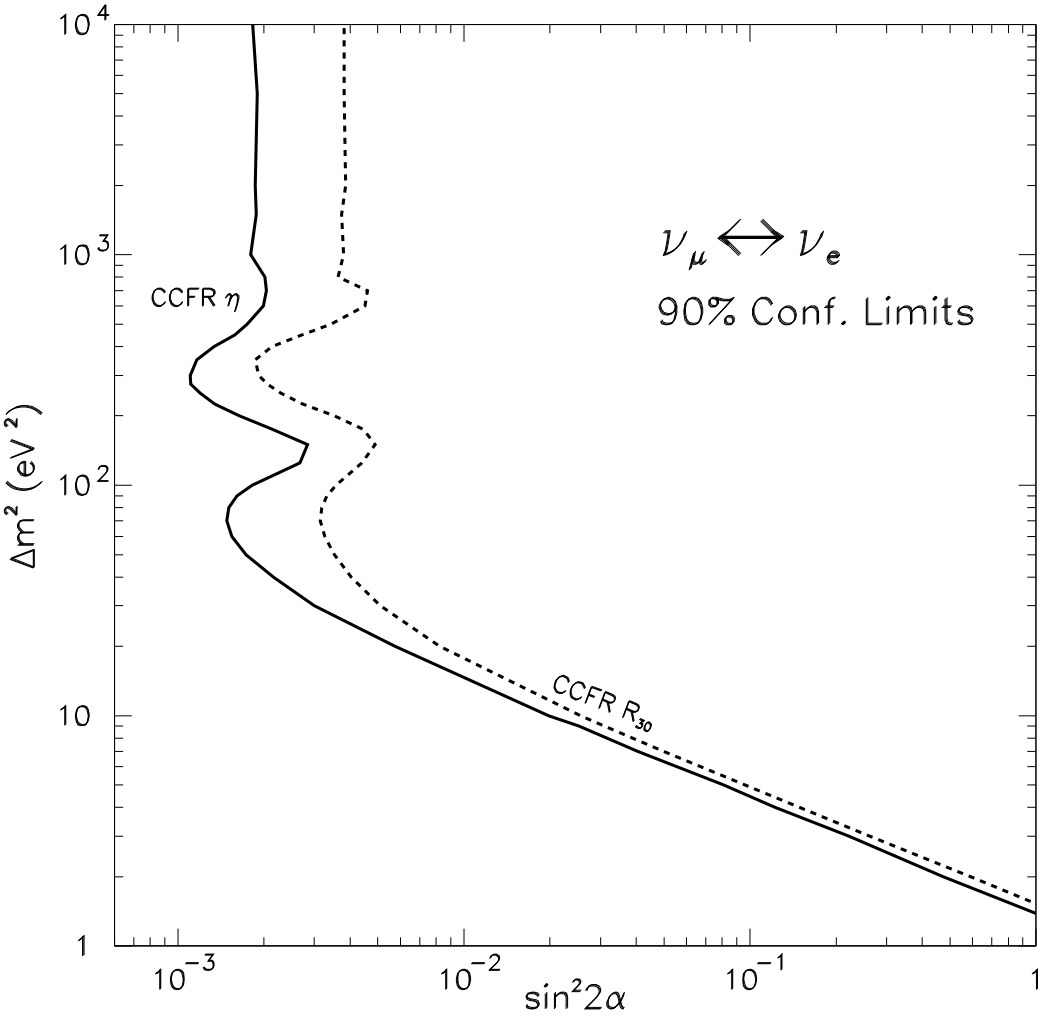

Figure 6.12: Comparison of $\nu_\mu \to \nu_e$ confidence upper limits using the R_{30} method (dashed) and the η analysis method (solid).

for $\Delta m^2 > 25$ eV^2. The CCFR experiment is also unique among the other accelerator experiments searching for neutrino oscillations because of our high energy neutrino beam averaging 160 GeV. All other experiments were performed with low energy (a few GeV) beams, and consequently probe lower values of Δm^2.

6.4 Tests of ν_μ/ν_e Universality

Universality is the hypothesis that the fermionic structures of the electromagnetic and weak interactions are the same for each generation. There are a number of theoretical models which predict violations of universality. Some examples are super-symmetry, theories with heavy leptons or heavy, neutral generation-changing gauge bosons, mirror-fermion models, and theories which view the observed fermion universality as accidental. Some of these lead to a violation of neutrino universality without a violation of charged-lepton universality. The experimental detection of a breakdown in universality might indicate the existence of one of these phenomena. Alternatively, confirmations of universality provide constraints on various theories.

Under the assumption that there are no oscillations, this data can also be used to test $\nu_\mu(\overline{\nu}_\mu) \leftrightarrow \nu_e(\overline{\nu}_e)$ universality by comparing the observed ν_e flux to that predicted by the Monte Carlo. For this comparison we determine the ratio of the cross sections averaged over our flux by comparing the predicted number of electron neutrinos with the number measured. The prediction assumes the same coupling and the same form for ν_e CC and ν_μ CC interactions. Deviations from this assumption would appear as a discrepancy in the number of ν_e's measured from that predicted.

To measure the ratio of the ν_μ to ν_e cross sections we fit the measured ν_e flux to the shape of the predicted ν_e flux allowing the normalization to float. The χ^2 function is given by:

$$\chi^2 = \sum_{\text{energy bins}} \left(\frac{MC(E_{vis}; C_i) - U \times \text{Data}(E_{vis})}{\sigma_{basic}} \right)^2 + \sum_{i \in \{\text{systematics}\}} C_i^2 \qquad (6.8)$$

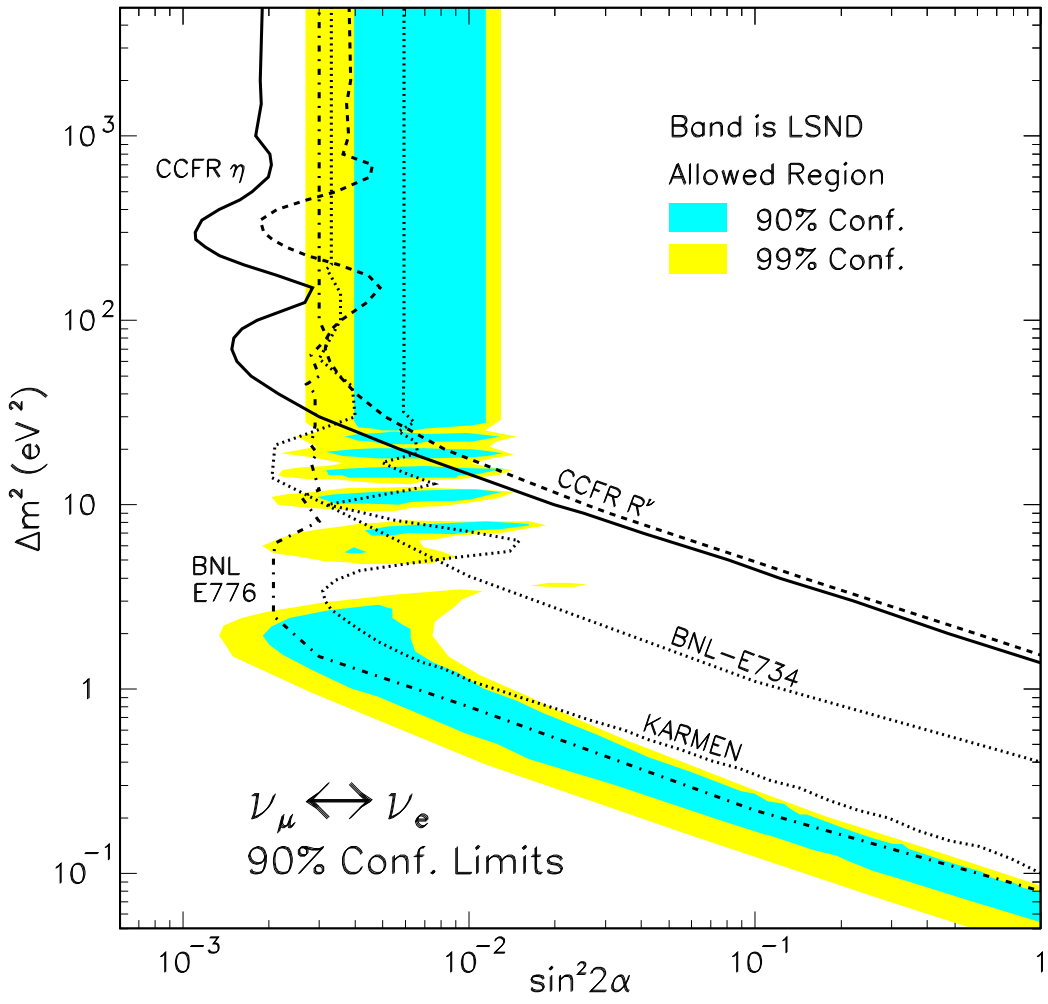

Figure 6.13: Excluded region of $\sin^2 2\alpha$ and Δm^2 for $\nu_\mu \to \nu_e$ oscillations from this analysis at 90% confidence is the area to the right of the dark, solid curve.

where C_i are the coefficients to the systematic error discussed previously, and σ_{basic} is the basic error. We minimize this χ^2 letting all the C_i float with the normalization factor, U, as the only free parameter. From this we measure

$$\frac{\sigma_{CC}(\nu_\mu)}{\sigma_{CC}(\nu_e)} = \frac{\nu_\mathrm{e} \text{ events predicted}}{\nu_\mathrm{e} \text{ events observed}} \frac{\int E_{\nu_e}(\nu_\mathrm{e} \text{ flux predicted})\, dE}{\int E_{\nu_e}(\nu_\mathrm{e} \text{ flux observed})\, dE} = 1.026 \pm 0.025(\mathrm{stat}) \pm 0.049(\mathrm{syst}) \tag{6.9}$$

The result is consistent with the universality hypothesis and is currently the most stringent test of universality at high space-like momentum transfer.

The same method was also used to study a linear dependence on energy of the ν_μ to ν_e cross section ratio by taking the normalization factor to be of the form

$$U_1 + U_2 \langle E \rangle_i, \tag{6.10}$$

where $\langle E \rangle_i$ is the flux weighted average for each of the 15 E_{vis} bins studied. From the fit we obtain $U_1 = 1.044 \pm 0.090$ and $U_2 = -0.0001 \pm 0.0004$. From this we conclude that the ratio of the cross sections doesn't exhibit any linear dependence on energy.

6.5 Summary and Conclusions

The next several years promise many new oscillation measurements and perhaps some of the hints for neutrino oscillations will either be confirmed or finally excluded beyond any doubt. Fermilab continues the rich tradition of neutrino experiments. The NuTeV experiment, a successor of the CCFR experiment, is currently taking data with a new sign selected quad triplet (SSQT) beam. One can reasonably expect an improvement of the current CCFR oscillation limits, since one of the main advantages of the SSQT beam is a reduced ν_e contamination, and also the detector is being continuously calibrated which will result in lower systematic uncertainties. The MINOS (Minn.-Ill.-ν-Osc.-Search.) long baseline experiment which will use the new Main Injector beam, is expected to run in approximately 2002. CHORUS and NOMAD are running at CERN looking for $\nu_\mu \to \nu_e$

oscillations at large $\Delta m^2 > 10$ eV^2 but small $\sin^2 2\alpha \approx 10^{-4} - 10^{-5}$. The Sudbury Neutrino Observatory (SNO) and Super-Kamiokande will continue the long history of Solar neutrino experiments. Figure 6.14 shows the region of phase space currently excluded, and expected future limits for $\nu_\mu \to \nu_e$ oscillations together with regions of possible hints of oscillations from atmospheric and solar neutrino experiments.

For the measurement presented in this thesis, we have used the difference in the longitudinal shower energy deposition pattern of $\nu_e N$ versus $\nu_\mu N$ interactions to search for $\nu_\mu \to \nu_e$ oscillations with a coarse-grained calorimetric detector. We see a result consistent with no neutrino oscillations and find 90% confidence level excluded regions in the $\sin^2 2\alpha - \Delta m^2$ phase space. This result is the most stringent limit to date for $\nu_\mu \to \nu_e$ oscillation for $\Delta m^2 > 25$ eV^2, which excludes the high Δm^2 region favoured by the LSND experiment. This measurement alone cannot constrain the possible values of a particular neutrino mass since oscillation measurements are sensitive only to mass differences. However, there are various constraints upon single masses from decay experiments and from cosmological arguments. It is in fact in the high Δm^2 region in which we might expect to find the effects of cosmologically useful neutrinos. As such, the region in the $\Delta m^2 - \sin^2 2\alpha$ plane for which neutrino oscillations are excluded by this measurement further constrains the mass of a massive neutrino with the possible implication that neutrinos alone cannot be responsible for the missing dark matter.

We also tested $\nu_\mu(\overline{\nu}_\mu) \leftrightarrow \nu_e(\overline{\nu}_e)$ universality and found the ratio of the ν_μ-to-ν_e cross-section to be 1.026 ± 0.055.

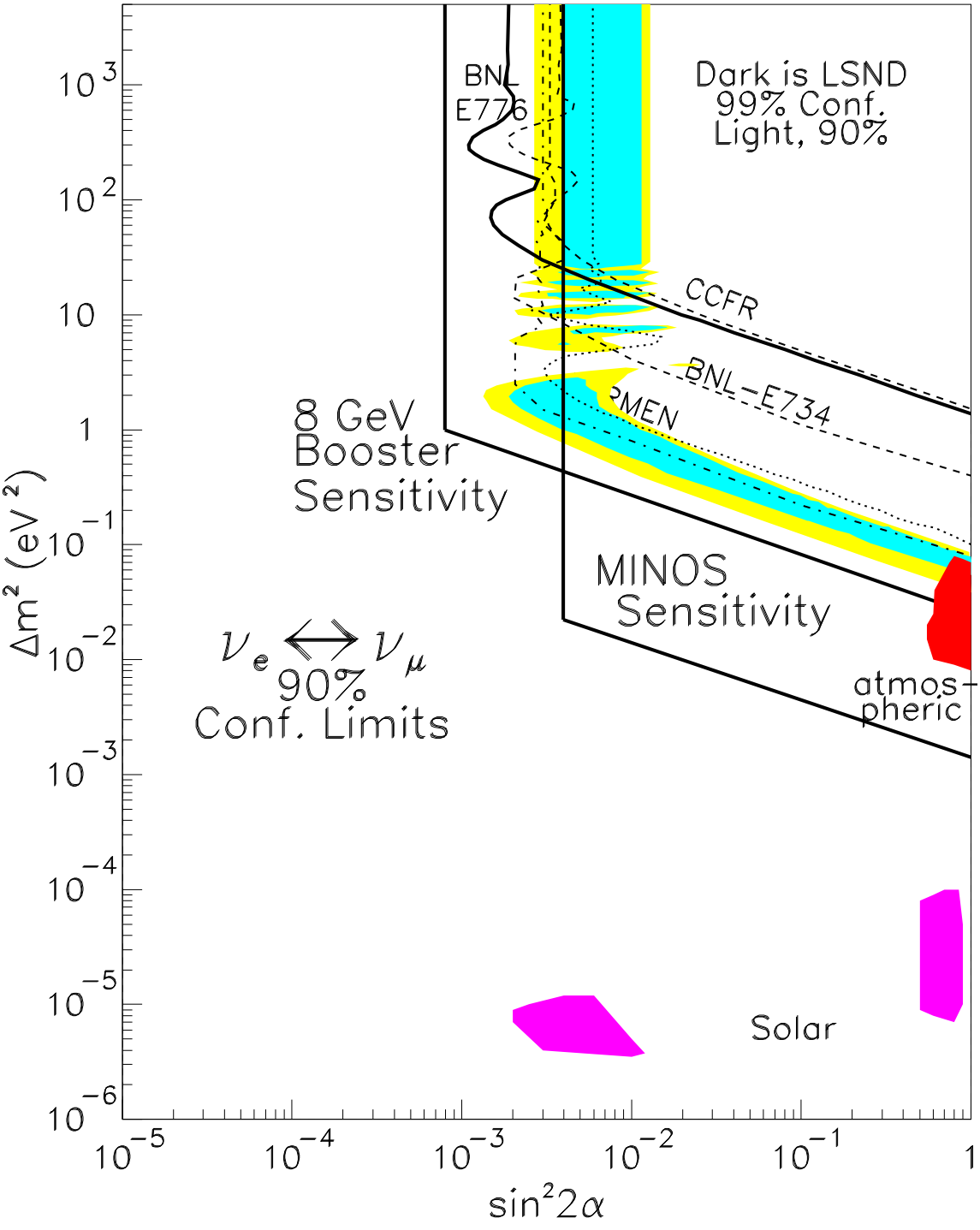

Figure 6.14: Current status of $\nu_\mu \to \nu_e$ oscillations and expected limits from future experiments.

Appendix A

The CCFR/NuTeV Collaboration

C.G. Arroyo, A.O. Bazarko, J. Conrad, J.H. Kim, B.J. King,
W.C. Lefmann, C. McNulty, S.R. Mishra, P.Z. Quintas, A. Romosan,
F.J. Sciulli, W.G. Seligman, M.H. Shaevitz, P. Spentzouris, E.G. Stern
Columbia University, New York, New York 10027

R.A. Johnson, M. Vakili
University of Cincinnati, Cincinnati, Ohio 45221

M.J. Oreglia, B.A. Schumm
University of Chicago, Chicago, Illinois 60637

R.H. Bernstein, K.S. McFarland, M.J. Lamm, W. Marsh
Fermilab, Batavia, Illinois 60510

T. Bolton, D. Naples
Kansas State University, Manhattan, Kansas 66506

H. Schellman
Northwestern University, Evanston, Illinois 60208

R.B. Drucker

University of Oregon, Eugene, Oregon 97403

A. Bodek, H.S. Budd, P. de Barbaro, D.A. Harris, W.K. Sakumoto, U.K. Yang

University of Rochester, Rochester, New York 14627

T. Kinnel, W.H. Smith

University of Wisconsin, Madison, Wisconsin 53706

Appendix B

Journal Publication

The existence of neutrino mass and mixing would have important implications for fundamental problems in both particle physics and cosmology. These include violation of lepton family number conservation, the mass of the universe, and the observed neutrino deficits from the sun and from atmospheric sources. Neutrino oscillations are a necessary consequence of non-zero neutrino mass and mixing since neutrinos are produced and detected in the form of weak-interaction eigenstates whereas their motion as they propagate from the point of production to their detection is dictated by the mass eigenstates [1]. In the two-generation formalism, the mixing probability is:

$$P(\nu_1 \to \nu_2) = \sin^2 2\alpha \sin^2 \left(\frac{1.27 \Delta m^2 L}{E_\nu} \right) \tag{B.1}$$

where Δm^2 is the mass squared difference of the mass eigenstates in eV^2, α is the mixing angle, E_ν is the incoming neutrino energy in GeV, and L is the distance between the point of creation and detection in km.

To date the best limits from accelerator experiments for $\nu_\mu \to \nu_e$ oscillations come from fine-grained calorimetric (e.g.: BNL-E734 [14], BNL-E776 [15]) or fully active detectors (e.g. KARMEN [16], LSND [17]) searching for quasi-elastic charged current production of electrons. The LSND experiment, using a liquid scintillator neutrino target, has reported a signal consistent with $\overline{\nu}_\mu \to \overline{\nu}_e$ oscillations at a $\sin^2 2\alpha \approx 10^{-2}$ and $\Delta m^2 \gtrsim 1$ eV^2 [17].

[1] Published in Phys. Rev. Lett., **78**, 2912 (1997)

The CCFR collaboration has previously reported a limit on $\nu_\mu \to \nu_e$ oscillations using the ratio of neutral to charged current neutrino events comparable in sensitivity to the above mentioned limits [18].

In this report we present new limits on $\nu_\mu \to \nu_e$ oscillations based on the statistical separation of $\nu_e N$ charged current interactions.

The CCFR detector [51, 52] consists of an 18 m long, 690 ton total absorption target calorimeter with a mean density of 4.2g/cm^3, followed by a 10 m long iron toroidal spectrometer. The target consists of 168 steel plates, each 3m $\times$ 3m $\times$ 5.15cm, instrumented with liquid scintillation counters placed every two steel plates and drift chambers spaced every four plates. The separation between scintillation counters corresponds to 6 radiation lengths, and the ratio of electromagnetic to hadronic response of the calorimeter is 1.05. The toroid spectrometer is not directly used in this analysis which is based on the shower profiles in the target-calorimeter.

The Fermilab Tevatron Quadrupole Triplet neutrino beam is a high-intensity, non-sign-selected wideband beam with a $\nu : \overline{\nu}$ flux ratio of about 2.5 : 1 and usable neutrino energies up to 600 GeV. The production target is located 1.4 km upstream of the neutrino detector and is followed by a 0.5 km decay region. The resulting neutrino energy spectra for ν_μ, $\overline{\nu}_\mu$, ν_e, and $\overline{\nu}_e$ induced events are shown in Figure B.1. The beam contains a 2.3% fraction of electron neutrinos, 82% of which are produced from $K^\pm \to \pi^0 e^\pm \overset{(-)}{\nu}_e$.

The neutrino interactions observed in the detector can be divided into three classes depending on the type of the incoming neutrino and on the interaction type:

1. $\nu_\mu N \to \mu^- X$ (ν_μ charged current (CC) events).

2. $\nu_{\mu,e} N \to \nu_{\mu,e} X$ ($\nu_{\mu,e}$ neutral current (NC) events).

3. $\nu_e N \to eX$ (ν_e CC events).

All three types of neutrino interactions initiate a cascade of hadrons that is registered

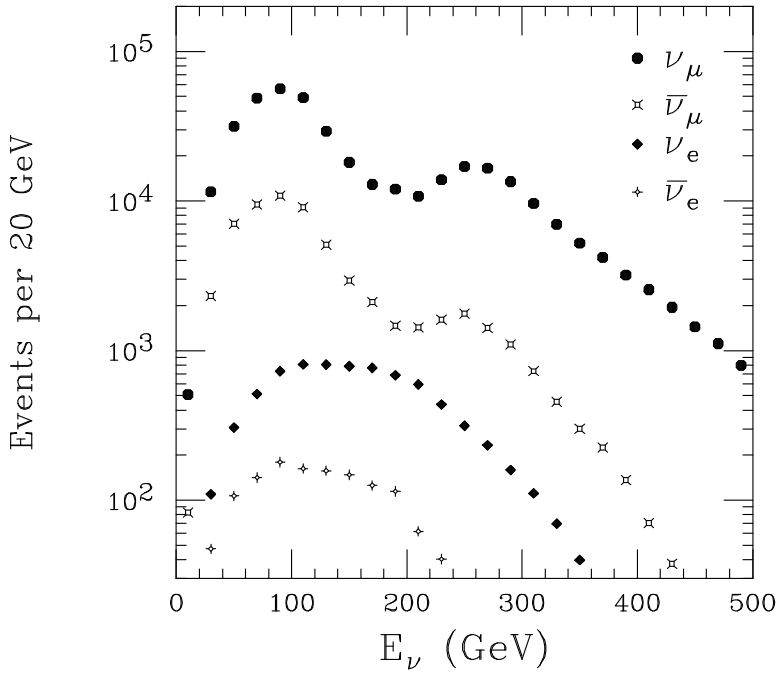

Figure B.1: Neutrino energy spectra for ν_μ, $\overline{\nu}_\mu$, ν_e, and $\overline{\nu}_e$ at the CCFR detector for the FNAL wideband neutrino beam (Monte Carlo based on relative ν_μ and $\overline{\nu}_\mu$ fluxes).

by the drift chambers and scintillation counters. The ν_μ CC events are characterized by the presence of a muon produced in the final state which penetrates beyond the end of the hadron shower, depositing energy characteristic of a minimum ionizing particle [51] in a large number of consecutive scintillation counters. Conversely, the electron produced in a ν_e CC event deposits energy in a few counters immediately downstream of the interaction vertex which changes the energy deposition profile of the shower. The electromagnetic shower is typically much shorter than the hadron shower and the two cannot be separated for a ν_e CC event.

In this analysis four experimental quantities are calculated for each event: the length, the transverse vertex position, the visible energy and the shower energy deposition profile. The event length is determined to be the number of scintillation counters spanned from the event vertex to the last counter with a minimum-ionizing pulse height. The mean position of the hits in the drift chamber immediately downstream of the interaction vertex

determines the transverse vertex position. The visible energy in the calorimeter, E_{vis} is obtained by summing the energy deposited in the scintillation counters from the interaction vertex to five counters beyond the end of the shower. The shower energy deposition profile is characterized by the ratio of the sum of the energy deposited in the first three scintillation counters to the total visible energy. Accordingly, we define

$$\eta_3 = 1 - \frac{E_1 + E_2 + E_3}{E_{vis}} \tag{B.2}$$

where E_i is the energy deposited in the i^{th} scintillation counter downstream of the interaction place.

The most downstream counter with energy deposited from the products of the neutrino interaction (CEXIT) occurs at the end of the hadron shower for ν_μ NC and ν_e CC events but is determined by the muon track for most ν_μ CC events. We isolate the events without a muon track by requiring CEXIT to be no more than 10 counters downstream from the end of the hadron shower. We parametrize the event length which contains 99% of such events as:

$$L_{NC} = 4. + 3.81 \times \log(E_{vis}) \tag{B.3}$$

In order to measure the number of ν_e CC events we divide the neutrino events into two classes: "short" if they deposit energy over an interval shorter than L_{NC}, and "long" otherwise. The long events consist almost exclusively of class 1 events, while the short ones are a mixture of class 2, class 3 and class 1 events with a low energy muon which cannot be separated on an event-by-event basis.

Based on Lund studies, we assume that for the same shower energy, the hadron showers produced in NC and CC interactions are the same. Any difference in the shower energy deposition profile of long and short events is attributed to the presence of ν_e CC interactions in the short sample. To compare directly the long and short events a muon track from the data was added to the short events to compensate for the absence of a muon in NC events.

The fraction, f, of ν_μ CC events with a low energy muon contained in the short sample which now have two muon tracks was estimated from a detailed Monte Carlo of the experiment in the range of 20%. A simulated sample of such events was obtained by choosing long events with the appropriate energy distribution from the data to which a second short muon track was added in software. The length of the short track and the angular distribution were obtained from a Monte Carlo of ν_μ CC events.

To simulate ν_e interactions in our detector we assume $\nu_\mu - \nu_e$ universality. The electron neutrino showers were generated by adding a GEANT [69] generated electromagnetic shower of the appropriate energy to events in the long data sample. The energy distribution of the electron neutrinos and the fractional energy transfer y were generated using a detailed Monte Carlo simulation of the experiment. Since the hadron showers in the long sample already have a muon track, the ν_e sample can be compared directly with the short and long events.

The long and short η_3 distributions were further corrected by subtracting the contamination due to cosmic ray events. The cosmic ray background was estimated from the event sample collected during a beam off gate using an identical analysis procedure as for the data gates. Additionally, the η_3 distribution of short ν_μ CC events, normalized to the predicted fraction f, was subtracted from the short event sample. The η_3 distributions for short, long, and ν_e events for various energy bins are shown in Figure B.2.

For this oscillation search we measure the absolute flux of ν_e's at the detector and compare it to the flux predicted by a detailed beamline simulation [56]. Any excess could be interpreted as a signal of $\nu_\mu \to \nu_e$ oscillations. The ν_μ flux was determined directly from the low hadron energy CC event sample, normalized to the total neutrino cross-section [55]. The same beamline simulation is used to tag the creation point of each simulated ν_μ along the decay pipe, and give the number of predicted ν_μ's at the detector normalized to the number observed at the detector divided by $1 - P(\nu_\mu \to \nu_e)$. $P(\nu_\mu \to \nu_e) = P(\overline{\nu}_\mu \to \overline{\nu}_e)$

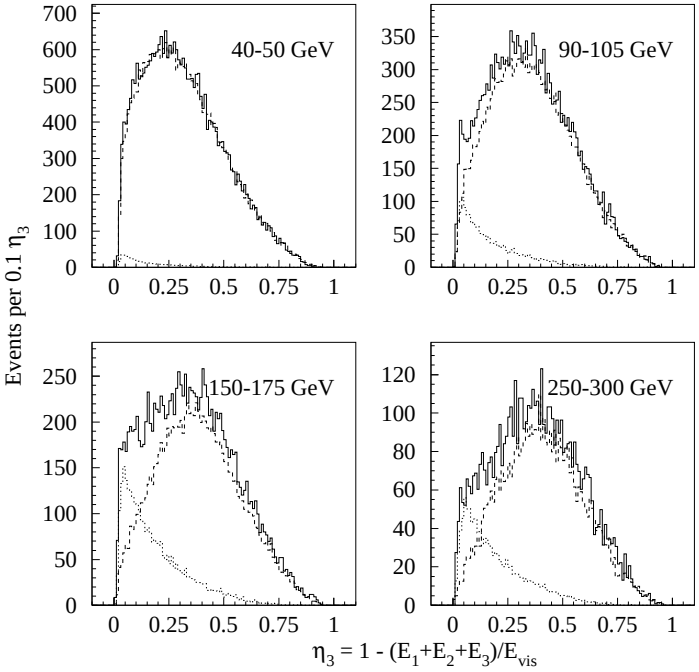

Figure B.2: Eta distributions for short (solid line), long (dashed line) and ν_e (dotted line) events in four of the energy bins studied. The ν_e and long distributions are normalized to the respective number of events predicted by the fit.

is the oscillation probability determined from eq. (B.1), assuming CP invariance. The predicted electron neutrino flux is normalized to the *produced* number of ν_μ's. The ν_e flux from neutrino oscillations is calculated by multiplying the *produced* number of ν_μ's by $P(\nu_\mu \rightarrow \nu_e)$.

The events selected are required to deposit a minimum of 30 GeV in the target calorimeter to ensure complete efficiency of the energy deposition trigger. Additionally, we require the event vertex to be more than 5 counters from the upstream end of the target and five counters plus the separation length from the downstream end and less than 50" from the detector centre-line. The resulting data sample consists of 632338 long events and 291354 short ones.

To extract the number of ν_e CC events in each of 15 E_{vis} bins, we fit the corrected shape of the observed η_3 distribution for the short sample to a combination of ν_μ CC and ν_e CC

distributions with appropriate muon additions:

$$\nu_\mu \mathrm{NC}(+\mu) = \alpha\, \nu_\mu \mathrm{CC} + \beta\, \nu_\mathrm{e} \mathrm{CC}(+\mu) \tag{B.4}$$

The χ^2 of the fit in each of the 15 E_{vis} bins ranges from 33.2 to 77.7 for 41 degrees of freedom (DoF) with a mean value of 48.4. Figure B.3 shows that the measured number of ν_e CC's agrees with the Monte Carlo prediction in each energy bin. The χ^2 value with a no-oscillations assumption is 9.97/15 DoF.

The major sources of uncertainties in the comparison of the electron flux extracted from the data to that predicted by the Monte Carlo are: (i) The statistical error from the fit in the extraction of the ν_e flux. (ii) The error in the shower shape modeling, estimated by extracting the ν_e flux using two definitions of η. Analogous to the definition of η_3 given in eq. (B.2), we define η_4 to be the ratio of the sum of the energy deposited outside the first four scintillation counters to the total visible energy. If the modeling of the showers were correct, the difference in the number of electron neutrinos measured by the two methods should be small, any difference is used to estimate the systematic error. Since this error was shown not to be correlated among energy bins, we add it in quadrature to the statistical error from the fit and take this to be the combined basic error. The error bars on the data points in Fig. B.3 show the size of this error which is dominated by the statistical error from the fit. (iii) The 1% uncertainty in the absolute energy calibration of the detector changes the relative neutrino flux which is extracted using the subset of the data sample with low hadron energy [55] by 0.4% on average. (iv) The uncertainty in the incident flux of ν_e's on the detector is estimated to be 4.1% [56]. This error is dominated by a 20% production uncertainty in the K_L content of the secondary beam which produces 16% of the ν_e flux. The majority of the ν_e flux comes from $K^\pm_{e_3}$ decays, which are well-constrained by the observed ν_μ spectrum from $K^\pm_{\mu_2}$ decays [56]. Other sources of systematic errors were also investigated and found to be small.

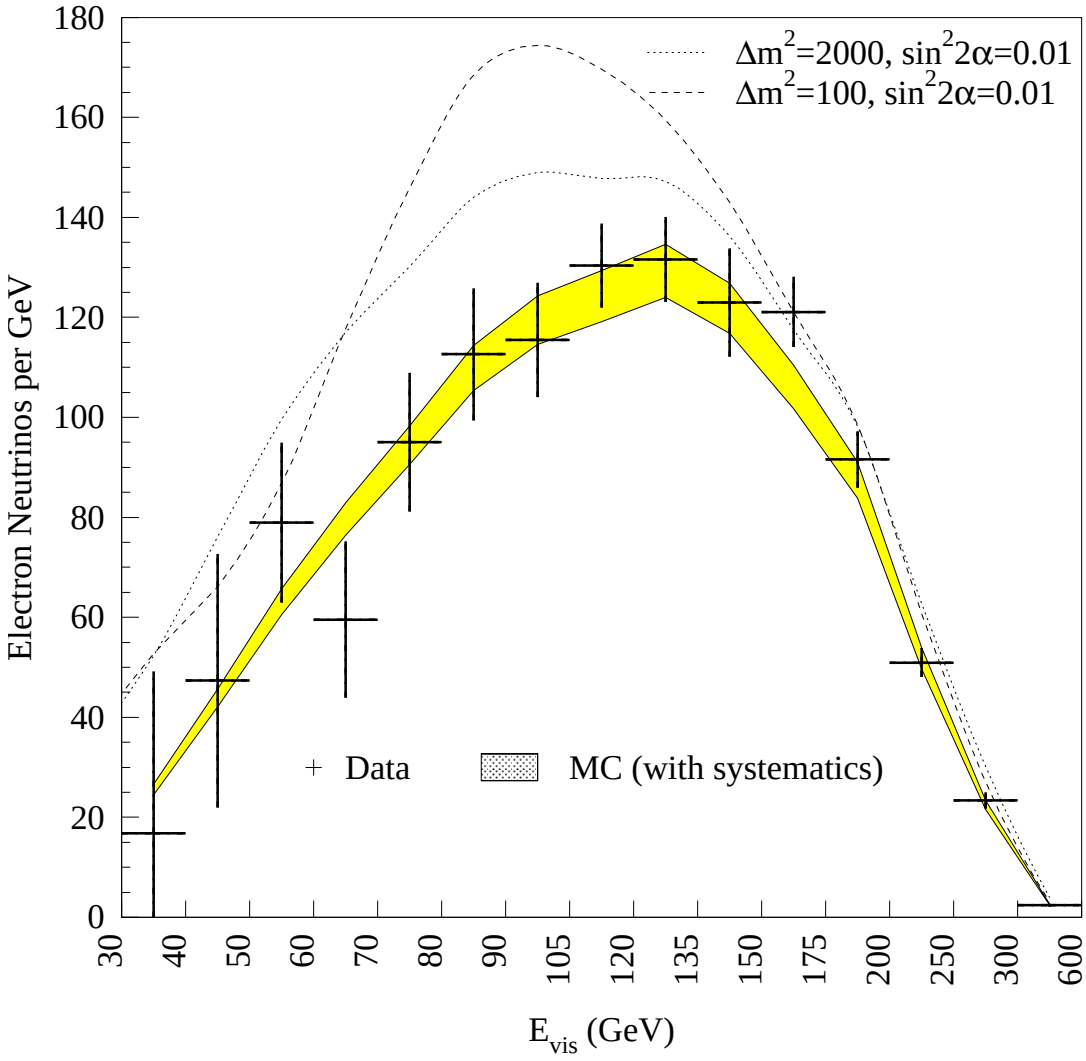

Figure B.3: Number of electron neutrinos as a function of visible energy. For electron neutrinos the visible energy is equal to the total neutrino energy. The filled band shows Monte Carlo prediction assuming no oscillations. The dotted curve corresponds to $\nu_\mu \to \nu_e$ oscillations with $\Delta m^2 = 2000$ eV^2 and $\sin^2 2\alpha = 0.01$ and the dashed curve to $\Delta m^2 = 100$ eV^2 and $\sin^2 2\alpha = 0.01$

Δm^2 (eV^2)	Best fit	σ	Δm^2 (eV^2)	Best fit	σ
1.0	-0.1741	1.6501	175.0	0.0000	0.0016
2.0	-0.0501	0.4107	200.0	-0.0002	0.0014
3.0	-0.0153	0.1852	225.0	-0.0003	0.0013
4.0	-0.0112	0.1041	250.0	-0.0004	0.0012
5.0	-0.0051	0.0671	275.0	-0.0004	0.0012
7.0	-0.0036	0.0345	300.0	-0.0004	0.0012
9.0	-0.0021	0.0213	350.0	-0.0004	0.0012
10.0	-0.0023	0.0173	400.0	-0.0003	0.0013
20.0	-0.0004	0.0048	450.0	-0.0003	0.0015
30.0	-0.0003	0.0026	500.0	-0.0004	0.0016
40.0	-0.0002	0.0018	600.0	-0.0005	0.0019
50.0	-0.0002	0.0015	700.0	-0.0003	0.0018
60.0	-0.0002	0.0014	800.0	-0.0002	0.0018
70.0	-0.0002	0.0014	1000.0	-0.0004	0.0017
80.0	-0.0003	0.0014	1500.0	-0.0003	0.0017
90.0	-0.0003	0.0015	2000.0	-0.0004	0.0017
100.0	-0.0002	0.0015	5000.0	-0.0003	0.0018
125.0	0.0004	0.0018	10000.0	-0.0004	0.0017
150.0	0.0005	0.0019	20000.0	-0.0004	0.0017

Table B.1: The result for $\sin^2 2\alpha$ from the fit at each Δm^2 for $\nu_\mu \to \nu_e$ oscillations. The 90% C.L. upper limit is equal to the best fit $\sin^2 2\alpha + 1.28\sigma$.

The data are fit by forming a χ^2 which incorporates the Monte Carlo generated effect of oscillations, the basic error, and terms with coefficients accounting for systematic uncertainties. A best fit $\sin^2 2\alpha$ is determined for each Δm^2 by minimizing the χ^2 as a function of $\sin^2 2\alpha$ and these systematic coefficients. At all Δm^2, the data are consistent with no observed $\nu_\mu \to \nu_e$ oscillations. The statistical significance of the best-fit oscillation at any Δm^2 is at most 0.3σ.

The frequentist approach [74] is used to set a 90% confidence upper limit for each Δm^2. The limit in $\sin^2 2\alpha$ corresponds to a shift of 1.64 units in χ^2 from the minimum χ^2 (at the best fit value in Table B.1). The 90% confidence upper limit is plotted in Figure B.4 for $\nu_\mu \to \nu_e$. The best limit of $\sin^2 2\alpha < 1.1 \times 10^{-3}$ is at $\Delta m^2 = 300$ eV^2. For $\sin^2 2\alpha = 1$, $\Delta m^2 > 1.6$ eV^2 is excluded, and for $\Delta m^2 \gg 1000$ eV^2, $\sin^2 2\alpha > 1.8 \times 10^{-3}$.

Under the assumption that there are no oscillations, this data can also be used to test

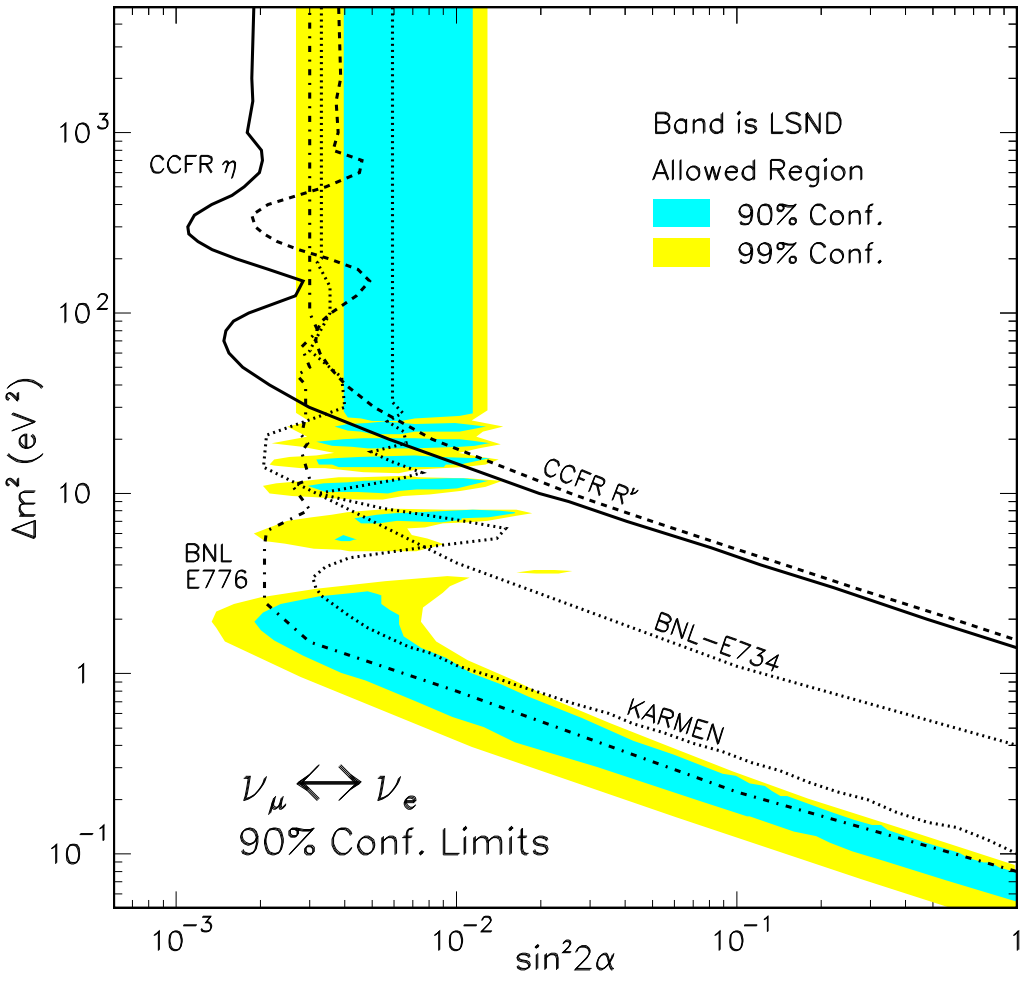

Figure B.4: Excluded region of $\sin^2 2\alpha$ and Δm^2 for $\nu_\mu \to \nu_e$ oscillations from this analysis at 90% confidence is the area to the right of the dark, solid curve.

$\nu_\mu(\overline{\nu}_\mu) \leftrightarrow \nu_e(\overline{\nu}_e)$ universality by comparing the observed ν_e flux to that predicted by the Monte Carlo. From this comparison we determine the ratio of the cross sections averaged over our flux to be $\sigma_{CC}(\nu_\mu)/\sigma_{CC}(\nu_e) = 1.026 \pm\ 0.025(\text{stat}) \pm 0.049(\text{syst})$. This is currently the most stringent test of universality at high space-like momentum transfer.

In conclusion, we have used the difference in the longitudinal shower energy deposition pattern of $\nu_e N$ versus $\nu_\mu N$ interactions to search for $\nu_\mu \rightarrow \nu_e$ oscillations with a coarse-grained calorimetric detector. We see a result consistent with no neutrino oscillations and find 90% confidence level excluded regions in the $\sin^2 2\alpha - \Delta m^2$ phase space. This result is the most stringent limit to date for $\nu_\mu \rightarrow \nu_e$ oscillation for $\Delta m^2 > 25$ eV^2. We also tested $\nu_\mu(\overline{\nu}_\mu) \leftrightarrow \nu_e(\overline{\nu}_e)$ universality and found the ratio of the ν_μ-to-ν_e cross-section to be $1.026 \pm 0.025(\text{stat}) \pm 0.049(\text{syst})$.

Bibliography

[1] B. Pontecorvo, JETP, **6**, 429 (1958); Z. Maki, M. Nakagawa and S. Sakata, Prog. Theor. Phys. **28**, 870 (1962).

[2] W. Pauli, Septieme Conseil de Physique Solvay 1933 Gauthier-Villas, Paris 324 (1934).

[3] E. Fermi, Nuovo Cimento **11** (1934).

[4] H. Bethe and R. Peirls, Nature **133**, 532 (1934).

[5] C.L. Cowan Jr., F. Reines *et al.*, Science **124**, 103 (1956).

[6] R. Davis, Bull. Am. Phys. Soc. **II 1**, 219 (1956).

[7] G. Danby *et al.*, Phys. Rev. Lett. **9**, 36 (1962).

[8] M. Perl *et al.*, Phys. Rev. Lett. **35**, 1489 (1975).

[9] N. Ushida *et al.*, Phys. Rev. Lett. **57**, 2897 (1986).

[10] Particle Data Group, Phys. Rev. **D54**, 286 (1996).

[11] A.I. Belesev *et al.*, Phys. Lett. **B350**, 263 (1995).

[12] K. Assamagan *et al.*, Phys. Rev. **D53**, 6065 (1996).

[13] D. Buskulic *et al.* Phys.Lett. **B349**, 585 (1995).

[14] L. A. Ahrens *et al.* , Phys. Rev. **D36**, 702 (1987).

[15] L. Borodovsky *et al.* , Phys. Rev. Lett. **68**, 274 (1992).

[16] B.A. Bodmann *et al.*, Nucl. Phys. **A553**, 831 (1993).

[17] C. Athanassopolous *et al.*, Phys. Rev. Lett. **77**, 3082 (1996).

[18] K.S. McFarland, D. Naples *et al.*, Phys. Rev. Lett., **75**, 3993 (1995).

[19] Y. Fukuda *et al.* Phys. Lett. **B335**, 237 (1994).

[20] R. Becker-Szendy *et al.* Phys. Rev. D **46**, 3720 (1992).

[21] K. Daum *et al.*, Z. Phys. **C66**, 417 (1995).

[22] Maury C. Goodman *et al.*, ANL-HEP-PR-94-56 (1994).

[23] Y. Fukuda *et al.* Phys. Rev. Lett. **77**, 1683 (1996).

[24] J.N. Bahcall and M.H. Pinsonneault, Rev. Mod. Phys. **64**, 885 (1992).

[25] B.T. Cleveland *et al.*, Nucl. Phys B (Proc. Suppl.) **38**, 47 (1995).

[26] GALLEX Collaboration, GX-91 (1996).

[27] V.N. Gavrin, in Proc. of Neutrino 96, ed. K. Enqvist K. Huitu and J. Maalampi (World Scientific ,Singapore), 1 (1996).

[28] G. Zacek *et al.*, Physical Review **D34**, 2621 (1986).

[29] Y. Declais *et al.*, Nucl. Phys. **B434**, 503 (1995).

[30] G.S. Vidyakin *et al.*, JETP Letters **59**, 390 (1994).

[31] R.P. Feynman, M. Gell-Mann, Phys. Rev. **109**, 193 (1958).

[32] J. Schwinger, Ann. Phys. **2**, 407.

[33] S.L. Glashow, Nucl. Phys. **22**, 579 (1961).

[34] S. Weinberg, Phys. Rev. Lett. **19**, 1264.

[35] A. Salam, "Elementary particle physics", Nobel Symp. No. 8 (ed. N. Svartholm Almqvist and Wilsell, Stockholm).

[36] F. Abe *et al.*, Phys. Rev. Lett. **75**, 11 (1995).

[37] P. Abreu *et al.*, Nucl.Phys **B421**, 3 (1994).

[38] C. Arroyo *et al.*, Phys. Rev. Lett. **72**, 3452 (1994).

[39] C.W. Kim and A. Pevsner, "Neutrinos in Physics and Astrophysics", Contemprary Concepts in Physics, Vol. 8 (Hardwood Academic, Gordon and Breach, Chur, Switzerland, 1993).

[40] F. Bohm and P. Vogel, "Physics of Massive Neutrinos" (Cambridge University Press, Cambridge, 1987).

[41] R.N. Mohapatra and P.B. Pal, "Massive Neutrinos in Physics and Astrophysics" (World Scientific, Singapore, 1991).

[42] P. Lagacker, "New Directions in Neutrino Physics", p. 95 (1988).

[43] C.W. Kim, DFTT-33-95A (1996).

[44] D0 collaboration, FERMILAB-CONF-96-114-E (1996).

[45] F. Abe *et al.*, Phys. Rev. Lett. **74**, 2900 (1995).

[46] E. Majorana, Nuo. Cim., **5**, 171 (1931).

[47] L. Wolfenstein, Nucl. Phys., **B186**, 147 (1981).

[48] M. Gell-Mann, P. Ramond and R. Slansky, in "Supergravity", ed. F. van Nieuwenhuizen and D. Freedman, (North Holland, Amsterdam, 1979) p. 315; T. Yanagida, Proc. of the Workshop on Unified Theory and the Baryon Number of the Universe, KEK, Japan (1979).

[49] S. Bludman, D. Kennedy, and P. Langacker, Phys. Rev. **D45**, 1810 (1992).

[50] A. De Rujula, M. Lusignoli, L. Maiani, S.T. Petcov, and R. Petronzio, Nucl. Phys. **B168**, 54 (1980).

[51] W.K. Sakumoto *et al.*, Nucl. Instrum. Methods **A294**, 179 (1990).

[52] B.J. King, *et al.*, Nucl. Instrum. Methods. **A 302**, 179 (1990).

[53] T. Bolton, internal memo, unpublished (1991).

[54] Wing Cheong Leung, Ph.D. Thesis, Columbia University (1991).

[55] Paul Quintas, Ph.D. Thesis, Columbia University (1992).

[56] Bruce J. King, PhD Thesis, Columbia University, Nevis preprint 284, unpublished (1994).

[57] R.P. Feynman, Phys. Rev. Lett. **23**, 1415 (1969).

[58] H.W. Atherton *et al.*, CERN 80-07 (1980).

[59] P. Skubic *et al.* Phys. Rev. **D18**, 3115 (1978).

[60] A.J. Malensek, FERMILAB-FN-0341 (1981).

[61] "Review of Particle Properties", Phys. Rev. **D45**, pp VII.84-6,95-6 (1992).

[62] K. Kodama *et al.*, Phys. Lett. **B263**, 573 (1991).

[63] R. Ammar *et al.*, Phys. Rev. Lett. **61**, 2185 (1988).

[64] M.E. Duffy *et al.*, Phys. Rev. **D38**, 2032 (1988).

[65] E.D. Commins and P.H. Bucksbaum, "Weak Interactions of Leptons and Quarks", Cambridge University Press (1983).

[66] J. Dworkin *et al.*, Phys. Rev. **D41**, 780 (1990).

[67] T.R. Cardello *et al.*, Phys. Rev. **D22**, 32 (1985).

[68] S. Dasu *et al.*, Phys. Rev. Lett. **61**, 1061 (1988).

[69] CN/ASD, GEANT, detector description and simulation tool, CERN (1995); G. Ingelman, A. Edin, J. Rathsman, DESY 96-057 (1996).

[70] F. Abe *et all*, FERMILAB-PUB-95/033-E (1995).

[71] P. Langacker, Particle Data Group, Phys. Rev. **D50**, 1309 (1994).

[72] M. L. Swartz, SLAC-PUB-6711 (1994).

[73] F. Abe *et al* FERMILAB-PUB-95/022-E (1995); S. Abachi *et al* FERMILAB-PUB-95/028-E (1995).

[74] Particle Data Group, Phys. Rev. **D54**,164 (1996).

[75] E. Ables *et al.*, Fermilab proposal No. P-875 (MINOS), 1995.

[76] P.F. Loverre, Phys. Lett. B **206**, 711 (1988).

[77] R.H. Bernstein and S.J Parke, Phys. Rev. D **44**, 2069 (1991).

[78] P.Z. Quintas *et al.*, Phys. Rev. Lett. **71**, 1307 (1993), W.C. Leung *et al.*, Phys. Lett. **B317**, 655 (1993).

[79] C.H. Albright and C. Jarlskog, Nucl. Phys. **B84**, 467 (1975).

[80] S. Jadach *et al.*, Comput. Phys. Commun. **64**, 275 (1991).

[81] A.O. Bazarko *et al.*, Z. Phys. C **65**, 189 (1995).

[82] E. Ables *et al.* Fermilab Proposal No. P-875 (MINOS), 1995.